RETROSPECTIVE COHORT STUDY TO EXAMINE DISEASE PROGRESSION IN RETINITIS PIGMENTOSA PATIENTS SEEN AT THE UNIVERSITY OF OTTAWA EYE INSTITUTE

LYNN KANDAKJI

Thesis submitted to the University of Ottawa in partial
fulfilment of the requirements for the degree of
Master of Science
in Neuroscience specialization in Human and Molecular Genetics

Department of Cellular and Molecular Medicine
Faculty of Medicine
UNIVERSITE D'OTTAWA

to experiences unexpected
paths redirected
with family by my side
friends found along the way
and God as my constant guide

Table of Contents

Table of Contents ..... *iii*
List of Tables ..... *vi*
List of Figures and Illustrations ..... *vii*
List of Abbreviations ..... *xi*
Abstract ..... *xv*
0.1 Declaration ..... *xvi*
0.2 Acknowledgements ..... *xvii*
0.3 Publications ..... *xviii*
0.4 Impact Statement ..... *xix*
Chapter 1 Introduction *1*
1.1 Retina 1
1.2 Retinal Layers 3
1.3 Retinitis Pigmentosa 4
1.4 Imaging and Testing in Retinitis Pigmentosa 6
1.4.1 Genetic Testing 7
1.4.2 Electroretinography 9
1.4.2.1 Full-field Electroretinography 10
1.4.2.2 Multi-focal Electroretinography 13
1.4.3 Visual Fields 16
1.4.3.1 Humphrey Visual Field 18
1.4.3.2 Goldmann Visual Field 23
1.4.4 Optical Coherence Tomography 25
1.4.5 Fundus Autofluorescence 29
1.5 Treatment of Retinitis Pigmentosa 31
1.5.1 Gene Therapy for Retinitis Pigmentosa 32
1.5.2 Clinical Trial Endpoints 34
1.5.3 Common pathway of cell death 36
1.5.4 X-linked Inhibitor of Apoptosis (XIAP) 37
1.6 Overview of Thesis Research 39
Chapter 2 Materials and Methods *41*
2.1 Study design 41
2.2 Study participants 42
2.3 Genetic Testing 43

2.4 Diagnostic Testing 43
2.4.1 Electrophysiology 43
2.4.1.1 Full-field testing 43
2.4.1.2 Multi-focal testing 44
2.4.2 Perimetry 45
2.4.2.1 Humphrey static visual field 45
2.4.2.2 Goldmann kinetic visual field 46
2.4.3 Optical Coherence Tomography 48
2.4.4 Fundus Autofluorescence 52
2.5 Statistical Analysis 52
Chapter 3 Results 54
3.1 Clinical Data 54
3.2 Genetics 57
3.3 Current Status, Distribution, and Symmetry of Study Cohort 59
3.4 Rates of disease progression for each of the parameters 70
3.4.1 Ellipsoid zone shortening with time 70
3.4.2 Humphrey mean deviation change with time 73
3.4.3 Goldmann rate of isopter constriction 75
3.4.4 ERG amplitude attenuation and latency increase 78
3.5 Correlations between different diagnostic variables 81
3.5.1 Correlation between diagnostic tests evaluating the central 30° of retina 82
3.5.1.1 Relationship of ellipsoid zone to mean deviation 82
3.5.1.2 Relationship of ellipsoid zone to central isopter constriction 83
3.5.1.3 Relationship of ellipsoid zone to mfERG amplitude 84
3.5.1.4 Relationship of mean deviation to mfERG amplitude 85
3.5.1.5 Relationship of central isopter constriction to mfERG amplitude 86
3.5.2 Correlation between diagnostic tests evaluating the total retina 87
3.5.2.1 Relationship of rod amplitude to ellipsoid zone 87
3.5.2.2 Relationship of cone amplitude to ellipsoid zone 89
3.5.2.3 Relationship of total photoreceptor function to isopter constriction ... 90
Chapter 4 Discussion 91
4.1 Discussion of results 91
4.2 Limitations 100
4.3 Meaningful efficacy measures for a clinical trial 101

4.4 Conclusions 103
Bibliography *104*
Appendix *126*
A. ImageJ protocol for manual measurement of ellipsoid zone on OCT *126*
B. Normative data for multi-focal ERG *126*
C. Normative data for full-field ERG *127*
D. Supplemental results *129*
Curriculum Vitae *135*

List of Tables

Table 1. Options for Goldmann kinetic stimuli. 24

Table 2. Normal isopter position in the peripheral visual field in kinetic perimetry. 24

Table 3. Selected interventional therapy clinical trials for retinitis pigmentosa. 33

Table 4. Demographics, metrics, and diagnostic summary of study cohort 55

Table 5. Intersections of diagnostic testing by number of patients 57

Table 6. Genotype, proteins, and their functions in study subjects with genetic results available 58

Table 7. Rate of progression in RP via SD-OCT 72

Table 8. Rate of ellipsoid zone progression in RP as a factor of genetic inheritance. 73

Table 9. Rate of progression in RP via HVF. SE = Standard Error. 74

Table 10. Rate of progression in RP via GVF. SE = Standard Error. 77

Table 11. Difference in progression rates (deg/year) between isopter sizes. 77

Supplemental Table I. Correlation of ellipsoid zone length and mfERG amplitude and latencies. 130

Supplemental Table II. Correlation of ellipsoid zone length and ffERG amplitudes and latencies. 130

Supplemental Table III. Correlation of HVF mean deviation and mfERG amplitudes and latencies. 130

Supplemental Table IV. Correlation of GVF isopter length and mfERG amplitudes and latencies. 131

Supplemental Table V. Correlation of GVF isopter length and ffERG amplitudes and latencies. 132

List of Figures and Illustrations

Figure 1.1 The eye and the retinal mosaic. 2

Figure 1.2. Fundus photography showing the posterior pole of a healthy eye (left) and a patient with retinitis pigmentosa (right). 7

Figure 1.3. Venn diagram of currently identified genes associated with retinitis pigmentosa and their genetic overlap with other inherited retinal dystrophies. 9

Figure 1.4. ERG response recorded from a healthy individual after both dark-adaptation (scotopic) and light-adaptation. 11

Figure 1.5. Example of full-field ERG recordings in a healthy patient and in patients with different disease stages of retinitis pigmentosa. 13

Figure 1.6. Example of a multi-focal recording obtained in a normal eye displayed in three different ways. 15

Figure 1.7. Traces of multifocal ERG arrays showing progression of responses with respect to different stages of retinitis pigmentosa. 15

Figure 1.8. The spatial extent of a normal visual field. 16

Figure 1.9. Sensitivity thresholds. 19

Figure 1.10. Correspondence between retinal nerve fibres and visual field. 19

Figure 1.11. Single field analysis (SFA) printouts of STATPAC software analysis in Humphrey Field Analyzer (HFA). 21

Figure 1.12. Humphrey Field Analyzer greyscale pattern and mean deviation in 4 patients with different stages of RP. 22

Figure 1.13. Normal Goldmann kinetic perimetry isopters for a healthy 20–30-year-old person. 25

Figure 1.14. Illustrative example of a typical monocular visual field progression in a patient with retinitis pigmentosa using Goldmann kinetic perimetry. 25

Figure 1.15. Fovea-centred SD-OCT scan of a healthy eye, showing various optical layers of the retina. 27
Figure 1.16. Progressive changes in a patient with retinitis pigmentosa via fundus autofluorescence imaging. 31
Figure 2.1. Champlain Local Health Integration Network. 41
Figure 2.2. Goldman visual field isopter measurement. 48
Figure 2.3. Ellipsoid zone measurement using ImageJ. 50
Figure 2.4. Various OCT presentations within study cohort. 51
Figure 3.1. Genetic inheritance distribution of study cohort. 56
Figure 3.2. Distribution of ellipsoid zone lengths. 60
Figure 3.3. Correlation of ellipsoid zone length between eye pairs 60
Figure 3.4. Distribution of mean deviations across various testing protocols. (A) 61
Figure 3.5. Correlation of mean deviation between eye pairs. 61
Figure 3.6. Distribution of isopter lengths across five stimulus sizes. 62
Figure 3.7. Correlation of isopter lengths between eye pairs. 62
Figure 3.8. Distribution of multifocal ERG responses across five rings. 63
Figure 3.9. Correlation of mfERG responses between eye pairs. 64
Figure 3.10. Distribution of photopic ffERG responses. 65
Figure 3.11. Correlation of photopic ERG responses between eye pairs. 65
Figure 3.12. Distribution of photopic 30Hz flicker responses. 66
Figure 3.13. Correlation of 30Hz Flicker ERG responses between eye pairs. 66
Figure 3.14. Distribution of full-field ERG scotopic responses 68
Figure 3.15. Correlation of scotopic ERG responses between eye pairs. 69
Figure 3.16. Bland-Altman plot showing the difference in ellipsoid zone length measurements between readers. 70

Figure 3.17. Structural progression of ellipsoid zone for patients with retinitis pigmentosa over a 10-year follow-up period. 71
Figure 3.18. Relationship between the initial ellipsoid zone width and progression rate over one month. 73
Figure 3.19. Functional visual field progression via automated perimetry for patients with retinitis pigmentosa over a 10-year follow-up period. 74
Figure 3.20. Bland-Altman plot showing the difference in isopter length measurements between readers. 75
Figure 3.21. Technician contribution to test-retest variability. 76
Figure 3.22. Goldmann isopter constriction for patients with retinitis pigmentosa over a 10-year follow-up period. 77
Figure 3.23. mfERG P1 Amplitude attenuation for patients with retinitis pigmentosa over a 10-year follow-up period. 78
Figure 3.24. ffERG 30Hz flicker peak amplitude attenuation for patients with retinitis pigmentosa over a 10-year follow-up period. 79
Figure 3.25. ffERG photopic a- and b-wave amplitude change for patients with retinitis pigmentosa over a 10-year follow-up period. 79
Figure 3.26. ffERG scotopic a- and b-wave amplitude change across 3 luminance intensities for patients with retinitis pigmentosa over a 10-year follow-up period. .. 80
Figure 3.27. Correlation of ellipsoid zone length and Humphrey visual field mean deviation for patients with retinitis pigmentosa. 82
Figure 3.28. Correlation of ellipsoid zone length and Goldmann isopter length for patients with retinitis pigmentosa. 83
Figure 3.29. Correlation of ellipsoid zone length and multi-focal ERG P1 amplitude for patients with retinitis pigmentosa. 84

Figure 3.30. Correlation of mean deviation and multi-focal ERG P1 amplitude per unit area for patients with retinitis pigmentosa. 85
Figure 3.31. Correlation of Goldmann isopters I3e and I2e and multi-focal P1 amplitude responses in patients with retinitis pigmentosa. 86
Figure 3.32. Correlation of ellipsoid zone and rod photoreceptor function for patients with retinitis pigmentosa. 88
Figure 3.33. Correlation of ellipsoid zone length and cone photoreceptor function tested through various ffERG responses for patients with retinitis pigmentosa. 89
Figure 3.34. Correlation of Goldmann isopters and full-field ERG responses patients with retinitis pigmentosa. 90
Supplemental Figure I. Various FAF presentations within study cohort. 129

List of Abbreviations

A-scan	Amplitude scan
AAV	Adeno-associated virus
AD	Autosomal dominant
ANOVA	Analysis of Variance
AR	Autosomal recessive
B-scan	Brightness scan
BCVA	Best corrected visual acuity
cd	Candela
CHEO	Children's Hospital of Eastern Ontario
CME	Central macular oedema
COR	Coefficient of repeatability
COS	Canadian Ophthalmological Society
CT	Computed tomography
dB	Decibels
DNA	Deoxyribonucleic acid
DTL	Dawson, Trick, and Litzkow
ELM	External limiting membrane
EMA	European Medicines Agency
EMR	Electronic medical record
ERG	Electroretinography
ETDRS	Early Treatment Diabetic Retinopathy Study
EZ	Ellipsoid Zone
FAF	Fundus autofluorescence

FDA	Food and Drug Administration
ffERG	Full-field electroretinography
FL	Fixation losses
FN	False negative
FP	False positive
FST	Full-field stimulus testing
GCL	Ganglion cell layer
GVF	Goldmann visual field
HAR	Hyperautofluorescent ring
HEYEX	Heidelberg Eye Explorer
HFA	Humphrey Field Analyzer
HNL	Henle fibre layer
HRA	Heidelberg retina angiograph
HVF	Humphrey visual field
ICC	Intraclass coefficient
iJCAHPO	International Joint Commission on Allied Health Personnel in Ophthalmology
ILM	Internal limiting membrane
INL	Inner nuclear layer
IPL	Inner plexiform layer
IRD	Inherited retinal diseases
IS	Inner segment
ISCEV	International Society for Clinical Electrophysiology of Vision
IU	International units
LHON	Leber's hereditary optic neuropathy

LMM	Linear mixed model
MD	Mean Deviation
mfERG	Multi-focal electroretinography
MLMT	Multi-luminance mobility tests
MRI	Magnetic resonance imaging
MRN	Medical record number
ms	Millisecond
MT	Mitochondrial
NFL	Nerve fibre layer
NI	Nasal inferior
NS	Nasal superior
nv/deg^2	Nanovolts/degrees area
OCT	Optical coherence tomography
OCT-A	Optical coherence tomography angiography
OD	Optic disc
OD	Oculus dexter (right eye)
OEI	Ottawa's Eye Institute
OHRI	Ottawa Hospital Research Institute
ONL	Outer nuclear layer
OP	Oscillatory potential
OPL	Outer plexiform layer
OS	Outer segment
OS	Oculus sinister (left eye)
P-value	Probability value
PL	Photoreceptor layer

PLR	Pupillary light reflex
PRC	Photoreceptor cell
PSD	Pattern standard deviation
RIP	Receptor interacting protein
RP	Retinitis Pigmentosa
RPE	Retinal pigment epithelium
SD	Standard deviation
SD-OCT	Spectral-domain optical coherence tomography
SE	Standard error
SITA	Swedish interactive thresholding algorithm
SS-OCT	Swept-source optical coherence tomography
t-test	Test statistic test
TI	Temporal inferior
TNF	Tumour necrosis factor
TOH	The Ottawa Hospital
TS	Temporal superior
VF	Visual field
VFI	Visual field index
VO	Vessel occlusion
XL	X-linked
XIAP	X-linked inhibitor of apoptosis
µm	Micrometres
µV	Microvolts

Abstract

Retinitis pigmentosa (RP) is the most common form of inherited retinal degeneration, heterogenous in its clinical presentation and genetic cause. Understanding the short-term disease mechanisms is pivotal for the development of new therapies. Upcoming clinical trials will take genotype-agnostic approaches; therefore, a comprehensive analysis of progression that encompasses many genetic factors will be needed. In this 10-year retrospective cohort study, rates of progression were measured, structurally and functionally, in 85 RP patients seen at the Ottawa Eye Institute. Parameters examined were the ellipsoid zone (EZ) length on an optical coherence tomography (OCT) image, Humphrey and Goldmann visual fields (VF), and full-field and multifocal electroretinograms (ERGs). RP is revealed to have a 1st order exponential decay pattern of loss, with mean rates of decline of 7.65 %/year for ellipsoid zone (EZ) length, 6.35%/year, 4.39%/year, and 1.57%/year for the Humphrey VF 30-2, 24-2, and 10-2 mean deviation (MD) respectively, and 5.22%/year, 7.77%/year, 6.77%/year, 6.80%/year, and 12.45%/year for Goldmann V4e, III4e, I4e, I3e, and I2e isopter lengths, respectively. In cases where different diagnostic tests were conducted within 3 months of each other, the data was analysed to determine if there was a positive correlation between the diagnostic tests. Ellipsoid zone length and Humphrey 24-2 mean deviation exhibited the strongest association with a coefficient of 0.99. The study reveals structural and functional changes in advanced retinitis pigmentosa and presents a protocol for assessing short-term progression.

0.1 Declaration

I hereby certify that this thesis is entirely my own original work except where otherwise indicated. Any use of the works of any other author, in any form, is properly acknowledged at their point of use.

0.2 Acknowledgements

I am very grateful for having been offered the opportunity to undertake this Masters and deepen my knowledge of ophthalmology, statistics, genetics, and conducting research. These two years have truly shaped my critical thinking skills and has encouraged to me to continue pursuing academia at the next level. First and foremost, my eternal gratitude to my family for their devotion and support. Their constant encouragement and faith in me have been my pillars of strength throughout this journey. Without their sacrifices, both big and small, this pursuit of higher education would not have been possible. Secondly, I wish to thank all the remarkable people I am honoured to have gotten to know and work with. My supervisor, Cathy Tsilfidis, for her approachability, support, understanding, and encouragement through the obstacles, and for her pragmatism and guidance. My two thesis advisors: Michael Dollin, for his invaluable clinical insight which I absorbed rapaciously since my undergraduate OMT days, and Stuart Coupland, whose expertise in research and electrophysiology carried me through both my honours project and this thesis. Tim Ramsay, for his guidance in statistics and in tackling this complex dataset. Marah Elkabouli: for her tireless contribution as second reader. Natalie Doran, for her support in ERG data collection. Nada Mariamme Ukena, for being my biggest cheerleader and the brightest presence in the hospital. The clinical staff at the University of Ottawa Eye Institute, for their assistance in data collection, including Ange-Lynca Kantungane, Hong-An Nguyen, Chloe Gottlieb, Bernard Hurley, and Brian Leonard. Finally, the DORF committee at the University of Ottawa Eye Institute, for their financial support, including Rustum Karanjia and Pamela Lagali. I also wish to acknowledge the Ontario Research Fund, Canadian Institute of Health Research, The Ottawa Hospital Department of Ophthalmology Research Fund, and Excelerator Program for funding this research.

0.3 Publications

This study has been submitted as an abstract for the Canadian Ophthalmological Society (COS) 2023. At the time of writing, a manuscript for publication is underway but yet to be submitted.

0.4 Impact Statement

Vision is undoubtedly the most important sense for humans, such that 30 to 55% of the brain is devoted to sight (Sheth & Young, 2016). Visual impairments have dire consequences for quality of life and productive activities. The retina contains a surprising complexity in its cellular architecture, and quite literally presents a window to the brain; no other part of the central nervous system is amenable to direct observation. Given the increasing economic and social burdens of blindness due to the aging of our population, there is an urgent necessity for Canada to establish a comprehensive national vision plan, one that encompasses research, prevention, and treatment strategies to address the growing challenges posed by vision loss.

In this context, retinitis pigmentosa (RP) is a condition that demands our attention. Although classified as a "rare disease," it is one of the most common inherited diseases of the retina, affecting between 1 in 3500 to 1 in 4000 Canadians (Pagon, 1988; Verbakel et al., 2018). It affects individuals at an age when the gradual loss of vision exerts a maximal effect on their quality of life and employment opportunities. At present, there are no effective treatments available to halt or reverse the progression of RP, making it a condition of compelling clinical need.

The research within this thesis has been conducted in close collaboration with several clinicians whose area of expertise is treating patients with retinitis pigmentosa and with scientists who have devoted their career to developing potential treatments. The scope of data amassed and meticulously analysed in this study surpasses previous efforts, providing a multimodal insight into the trajectory of RP over a ten-year period. Through meticulous observation, data collection, and advanced statistical analysis, this thesis unravels the intricate nuances of how RP progresses over time, both short- and long-term.

This comprehensive examination of the disease's evolution includes detailed assessments of demographic data, retinal structure, genetic markers, and a diverse array of diagnostic data. Moreover, the core contribution of this thesis lies in its effort to correlate several variables of RP progression, many of which have never been previously explored. By identifying and quantifying the relationships between genetic predisposition, clinical manifestations, and structural and functional changes in the retina, we have achieved a level of clarity that was previously elusive in the field, particularly for a Canadian population. This work aims to lay a sturdy foundation for the development of a Canadian clinical trial, poised to usher in a new era in the treatment of retinitis pigmentosa.

Chapter 1 Introduction

1.1 Retina

The retina develops as an outgrowth of the forebrain and is a neural network lining the back of the eye responsible for the primary function of the eyeball as a photosensitive surface. Retinal landmarks include the optic disc (nerve head), macula, fovea, and foveola. The macula is the posterior central focal point for the eye's optic system, marked by intense pigmentation and responsible for providing sharp central vision and colour discrimination. At its centre is the fovea, a retinal depression formed by sideways displacement of some internal retinal layers, exposing photoreceptor cells (Figure 1.1A). The central pit within the fovea is the foveola. The fovea and the optic disc have a diameter of 1.5 mm while the macula is 3 mm (Squire, 2011). The ora serrata is the serrated anterior limit of the retina. From ora to ora the length of the retina is approximately 32 mm along the horizontal meridian (Van Buren., 2005). This is calculated from the expectations that the average dimension of the human eye is 22 mm from anterior to posterior poles, and that 72% of the inside of the globe is retina (Michels et al., 1991).

Rods and cones are the two types of light-sensitive photoreceptor cells. The retina adapts very well to varying light intensities by a dual system: photopic and scotopic. The photopic system functions in bright daylight and employs cone photoreceptors, whereas the scotopic system functions under dim light and darkness and employs rod photoreceptors. The rods are more numerous, some 120 million, and are more sensitive than the cones (Orna, 1985). However, they are not sensitive to colour. The six to seven million cones provide the eye's colour sensitivity, and they are much more concentrated in the central retinal area known as the macula (Orna, 1985). In the centre of the macula is the fovea, a tiny rod-free area densely packed with cones that are individually coupled

to a neuron (Kolb et al., 2020), providing the sharpest vision. Measured density curves for the rods and cones on the retina (Figure 1.1D) show an enormous density of cones in the fovea centralis. At a few degrees away from the fovea rod density rises to a high value and spreads over a large area of the retina. These rods are responsible for night vision, sensitive motion detection, and peripheral vision (Orna, 1985).

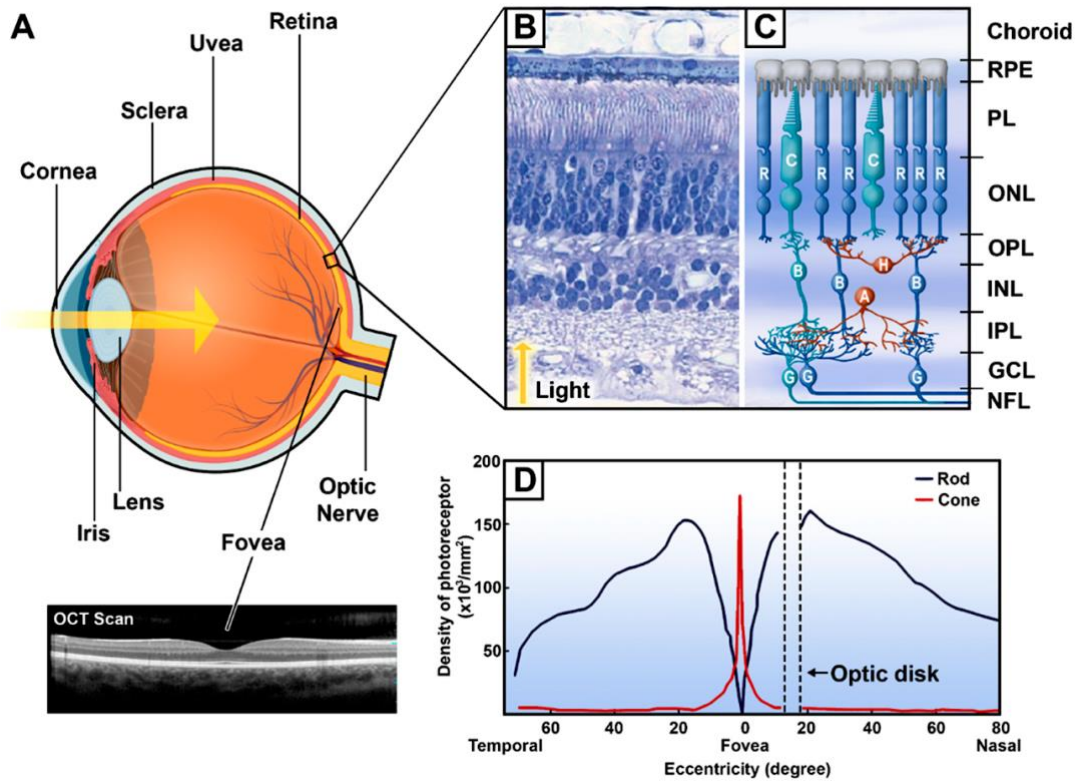

Figure 1.1 The eye and the retinal mosaic. (A) A sagittal section of the eye and an optical coherence tomography (OCT) scan of the central retina. The yellow arrow represents the path of the light rays entering the eye. (B) An H&E-stained transverse section of a human retina. Adapted from (Swaroop & Zack, 2002). (C) Schematic organization of retinal cells from the retinal pigment epithelium to the nerve fibre layer. (D) Density of cones and rods throughout the retinal surface. Adapted from (Osterberg, 1935). OCT, optical coherence tomography; R, rod; C, cone; H, horizontal cell; B, bipolar cell; A, amacrine cell; G, retinal ganglion cell; RPE, retinal pigment epithelium; PL, photoreceptor layer; ONL, outer nuclear layer; OPL, outer plexiform layer; INL, inner nuclear layer; IPL, inner plexiform layer; GCL, ganglion cell layer; NFL, nerve fibre layer. Reproduced with permission under Creative Commons CC-BY license (Ptito et al., 2021)

1.2 Retinal Layers

Over most of its area, the human retina is comprised of numerous layers (Figure 1.1B, C). The retinal pigment epithelium (RPE) is found beneath the outer retina. It provides numerous roles, including roles in nutrient and waste product exchange, photoreceptor outer segment turnover and phototransduction. Next is the photoreceptor layer (PL), which is composed of an outer segment (OS) and inner segment (IS). The OS and IS are connected via a narrow connecting cilium (Oyster & Haver, 1999). The IS is more commonly known as the ellipsoid zone (EZ) and will henceforth be referred to as such. The EZ is the photoreceptors' metabolic centre, and is filled with mitochondria, whereas the OS contains photopigments. The retina itself contains three layers of neuron cell bodies; the outer nuclear layer (ONL) containing the rod and cone photoreceptors, the inner nuclear layer (INL) containing bipolar, amacrine and horizontal cells, and the retinal ganglion cell layer (GCL), containing ganglion cells and displaced amacrines. There is also one glial cell type in the retina, the Muller glial cell, whose cell body is found in the INL, but which spans almost the entire thickness of the retina, and which provides nutritional and structural support for the neurons. Two plexiform layers contain synapses from one neuron type to another; the outer plexiform layer (OPL) contains synapses from photoreceptors to neurons in the INL, and the inner plexiform layer (IPL) contains synapses between INL neurons and ganglion cells. The nerve fibre layer (NFL) is found at the inner surface of the retina, and it contains the axons of the retinal ganglion cells (Figure 1.1B, C). External (ELM) and internal (ILM) limiting membranes are found at the outer and inner surfaces of the retina, respectively. The ELM is at the junction of the ONL and inner segments of the photoreceptors, and the ILM separates the vitreous from the retina.

The retinal thickness shows greatest variations in the centre. The retina is thinnest at the foveal floor, between 0.10 and 0.200 mm, and thickest at the foveal rim, between 0.23 and 0.320 mm (Kolb et al., 2020). Beyond the fovea the retina rapidly thins until the equator. At the ora serrata the retina is thinnest of all at 0.080 mm (Kolb et al., 2020).

1.3 Retinitis Pigmentosa

Most human retinal diseases mainly affect one of two sites in the human retina: the photoreceptor layer and the RPE, or the nerve fibre layer. Pigmentary retinal degeneration, as seen through the ophthalmoscope, was first described by van Trigt in 1853 (Van Trigt, 1852) and named retinitis pigmentosa by Donders in the Netherlands (Donders, 1857). The term retinitis pigmentosa (RP) encompasses a group of hereditary retinal degenerations characterized by diffuse progressive dysfunction of photoreceptor cells (PRCs) or the retinal pigment epithelial cells, causing progressive vision loss. It is the leading genetic cause of visual handicap among populations in developed countries, estimated to affect between 1 in 3000 to 1 in 4000 people worldwide (Perea-Romero et al., 2021; Verbakel et al., 2018).

RP is notoriously highly heterogenous in genetic cause and clinical presentation and shows considerable overlap with other inherited retinal diseases. Onset is typically in one's teens but usually refers to the age at which a patient reports visual symptoms. In a study by Tsujikawa and colleagues, they found the average age at diagnosis was 35 years old and the median age 36 years old (Tsujikawa et al., 2008). Depending on the nature of the condition and its duration, a patient could become blind as early as age 30 and legally blind by age 60, or their case may be mild and remain stable for a lifetime. Those who develop the disease early on in life as teens tend to have a worse prognosis than those whose onset occurs in their 40s and 50s (O'Neal & Luther, 2023). As patients tend to see

a doctor only when they experience serious vision problems, the task to determine the mechanism of development of RP is a difficult one. At this time, there is still much that remains to be understood in the aetiology of RP.

The classic symptoms of RP are impaired adaptation, night blindness, and difficulty with mid-peripheral visual field, progressing to a loss of far-peripheral field and eventually to a loss of central vision (Hamel, 2006). In the first stage, when the rods are dying, patients have trouble adapting to situations where there is a reduction in lighting such as driving into a tunnel or walking into a dark room. This symptom reflects the widespread rod degeneration. Today, artificial lighting is commonly used for night-time activities, leading to patients being unaware of the issue for a long time. As RP progresses, the patient undergoes gradual constriction of their visual field progressing to a central island. One study showed that patients do not have trouble with daily tasks so long as their visual field is greater than 50 degrees in diameter (Szlyk et al., 2001). However, other pathological events such as posterior subcapsular cataracts (G. A. Fishman et al., 1985), cystoid macular oedema, macular holes, diffuse retinal vascular leakage, macular preretinal fibrosis and epiretinal membrane formation (Hagiwara et al., 2011) may occur early in the disease and further degrade the central vision.

The typical progression of RP, where rod death precedes the death of cones, is also known as a rod-cone dystrophy, and is the most common clinical manifestation of the disease (Jaffal et al., 2022). Although most mutations that cause RP are almost exclusively expressed in rods, cones also die as a result of such mutations. As rods outnumber cones at a ratio of >20:1 and photoreceptors account for approximately 75% of all retinal cells, loss of rods severely alters the retinal architecture. Cones suffer from a nutrient shortage induced by this disruption of the retinal architecture after approximately 90% rods have been lost irrespective of rod death kinetics (Punzo et al., 2009). Cone

death initiates as a cell autonomous event due to a reduction in nutrient flow from the adjacent cell layer, the retinal-pigmented epithelium. During end stage RP, cones display signs of prolonged starvation, and this results in loss of central vision (Verbakel et al., 2018). Catching RP in early stages and assessing progression can be a challenge, as patients with RP can retain good visual acuity until late in the disease course. Visual acuity tends to be an insensitive measure of disease severity, so more specialised tests of visual function are required to diagnose and monitor RP.

1.4 Imaging and Testing in Retinitis Pigmentosa

The diagnosis of retinitis pigmentosa can often be made with direct visualization of the fundus using an ophthalmoscope and ophthalmic diagnostic testing. A fundus exam would reveal the classic triad of "bone spicule" retinal appearance, blood vessel attenuation, and optic disc pallor (Figure 1.2) (Hamel, 2006). Bone spicule pigmentation is due to detachment of RPE cells which have migrated to the inner retina after PRC death and usually develops in the mid-stages of the disease, starting at the mid-periphery, and moving towards the macula as the disease progresses (Milam et al., 1998). Blood vessel constriction is understood to be due to reduced metabolic demand and reduced blood flow as a result of a hyperoxic state after the loss of oxygen-consuming PRCs (Grunwald et al., 1996; Yu & Cringle, 2005). Blood vessel ischemia in turn diminishes the traditional colour of the optic nerve, causing the waxy pallor often seen in later stages of the disease (Ilhan & Citirik, 2019). Aside from the observed clinical signs, genetic testing as well as numerous structural and functional measures have been used to assess disease progression in RP, including electroretinography (ERG), visual field (VF) testing, optical coherence tomography (OCT) and fundus autofluorescence (FAF).

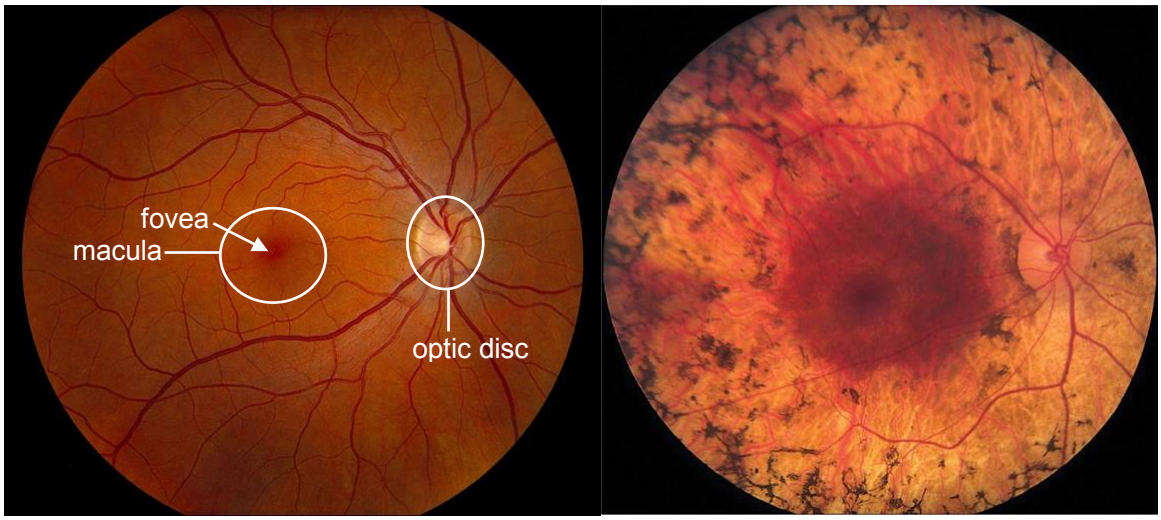

Figure 1.2. Fundus photography showing the posterior pole of a healthy eye (left) and a patient with retinitis pigmentosa (right). Note the "waxy disk", the attenuated retinal vessels and the bony spicule-like pigmentary deposits throughout the midperiphery. Reproduced with permission under Creative Commons CC-BY (Vislisel, n.d.)

1.4.1 Genetic Testing

Genetic testing is a cornerstone in the diagnosis and management of retinitis pigmentosa. In most cases, comprehensive next-generation sequencing can be performed at minimal to no cost to the patient, with multiple sponsored, open-access gene panels commercially available. However, causative genetic variants are identified in about 60 percent of cases (H. Huang et al., 2018), leaving a significant portion of cases with an undetermined genetic aetiology. Furthermore, the ubiquitous presence of variants of uncertain significance can complicate the interpretation of results. At the time of writing, there are over 75 genes (Stephen P. Daiger, 2022) associated with non-syndromic RP (affecting only the retina), and an additional 35 genes for syndromic RP (affecting other tissues and organs) (Branham et al., 2020; S. P. Daiger et al., 2013; Verbakel et al., 2018). Figure 1.3 provides an overview of the different causative genes in RP and their overlap with other inherited retinal diseases (IRDs). Of those genes with known functions, some encode proteins involved in the visual transduction cascade (e.g., rhodopsin), others in maintenance of photoreceptor structure (e.g., peripherin), and others are involved in

regeneration of the rhodopsin chromophore (11-cis retinal) in the visual cycle (e.g., retinal pigment epithelium protein (RPE) 65). Of those affected with RP, approximately 20% are autosomal recessive (AR), 20% are autosomal dominant (AD), 10% are X- linked (X), and the remainder are isolated (simplex RP; no known family history) (Bunker et al., 1984). The most common form of syndromic RP is autosomal recessive Usher syndrome, which accounts for about 10-15% of RP and is associated with either profound (Type I), partial (Type II), or progressive (Type III) hearing loss (Bunker et al., 1984). The second most common form of syndromic RP is Bardet Biedl syndrome, an autosomal recessive disorder. Due to the large number of causative genes and known phenotypic variance associated with RP, the disease's clinical findings, onset and progression may differ considerably between affected individuals. X-linked is the rarest and severest form of RP with an earlier and worse prognosis of near total loss of vision (Parmeggiani et al., 2011; Michael A. Sandberg et al., 2007). Autosomal recessive RP is the most common form and also tends to present early in life but with intermediate outcomes (O'Neal & Luther, 2023). Autosomal dominant forms are the least severe mode of causation; patients experience a more gradual onset of RP typically in adult life, with variable penetrance and less severe visual loss (Grøndahl, 2008).

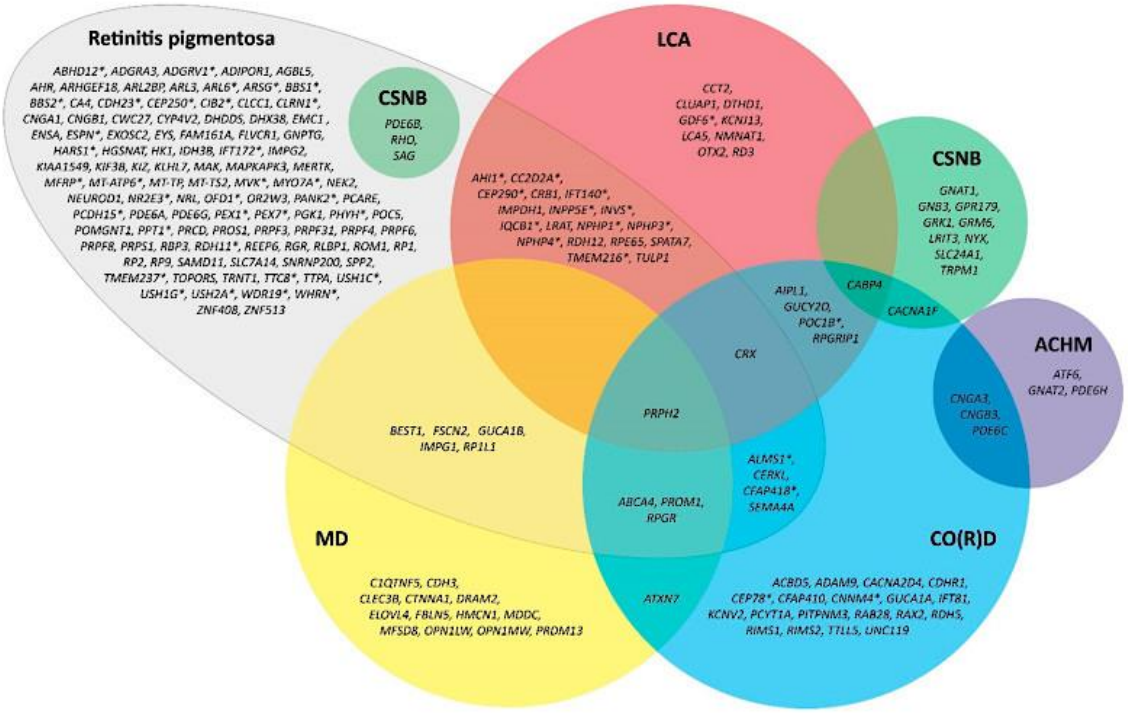

Figure 1.3. Venn diagram of currently identified genes associated with retinitis pigmentosa and their genetic overlap with other inherited retinal dystrophies. All genes included are registered in the Online Mendelian Inheritance in Man (OMIM) database and follow the up-to-date symbols of the HUGO Gene Nomenclature Committee (HGNC). Genes that are associated with syndromic forms of RP are marked with an asterisk (*). ACHM = achromatopsia; CO(R)D = cone(-rod) dystrophy; CSNB = congenital stationary night blindness; LCA = Leber Congenital Amaurosis; MD = macular dystrophy. Reproduced with permission under Creative Commons CC-BY (Nguyen et al., 2023).

1.4.2 Electroretinography

Electroretinography testing serves as an objective measure of retinal function and is an evoked potential, meaning that a stimulus (usually a flash of light) is required to generate it. This electrical potential is usually picked up with an active electrode placed on the eye (i.e., the cornea or conjunctiva) or on the skin around the eye. The response is produced by light-induced movements of ions (potassium and sodium) in the retina (Lam, 2005). The ERG signal is usually obtained in photopic (or light-adapted) and scotopic (or dark-adapted) conditions to assess cone- and rod-mediated function, respectively. There are two ERG modalities relevant to our study here: full-field (ffERG) and multi-focal (mfERG). Conventional full-field ERG records the summed electrical response from the

entire retina elicited by full-field "ganzfeld" flash stimulation (Lam, 2005). It can assess general rod and cone function separately but cannot adequately detect local retina dysfunction. For instance, an isolated macular lesion is unlikely to decrease the overall ERG response enough to be detectable by the full-field ERG (Lam, 2005). Multifocal ERG is a technique that has been developed to measure topographical retinal function of the central 30°. It is not a replacement for the full-field ERG but is considered as a different test to provide localised retinal information. However, although ERG can quantify retinal function objectively, it is highly susceptible to technical variations and requires centre-based validation (McCulloch et al., 2015).

1.4.2.1 Full-field Electroretinography

The full-field ERG measures the overall rod- and cone-generated retinal responses to flashes of light of varying intensities and frequencies. The International Society for Clinical Electrophysiology of Vision (ISCEV)-suggested protocol for full-field ERG includes five standard responses (M. F. Marmor, 1999; M. F. Marmor & Zrenner, 1998; McCulloch et al., 2015), which are broken down into three scotopic and two photopic responses. The responses thus obtained are evaluated based on appearance or morphology and quantified by measuring the amplitude and implicit time of their two major components, namely the a-wave (the short latency negative wave) which signals the activation of the photoreceptors and the b-wave (the larger positive wave that follows) which arises from the combined activities of the bipolar and Müller cells. The amplitude of the a-wave is measured from the baseline to the base of the a-wave negative trough, and the amplitude of the b-wave is measured from the a-wave trough to the top of the b-wave positive peak. The implicit time of each wave is the time from stimulus onset to its peak (Figure 1.4). Low voltage high-frequency oscillations are also seen on the ascending

limb of the b-wave. They are referred to as the oscillatory potentials (OPs) and are likely generated by amacrine and bipolar cells in response to both rod- and cone-generated activity. OPs usually consist of three larger wavelets followed by smaller ones during the ascending phase of the b-wave, and are designated in order as OP1, OP2, OP3 and so on (Janáky et al., 1996; X.-X. Li & Yuan, 1990; Rousseau & Lachapelle, 1999; Speros & Price, 1981; Wachtmeister, 1980, 1981, 1998). The amplitudes and implicit times of each of the wave forms are compared to a group of age-matched normative ERG values, which must be collected by each facility because of differences in recording equipment and technique.

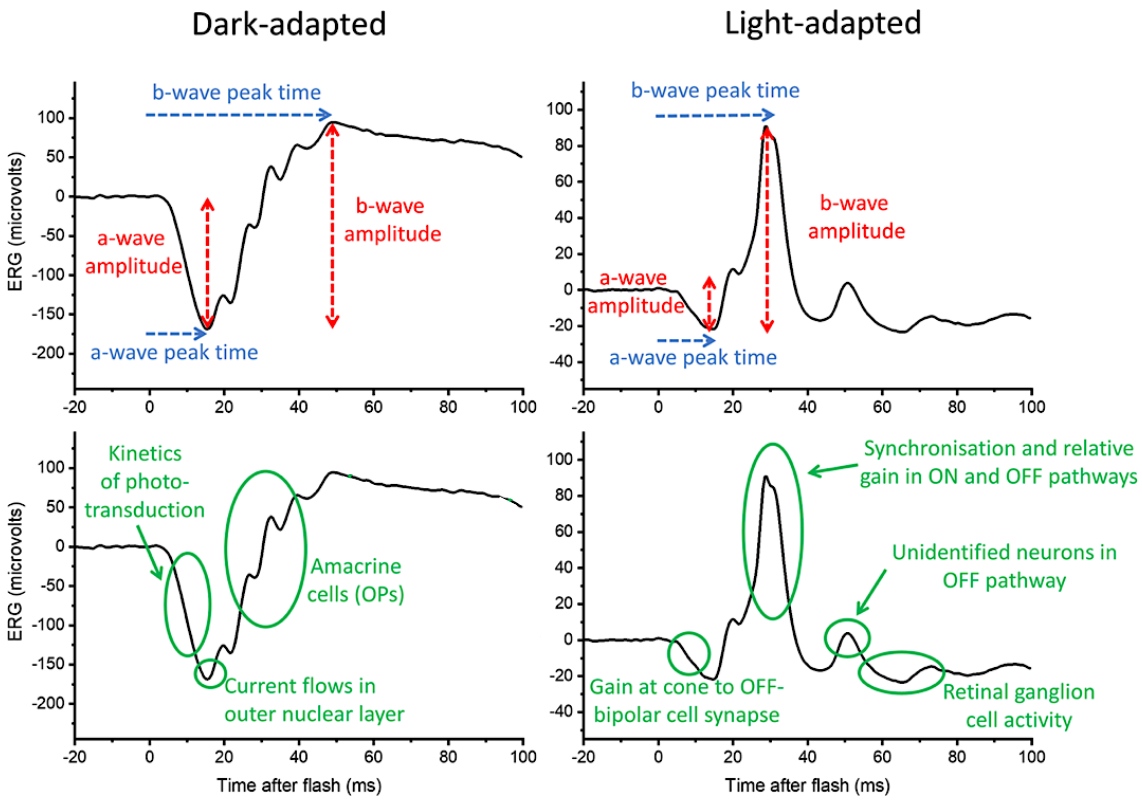

Figure 1.4. ERG response recorded from a healthy individual after both dark-adaptation (scotopic) and light-adaptation. Labels in the upper panels highlight the quantitative parameters usually reported (a-wave and b-wave amplitudes and peak times); the oscillatory potentials (OPs) on the rising limb of the b-wave may be qualitatively evaluated or quantified. The lower panel highlight several components in the waveforms and the underlying retinal processes or neuronal origins. Adapted with permission from Omar A. Mahroo (Mahroo, 2023).

Full-field ERG responses are reduced in early stages of RP even when changes on clinical exam or imaging modalities are minimal (Figure 1.5). Traditionally, patients receiving ERG tend to have prior clinical evidence of RP (E. L. Berson, 1993; Eliot L. Berson, 2008). Nonetheless, ERG testing is helpful in confirming RP. In general, patients with early stages of RP have reduced and prolonged rod ERG responses and near normal cone responses (Gouras & Carr, 1964). With further progression, the rod and cone ERG responses diminish, prolong, and become non-detectable (Lam, 2005). The amplitude of the responses is more or less proportional to the area of functioning retina. In RP patients with moderate to severe disease, the responses are likely to be wholly extinguished (Figure 1.5). It is estimated that RP patients lose about 16-18.5% per year of ERG amplitudes on average (E. L. Berson et al., 1985). There is variation in rod and cone readouts depending on the genetic causation, but a consistent finding in virtually all kinds of RP and allied retinal degenerations is a decrease in the maximum amplitude of the phototransduction a-wave and a delay in cone b-wave implicit time (E. L. Berson et al., 1985).

Various parameters of ffERG response components such as peak time and amplitude have been studied extensively as outcome measures in natural history and clinical trials in RP patients (E. L. Berson et al., 1985; Birch et al., 1999; Park et al., 2014; Andreas Schatz et al., 2011; Schroeder & Kjellström, 2018). While b-wave amplitude is the most common ERG endpoint in patients with RP, a-wave amplitude can provide a direct measure of photoreceptor activity and may be useful in these patients (Birch et al., 2002). The intervisit variability of b-wave amplitude ranged from 25-110% (Birch et al., 1999; Sandeep Grover et al., 2003; Tzekov et al., 1998). In a 4-year student of 67 RP patients with detectable rod and cone full-field ERG responses by Birch et al., the percentages of RP patients with a decline in ERG amplitudes were 64% and 60% for rod

and cone responses respectively, and the mean annual increase of rod ERG threshold was 28% per year (0.14 log unit) compared to 13% per year (0.06 log unit) for cone ERG threshold (Birch et al., 1999). In another study in patients with RP, the threshold for significant decrease in b-wave maximum amplitude for light- and dark-adapted single flash and light-adapted 30 Hz flicker stimuli were 23-35%, 30-44% and 17-22%, respectively (G. A. Fishman et al., 2005).

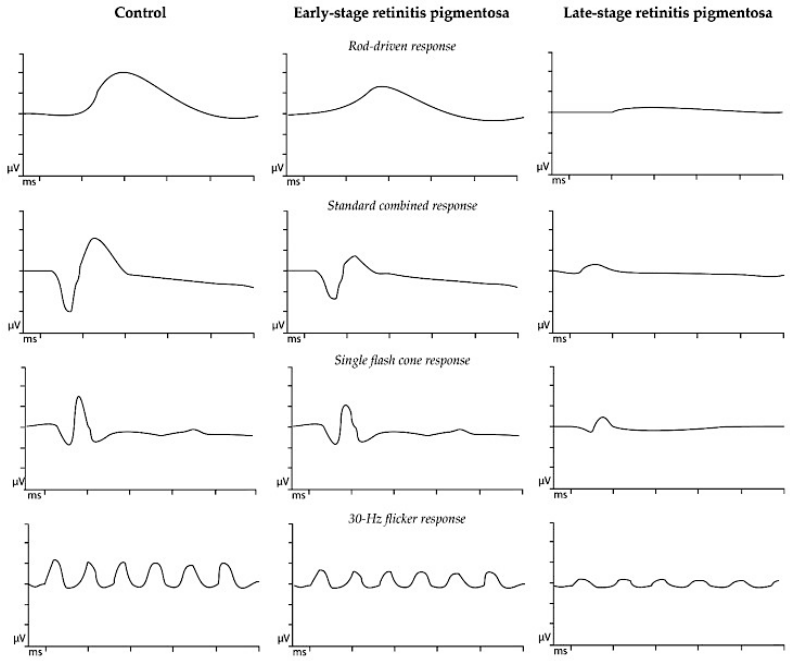

Figure 1.5. Example of full-field ERG recordings in a healthy patient and in patients with different disease stages of retinitis pigmentosa. Different stimuli are used to establish the diagnosis of retinitis pigmentosa, which is based on the guidelines of the International Society for Clinical Electrophysiology of Vision (ISCEV). In patients with advanced stages of diseases, rod-driven responses are severely diminished or even absent, whereas residual cone-driven responses may still remain. Reproduced with permission under Creative Commons CC-BY (Nguyen et al., 2023).

1.4.2.2 Multi-focal Electroretinography

This technique was developed by Sutter and Tran (Sutter & Tran, 1992) to provide a map of retinal function by simultaneously recording and calculating ERG signals from multiple retinal areas. Multifocal waveforms are not true direct recorded responses but

mathematical calculations of local ERG signals (Michael F. Marmor et al., 2003) of five concentric regions in the central retinal field surrounding the macula (Figure 1.6). The N1 and P1 components correlate with (but are not exact equivalents) of the a- and b-waves of the photopic full-field ERG (Maiti et al., 2011). The N1-wave is the initial negative deflection corresponding to cone photoreceptor cell activity, and largely measures outer retinal function. The P1-wave is the positive deflection following the N1-wave representing the depolarisation of inner retinal Muller, bipolar, and amacrine cells, providing a measure of phototransduction activity. The N1 amplitude is measured from baseline to the N1 trough, and the P1 amplitude is measured from the N1 trough to the P1 peak (Figure 1.6). The implicit time of N1 is measured from the onset of the stimulus to the N1 trough, and the implicit time of P1 is measured from stimulus onset to the P1 peak. An additional output unique to multifocal testing is the response density expressed as amplitude per degree area (nV/deg2), which is the summed response.

Multifocal ERG studies indicate decreased amplitudes and increased implicit times especially eccentric to the fovea in RP patients (Figure 1.7). The mean annual loss of mfERG amplitude in rings 3-5 were 6-10%, while the peak time remained stable (Ditta Nagy et al., 2008). However, another study concluded that loss of amplitude of a multifocal ERG test area is not a good predictor of visual sensitivity obtained with Humphrey visual field, but delayed timing of the test area appears to be an early indicator of local retinal damage to the cone system (D. C. Hood et al., 1998). There was a good correlation between the mfERG ring 5 amplitude and mixed rod-cone, cone, and 30 Hz flicker response amplitudes of ffERG. Significant mfERG responses were found to be present even in advanced cases with undetectable ffERG responses (Ditta Nagy et al., 2008).

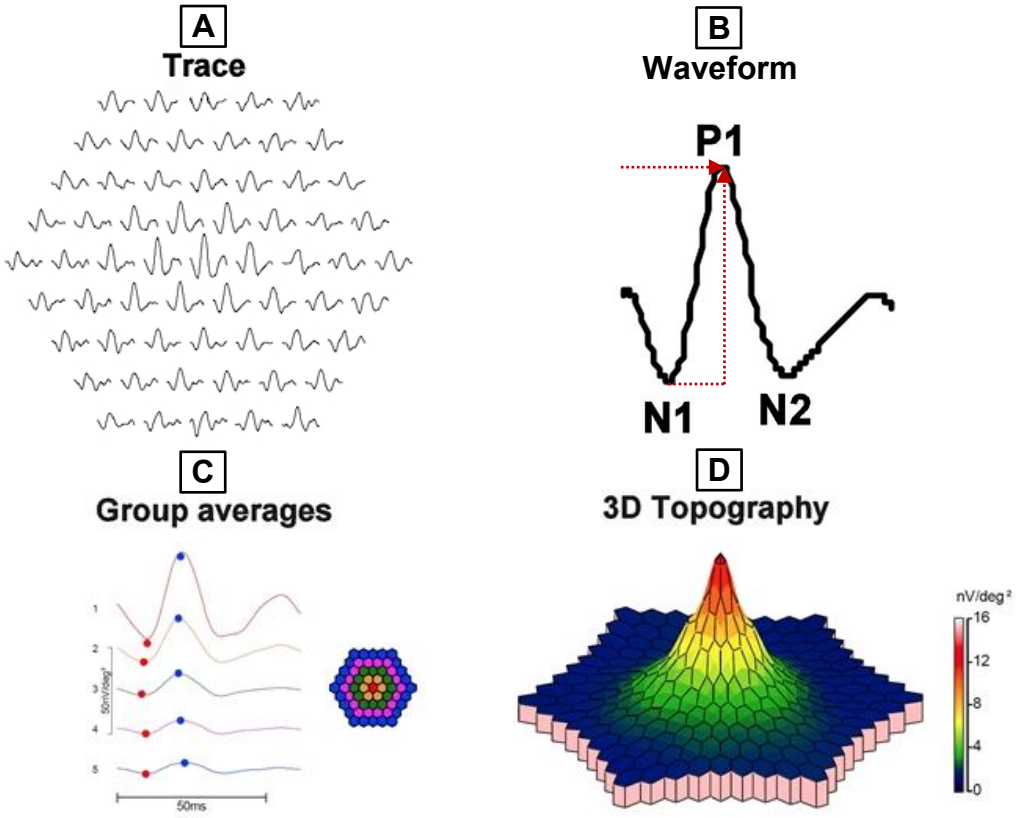

Figure 1.6. Example of a multi-focal recording obtained in a normal eye displayed in three different ways. The summations of local responses are calculated for five rings in the macular region with ring 1 representing < 2° field, ring 2 representing 2–5° field, ring 3 representing 5–10° field, ring 4 representing 10–15° field and ring 5 representing > 15° field. (A) Traces from different retinal locations are arranged in an equidistant manner for clear visualisation and comparison. (B) mfERG waveform and peak definitions, N1, P1, and N2 as well as P1 amplitude (trough to peak, vertical arrow) and P1-peak latency (horizontal arrow) measures are indicated for one retinal local response. (C) The horizontal mfERG traces from the concentric hexagons are averaged within (D) five difference eccentricity ranges and arranged vertically from ring 1-5. Reproduced with permission from J. Jason McAnany (Mcanany et el., 2023).

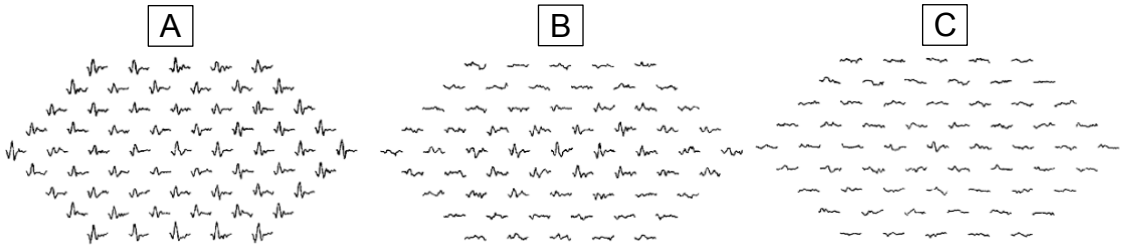

Figure 1.7. Traces of multifocal ERG arrays showing progression of responses with respect to different stages of retinitis pigmentosa. (A) Normal mfERG topography. The amplitude reduction on the left side, most prominent in the second element of the middle row, is caused by the optic disk. (B) In beginning stages of RP, the responses become smaller towards the periphery, and their peak implicit time is increased. (C) As RP progresses in severity, there remains some central response, but extinguished pericentral responses. Reproduced with permission from American Journal of Ophthalmology (Seeliger et al., 1998).

1.4.3 Visual Fields

One of the principal descriptors of visual function is the visual field, known as the area of a patient's subjective functional vision. Also known as perimetry, this exam is also useful for establishing baseline function and scope of vision, detecting pathologies, evaluating disease status, and determining progression or efficacy of treatment. The visual field of a person is defined as the area in which a person can see at a given moment relative to the direction of fixation, without head or eye movement (i.e., it defines the boundaries of the area beyond which nothing can be seen). A normal visual field extends more than 90° temporally, 60° nasally and superiorly, and 70° inferiorly (N. Wang et al., 2019). The visual fields of both eyes can overlap at the nasal side to form a binocular visual field of 210° horizontally and 130° vertically, with a nonoverlapping 30° area temporally in each eye (Figure 1.8). The most effective visual field of a single eye is within the central 30° of fixation (N. Wang et al., 2019), where the clear visual image and colour information can be provided, which is also a key area for modern visual field evaluation. The physiologic blind spot corresponds to the location of the optic disc, which has no photoreceptive function, and is located 10-20 degrees temporal to the point of fixation (Cassin, 1995).

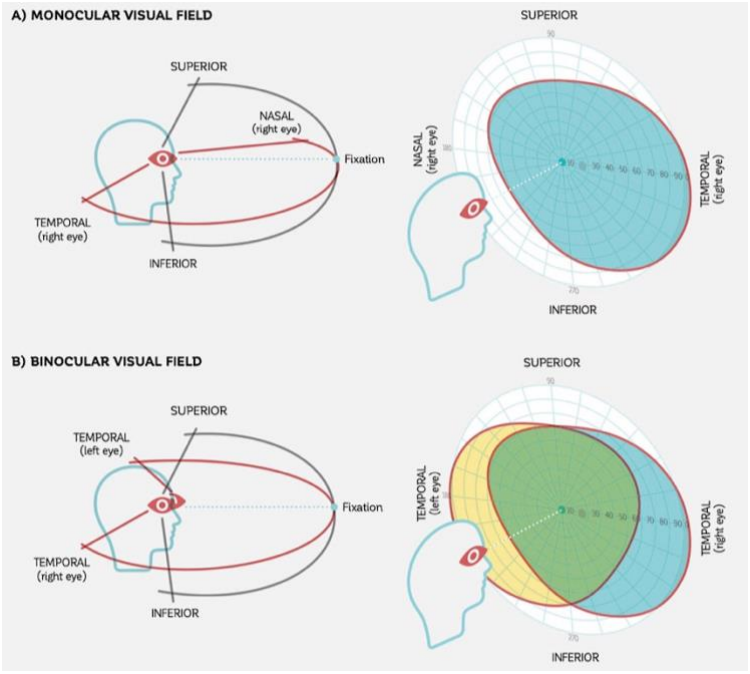

Figure 1.8. The spatial extent of a normal visual field. The monocular visual field of one eye is limited by the facial anatomy of the person with the eye socket, nose, brow, and cheekbones (A). The binocular visual field of two eyes overlaps in the central area (B). It contains input from both eyes, with integration and mapping of information from the two eyes, allowing for stereo acuity and depth perception. Reproduced with permission from Haag-Streit AG (Racette et. al, 2019).

Deviations can be either constrictions of the boundaries of the visual field, or depressions of sensitivity. Such depressions can be present throughout the visual field (widespread lowering of sensitivity) or localised in specific areas of the visual field (scotomas). Any damage to the outer areas of the retina (closer to the choroid) from a degenerative process, inflammation or trauma produces a scotoma that corresponds in size and location to the area of damage in the involved eye (N. Wang et al., 2019). This is known as focal pathology. A scotoma can be absolute or relative. The blind spot is an example of an absolute scotoma, in that the stimulus cannot be perceived no matter what kind of stimulation intensity, while a relative scotoma is an area where light sensitivity is relatively lower than normal, but a stimulus could be perceived with increased intensity. In 1901, Gonin (Gonin, 1901) was the first to describe different stages of progression in RP. As retinitis pigmentosa initially and primarily involves the retinal rods, the earliest perimetric sign is a characteristic ring scotoma occupying the midperiphery of the visual field (Ulrich, 2003). This defect usually starts as a group of isolated scotomas in the area 20 to 25 degrees from fixation which gradually coalesce to form a partial and finally a complete ring (Ulrich, 2003). The outer edge of the ring expands peripherally at a fairly rapid pace while the inner margin contracts very slowly toward fixation. Long after the entire peripheral field is gone, there remains a small oval remnant of intact central field, resembling the terminal defect of glaucoma (N. Wang et al., 2019). There are numerous variants of typical retinitis pigmentosa with occasional early macular involvement and central scotoma. It is key to note that due to spatial reversal, destruction of tissue in the inferior nasal portion of the fundus, for example, produces a corresponding defect in the superior temporal field (Cassin, 1995).

In visual field testing, decibels (dB) is the main unit of comparing the intensity of light to the maximum possible light intensity the machine can produce and is based on log

units (Anderson, 1982). For example, 10 dB means the light is 1/10th as bright as the brightest light, 20 dB means the light is 1/100th as bright. The higher the number of dB, the dimmer the stimulus.

There are two types of visual field tests commonly used in the clinic. Depending on whether or not the stimulus moves, the test can be classified as static or kinetic and depending on whether the stimulus is moved by hand or by a computer, as manual or automated. The Goldmann perimeter is a widely used manual kinetic perimeter whereas the Humphrey perimeter is a popular automated static perimeter. In fact, both perimeters have the capability of doing both static and kinetic tests but in practice they are used as described above. In both cases, the patient subjectively indicates by pressing a button if they are able to see the stimulus.

1.4.3.1 Humphrey Visual Field

The Humphrey visual field (HVF) Analyzer (HFA) is a fully automated perimeter, that uses a pre-programmed algorithm to quantify a patient's sensitivity in a standardized manner. Patients are shown stimuli of varying sizes and intensity and press a response button to indicate when they can see them. The minimum light intensity that can be seen defines the patient's sensitivity to light, or the threshold (Figure 1.9). In most clinical settings, the Swedish interactive thresholding algorithm (SITA) standard is the strategy most employed. Defects show up as varying shades between white and black, where darkening of the area indicates increasing severity of visual loss. Humphrey visual field tests focus on the area within 30 degrees of fixation as most of the retinal ganglion cells are distributed in this area (Figure 1.10) (Yi et al., 2010), so test protocols include either the central 30-2, 24-2, or 10-2 degrees of the field (Xiaoming C, 2000). The first number of the protocol refers to the number of degrees of field tested from the point of fixation. The 24-2 eliminates the most peripherical ring of test locations compared to 30-2, which

can be useful where the peripheral ring provides less reliable data, and the 10-2 is ideal for patients with advanced visual field loss and can improve detection of progression by assessing a larger number of points within that 10° central island. The second number refers to the specific testing strategy employed. In the case of HFA, the "-2" typically denotes the SITA Standard testing algorithm, designed to provide a faster and more patient-friendly method of assessing the visual field compared to older strategies.

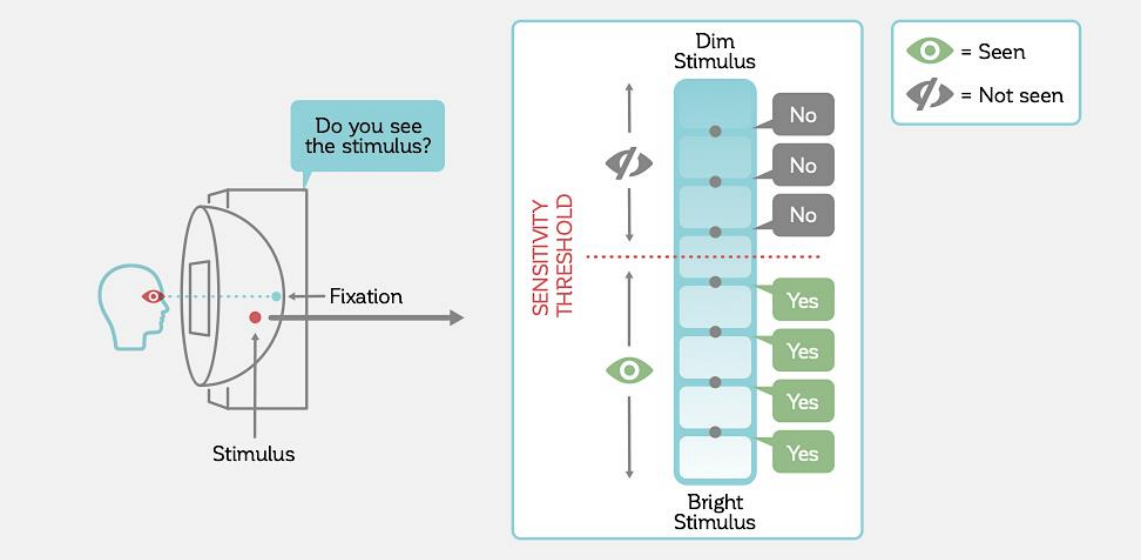

Figure 1.9. Sensitivity thresholds. The sensitivity threshold between seeing and non-seeing for stimuli of different intensity presented against a fixed background illumination at a given location in the visual field provides one data point on the hill of vision. Reproduced with permission from Haag-Streit AG (Racette et. al, 2019).

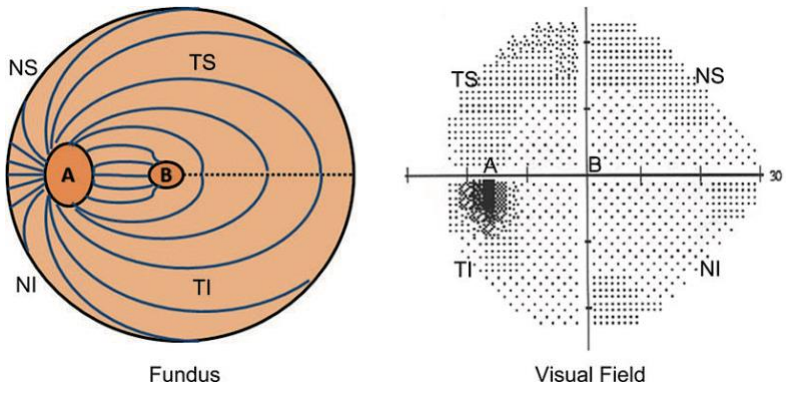

Figure 1.10. Correspondence between retinal nerve fibres and visual field. With the central fixation point as the centre, the horizontal and vertical midlines divide the visual field into four quadrants. The temporal, nasal, superior, and inferior quadrants of the visual field correspond to the nasal, temporal, inferior, and superior quadrants of the retina, respectively, with the macular fovea as the centre. NS: Nasal Superior, NI: Nasal Inferior, TS: Temporal Superior, TI: Temporal Inferior, A: Optic Disc, B: Macula. Reproduced with permission from Springer Nature Singapore (Ma et al., 2019).

The HVF printout contains a few relevant visual field analytics for the assessment of retinitis pigmentosa (Figure 1.11) The actual sensitivities of each testing point during the threshold test, expressed in decibel (dB) values, are printed in a plot called a numeric printout. The decibel scale is used as it is intuitive to understand in clinical practice, and typically ranges from 0 dB to approximately 32 dB in the fovea (Anderson & Patella, 1998). The defect depths expressed in dB values are generated by a comparison between the detected sensitivity and the normal sensitivity at the same point of the corresponding age group, and are printed in a plot, called the total deviation numerical plot (Figure 1.11). The different dB values of sensitivity at each point are expressed by different grayscales, resulting in the grayscale plot. The bigger the dB value, the lighter the grayscale; the smaller the dB value, the darker the grayscale. A darker grayscale indicates a lower light sensitivity in this area (Figure 1.11). As visual field is a psychophysical test, the reliability of the HVF is dependent on voluntary patient cooperation, including patient energy levels, fixation, and focus. The false-positive response error score (FP) measures a patient's response even without seeing any stimulus. A high FP percentage indicates a "trigger-happy" patient. The false-negative response error score (FN) is used to assess the self-control and attention of a patient. The perimeter will present the brightest stimulus in an area for which the threshold value has been obtained, and it will register a FN response if the patient fails to respond, indicating distraction (N. Wang et al., 2019). The HVF also projects the stimulus randomly onto the physiological blind spot to assess the patient's gaze stability. If the patient responds to these stimuli, it will be recorded as a fixation loss (FL). These three scores (i.e. FP, FN and FL) should be below 25% (Figure 1.11) (Cassin, 1995). HVF results are also subject to learning effects where the patient's second exam will see a marked improvement resulting from familiarity with the test procedure. All of these quantifications are summarised as a visual field index (VFI) called mean deviation

(MD), which refers to the difference of light sensitivity between the tested eye and that of normal people from the same age group (Yuansheng Y, 2015). It is the weighted mean of the values at each point in the total deviation numerical plot, and is the primary metric used by specialists to assess functional loss of RP patients and track progression (Yuansheng et al., 2005). In normal eyes, MD fluctuates around 0 to -2 dB. The bigger the negative value, the more serious the visual field loss.

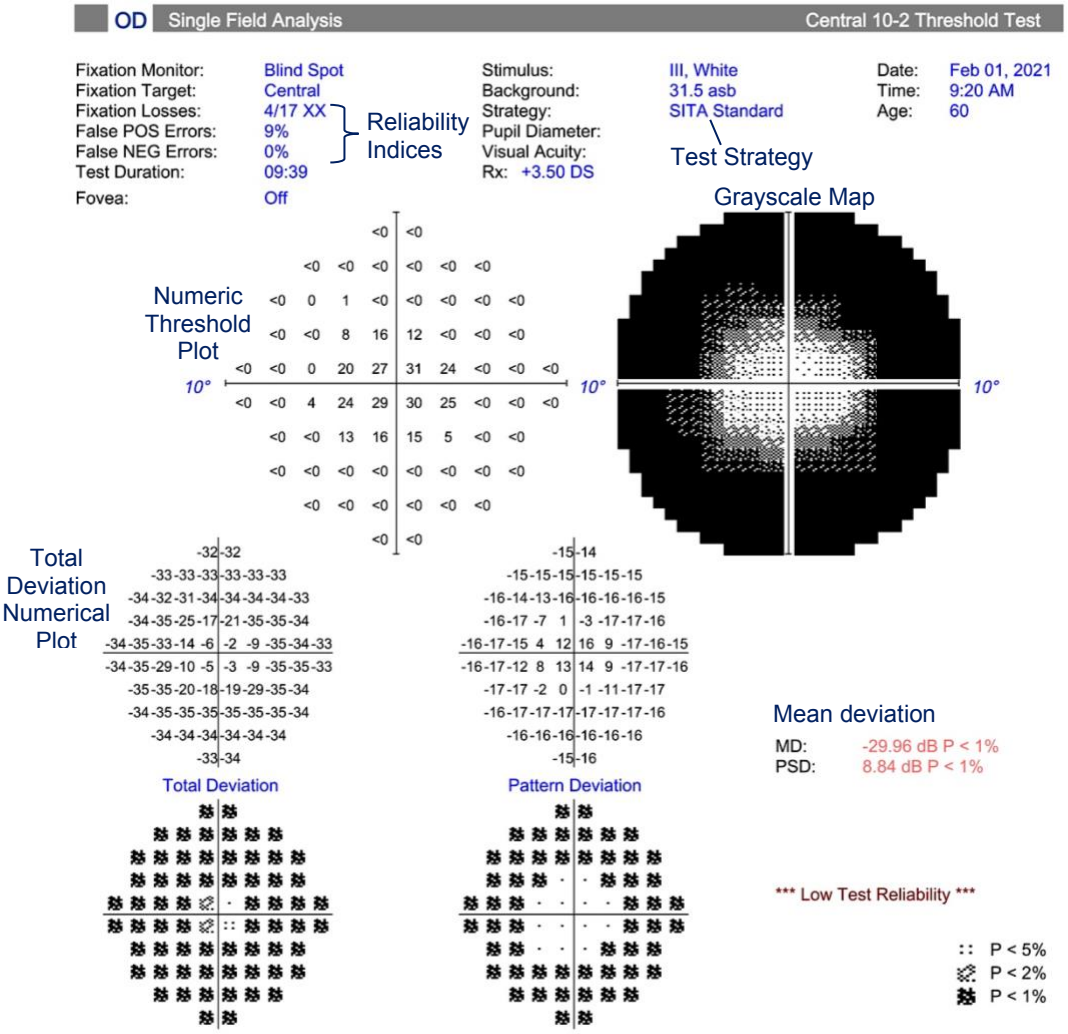

Figure 1.11. Single field analysis (SFA) printouts of STATPAC software analysis in Humphrey Field Analyzer (HFA). Regardless of the test mode utilised, the printout always contains general patient data, test pattern, strategy, reliability indices, gaze tracking record, and a series of analysis maps. This example uses a patient presenting with advanced RP, hence the use of a narrower testing strategy (10 degrees) to focus on the remaining 5 degrees of visual function. The mean deviation, the most used index in RP progression studies, is -29.96, indicating very limited functional visual field. Image obtained from study data.

Humphrey perimetry can be used to monitor the progression of RP because of its wide dynamic range of sensitivity at each test point (Figure 1.12). Visual sensitivity around the foveola is closely related to vision-related quality of life (Sugawara et al., 2011). A study by Iijima in 2012 found that in advanced RP, the Humphrey central 10-2 program may be more appropriate for determining visual sensitivity of RP patients compared with the Humphrey central 30-2, because, when they are initially seen by an ophthalmologist, many patients with RP still have residual visual fields with measurable sensitivity only inside the 10° visual field (Iijima, 2012), as seen with the example C in Figure 1.12. In a longitudinal study on patients with RP and choroideremia, the HVF 10-2 MD declined significantly in nearly 50% of patients ranging from -0.7 DB to -2.0 dB per year over 3.5 years of follow-up (Hirakawa et al., 1999). However, the rate of HVF 10-2 MD decline was -0.46 dB and -0.47 dB in two other reports on larger number of patients and longer follow-ups (Fujiwara et al., 2018; Sayo et al., 2017). It is also worth noting that short-term test-retest variability is higher in patients with RP compared with normal subjects regardless of sensitivity (Seiple et al., 2004).

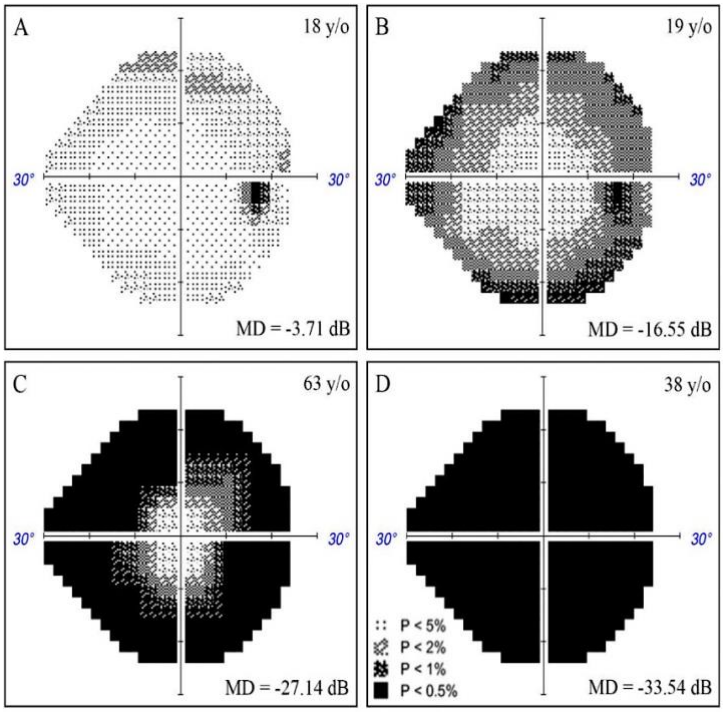

Figure 1.12. Humphrey Field Analyzer greyscale pattern and mean deviation in 4 patients with different stages of RP. (A) Very mild superior peripheral defect with mild MD loss in patient with early-stage RP. (B) Peripheral ring scotoma and moderately severe MD loss in patients with early macular involvement. (C) Dense scotoma with central island of vision (tunnel vision) limited to central 10 in a patient with advanced RP. (D) Total scotoma and profound MD loss in a patient with end-stage RP. Reproduced with permission from Springer Nature Singapore (Ma et al., 2019).

1.4.3.2 Goldmann Visual Field

The Goldmann visual field is a human-operated perimeter which tests the entirety of the visual field. It utilizes mobile targets of changeable size and luminosity that can be moved in all directions by the operator guiding a pantograph arm. A built-in telescope allows for the direct viewing of the patient's fixation. The pantograph arm moves across a paper chart on the operator side, allowing the operator to track the target position. The patient presses a buzzer when the target first becomes visible or disappears and reappears; this response is used to determine the boundaries of the visual field for that particular target and is called an isopter (N. Wang et al., 2019). An isopter (i.e., line of equal visibility) is the threshold border between seeing and non-seeing areas for that specific light sensitivity, similar to contour lines denoting equal elevations on a map (Figure 1.13). Each isopter is colour-coded to the size and intensity of the stimulus used. The stimulus size varies from 0 to V, with the areas of the light spots being 1/16, ¼, 1, 4, 16 and 64 mm^2 (Anderson, 1982). The intensity varies between 1 and 4 for each 5 dB change and further differs between a-e for smaller 1 dB changes (Table 1). In the current clinical standard, V4e is the largest and most intense target that maps the farthest peripheral vision, III4e is a middle-sized target that is used in the definitions for driving standard and legal blindness in Canada, and I4e, I3e and I2e are smaller sensitive stimuli useful for detecting field loss in the central 30 degrees of vision (Dersu et al., 2006; A. Wong & Sharpe, 2000; S. H. Wong & Plant, 2015). Table 2 summarises the normal boundaries of the isopters (Niederhauser & Mojon, 2002).

Where HVF's reliability relies on the patient, manual perimetry relies completely on the operation of the examiner. Patient attention and fixation is maintained by constant supervision and correction of the technician through the telescope. Inter- and intra-perimetrist variability is expected as the operator gains experience and modifies their

techniques, and as multiple operators handle a single patient over the course of their disease (Johnson et al., 2011).

Studies of treatments that aim to slow or reverse the progression of such retinal degenerative diseases have included manual kinetic visual field testing, such as with the Goldmann perimeter, to demonstrate efficacy (Bittner et al., 2015; Clemson et al., 2011; Ivandic & Ivandic, 2014; Koenekoop et al., 2014; Rotenstreich et al., 2013; Andreas Schatz et al., 2011; Testa et al., 2013). In RP patients, Goldmann perimetry can detect changes in vision over time (Fig. 1.14). Test-retest variability of visual field area using III4e and V4e targets in patients were reported to be 23.7% and 19.2-32.8%, respectively (Bittner et al., 2011). Studies with manual kinetic perimetry showed a mean of 4.6%-17% per year decline of the visual field area in patients with RP, with a mean residual VF half-life value of approximately 7 years (E. L. Berson et al., 1985; S. Grover et al., 1997; Massof et al., 1990; Ditta Nagy et al., 2008). Using annual rate of decline (9.4%) and test-retest variability, Calzetti and colleagues estimated that approximately 4.4 years is required to detect a significant change in visual field area using Goldman perimetry in patients with USH2A (Calzetti et al., 2018).

Table 1. Options for Goldmann kinetic stimuli.

Parameter	**Steps (smallest/dimmest to largest/brightest)**
Size	0, I, II, III, IV, V
Intensity (5 dB)	1, 2, 3, 4
Intensity (1 dB)	a, b, c, d, e

Table 2. Normal isopter position in the peripheral visual field in kinetic perimetry.

Isopter	**Normal Limits**
V4e	90° temporally and 60° in other quadrants
III4e	80° temporally and 55° in other quadrants
I4e	70° temporally and 50° in other quadrants
I3e	60° temporally and 45° in other quadrants
I2e	50° temporally and 40° in other quadrants

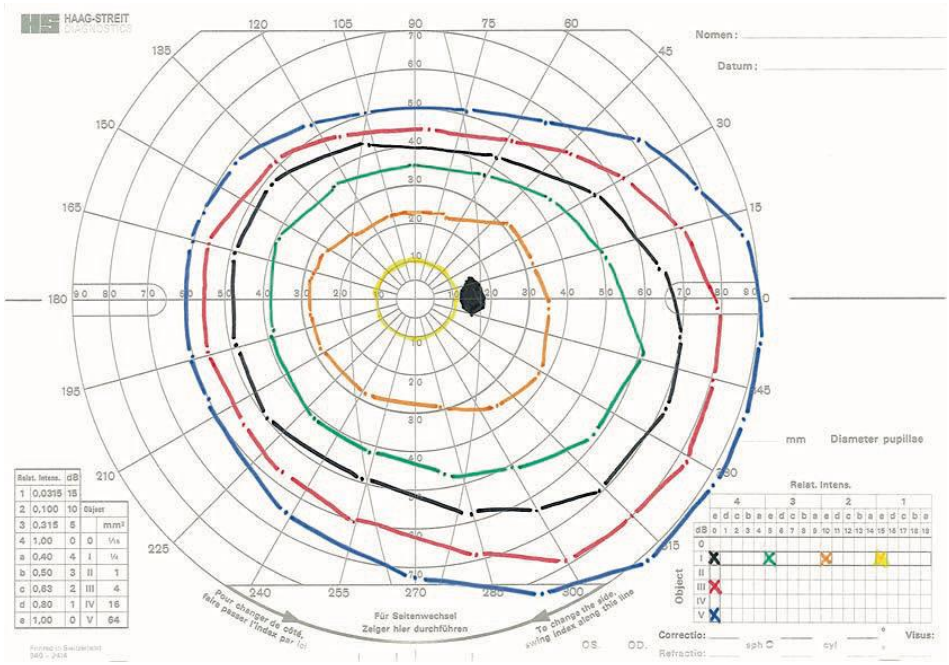

Figure 1.13. Normal Goldmann kinetic perimetry isopters for a healthy 20–30-year-old person. For a 50–60-year-old person, it is expected that the largest isopters decrease in radius by approximately 10°. Reproduced with permission from Springer New York (Talib et al., 2018).

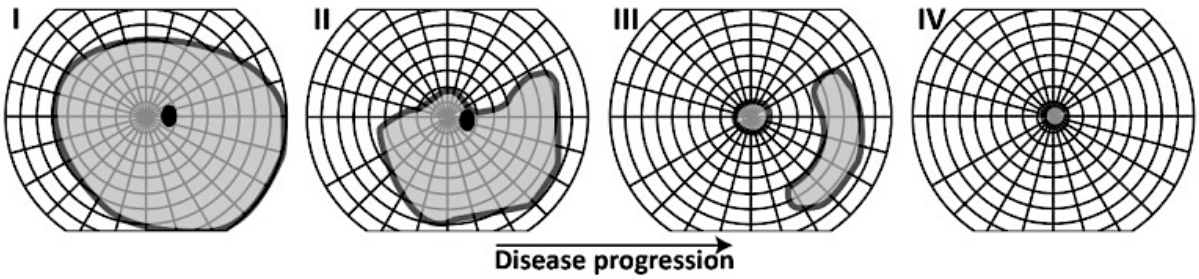

Figure 1.14. Illustrative example of a typical monocular visual field progression in a patient with retinitis pigmentosa using Goldmann kinetic perimetry. Visual fields can be within normal limits in early stages of disease (**I**), although visual field defects may already be present but not detectable within the used target stimulus. With time, constriction of the visual fields occurs, with defects typically being symmetric and expanding more rapidly outwards and slower inwards (**II**,**III**). Ultimately, a small central remnant of visual field may remain in end-stage retinitis pigmentosa, which is commonly experienced and known as 'tunnel vision' (**IV**). Note that the clinical course of visual field loss varies between individuals and may follow a progression pattern that is different from this illustration. Reproduced with permission under Creative Commons CC-BY (Nguyen et al., 2023).

1.4.4 Optical Coherence Tomography

Optical coherence tomography is a relatively new non-invasive imaging technique based on interferometry to capture three-dimensional cross-sectional images of the retina in high

resolution. The robust principles underlying the technology initially described by Huang et al. have continually been adapted and have since given rise to improved iterations such as spectral-domain OCT (SD-OCT), swept-source OCT (SS-OCT), and OCT angiography (OCTA) (D. Huang et al., 1991). This imaging modality allows the structure of the central 30° of the human retina to be observed *in vivo* on a micrometre scale. Its resolution is 1 to 2 orders finer than with the use of ultrasound, magnetic resonance imaging (MRI), or computed tomography (CT) (Fujimoto et al., 2000) , and allows for visualization of the distinct retinal layers. The received signals represent intensity versus wave number and are processed by inverse Fourier transformation into electric field magnitude (i.e., reflectivity) versus sample depth (Boon & Wijnholds, 2018). These individual depth profiles are called A-scans. A-scans acquired along one lateral direction form B-scans. SD-OCT has a much higher signal-to-noise ratio and a better depth resolution than time domain OCT and is therefore the predominantly used OCT technology in current clinical practice (Theelen & Teussink, 2018). An OCT b-scan of a healthy human retina obtained with SD-OCT is displayed in Figure 1.15. These images are displayed in log-scale intensity, while the original values are a measure of the number of photons reflected (backscattered). The different appearance of retinal layers is caused by the following optical effects (Lujan et al., 2011):

1. Differences in the refractive indices at the interface between two materials cause reflectance.
2. Diffuse reflective properties of tissues.
3. Angle between optical surfaces and incident OCT beam.
4. Birefringence, i.e., reflectivity is dependent on the light polarization state.

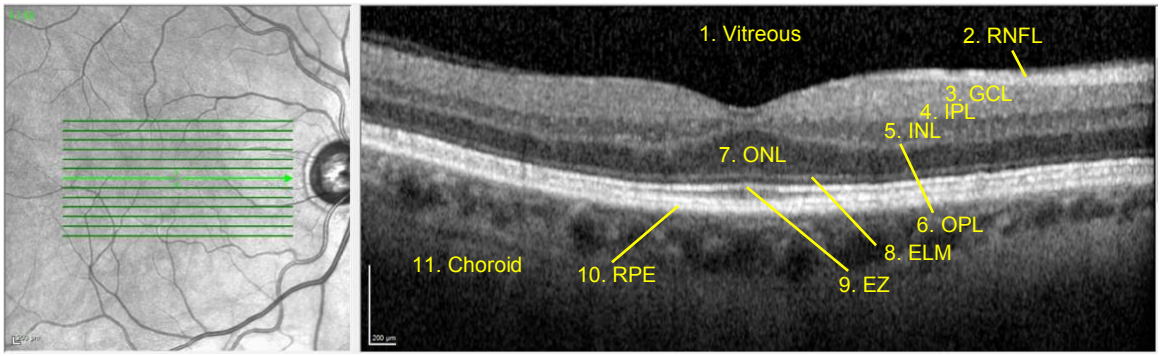

Figure 1.15. Fovea-centred SD-OCT scan of a healthy eye, showing various optical layers of the retina. (Left) Enface fundus image. Each B-scan cross-section is represented by a green line, with the brightest line indicating which cross-section is being examined on the right. In this example, the centremost foveal b-scan is being examined. (Right) In the cross-section, lighter pixels represent higher backscattering (i.e., reflectivity). Vitreous (1), retinal nerve fibre layer (2), ganglion cell layer (3), inner plexiform layer (4), inner nuclear layer (5), outer plexiform layer (6), outer nuclear layer (7), external limiting membrane (8), ellipsoid zone (9), retinal pigment epithelium/Bruch's membrane (10), choriocapillaris and choroid (11). The retina is displayed anatomically incorrect for better visualization of the layers; in reality the retina is flatter. The scale bar is shown on the bottom left. Image obtained from study data.

The OCT has been used to characterize features of the natural history of RP such as thinning of the neurosensory retina, disruption and loss of the ellipsoid zone (EZ) (Figure 1.15), loss of choroidal vasculature, and cystoid macular oedema (CME). OCT performed early in the disease course can show disorganization of the outer retinal layers. With disease progression, decreased thickness of the outer nuclear layer can be observed. Late stages of RP are characterized by the complete loss of both the outer segment and the outer nuclear layer, with the inner retina layers remaining relatively well preserved. Sandberg *et al.* first described a correlation between best corrected visual acuity (BCVA) and total retinal thickness in a large cross-sectional cohort of patients with RP (Michael A. Sandberg et al., 2005). Their study found that patients with thinner retinas on time-domain OCT (TD-OCT) frequently had poorer BCVAs, suggesting that retinal thickness could be used to monitor the natural history of disease progression. While some studies have disagreed with the correlation between total retinal thickness and BCVA, this study

presented the basis for future studies that expanded analysis to specific layers within the neurosensory retina (Battu et al., 2015; Wen et al., 2012; Witkin et al., 2006). Subsequent studies evaluated the correlation between the thicknesses of individual layers of the retina and measurements of retinal function such as visual field and electroretinography. Several reports assessing measurements of the inner retina have expressed conflicting increases and decreases in thickness with disease progression. (Tomas S. Aleman et al., 2007; Donald C. Hood et al., 2009; Milam et al., 1998; Santos et al., 1997; Vámos et al., 2011; Wen et al., 2012). In contrast, measurements of outer retinal layer thickness were found to be more reflective of disease progression. Witkin *et al.* demonstrated that foveal outer segment (OS) thickness could be used to estimate photoreceptor loss (Witkin et al., 2006). Additional studies compared the OS thickness and the outer retinal thickness, defined as the combined thickness of the RPE, EZ, ONL, and OPL, with functional measurements such as visual field and ERG (Wen et al., 2012), and found that the correlation between functional testing and retinal thickness was more sensitive outside of the central 30 degrees. However, most recently transverse measurements of the EZ line have been integral in evaluating disease progression and photoreceptor integrity (Spaide & Curcio, 2011; Staurenghi et al., 2014). It is widely accepted that the EZ band contracts centripetally in RP and the reduction in its boundary limits is well correlated with disease progression (Cai et al., 2014; Dagnelie, 1990a). The position at which the EZ band disappears is a structural marker for the edge of the functional visual field, demarcating a significant decrease in retinal sensitivity (Donald C. Hood et al., 2011). A longitudinal study on 81 patients with RP over 3 years showed a mean horizontal EZ loss of 140 µm (5.2%) per year with a test-retest variability of 74 µm (Cabral et al., 2017). EZ length measurements show approximate annual progression rates of 3-5% for autosomal dominant RP (Cai et al., 2014; Sujirakul, Lin, et al., 2015) and 7-9% for X-linked RP

(Birch et al., 2013; Cai et al., 2014). Birch *et al*. demonstrated that the rate of decline in the EZ line width was consistent with the rates of change reported for visual fields and full-field electroretinograms (ffERG) in patients with RP (Birch et al., 2013). The intersessional repeated variability of EZ line width measurements was found to be lower than these functional assessments, making it more useful in reliably detecting small changes in progression over short intervals (Birch et al., 2013). Given the phenotypic heterogeneity of RP, quantifying the progressive loss of the EZ line width can be used to characterize the natural disease progression of different aetiologies of RP on a gene-by-gene basis. However, a limitation of SD-OCT is that the scope of view restricts the scans to the central 30° of retina. This creates difficulty in monitoring patients with less advanced stages of RP, requiring newer OCT techniques such as SS-OCT to image a wider field (Rithambara Ramachandran et al., 2013; V. K. L. Takahashi, Takiuti, et al., 2019). Additionally, the presence of cystoid macular oedema and other secondary retinal pathology can distort measurements of retinal thickness and obscure visualization of the EZ band, limiting accurate assessment of disease progression.

1.4.5 Fundus Autofluorescence

Fundus autofluorescence (FAF), classically using blue-light excitation, is a non-invasive imaging technique using either a fundus camera or an OCT. It can give indirect information on the level of metabolic activity of the RPE through visualizing fluorophores, such as lipofuscin granules, which accumulate subretinally due to RPE dysfunction as a by-product of 11-cis-retinal and constant phagocytosis of shed photoreceptor outer segments (Delori et al., 1995; Schmitz-Valckenberg et al., 2008; Yung et al., 2016). It is estimated that more than 3,000,000,000 discs are phagocytosed during a human lifetime (Schmitz-Valckenberg et al., 2008). Thus, production, phagocytosis, and degradation of the discs are physiologic processes. However, the outer

segments of photoreceptors that degenerate in response to oxidative or age-related stressors are less susceptible to degradation by lysosomal enzymes, and thus lipofuscin accumulates (Feeney-Burns et al., 1980; Terman & Brunk, 2006). A normal FAF pattern is characterized by a physiological foveal hypo-autofluorescence from absorption of the short-wavelength excitation light by lutein and zeaxanthin (Menghini et al., 2020). Several FAF patterns are considered typical in RP, such as a hyper-autofluorescent ring or an abnormal central hyper-autofluorescence (Duncker et al., 2013; Lima et al., 2012; Robson et al., 2008). This hyperautofluorescent ring (HAR), also named the Robson-Holder ring, delineates the border between the normal and disrupted EZ, supported by OCT imaging (Figure 1.16). Significant loss of photoreceptors will be found outside the ring compared to inside in. The size of the ring negatively correlates with the remaining visual function, correlating with ellipsoid zone length defects observed by OCT (Figure 1.16). In a cohort of patients with RP, the mean external horizontal and vertical dimension of the FAF HAR was reported to decrease by 2.47% and 2.12%, 4.1% and 6.05% and 7.85% and 6.97% at 12, 24, and 36-month follow-up, respectively (Lima et al., 2012). Other authors reported the annual decline rate of horizontal and vertical HAR diameter in patients with RP to be 149 ± 15 μm and 120 ± 14 μm, respectively (Cabral et al., 2017).

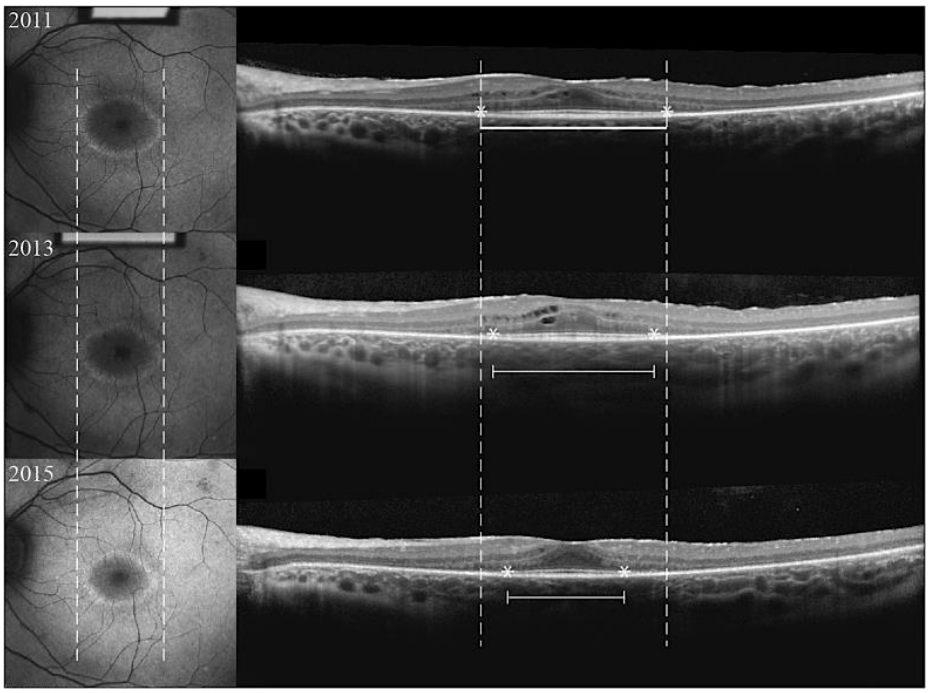

Figure 1.16. Progressive changes in a patient with retinitis pigmentosa via fundus autofluorescence imaging. Longitudinal SD-OCT and FAF images of a patient with retinitis pigmentosa. The association between the pattern of FAF and the residual area of the ellipsoid zone is shown. FAF images (left column) show characteristic hyperautofluorescent rings and SD-OCT (right column) images visualize the EZ line. Note that outside of the hyper-autofluorescent ring, the EZ line is not visible. This corresponds to the nasal and temporal borders of the hyper-autofluorescent ring. Solid lines; sample measurement. Dashed lines; initial measurement. Asterisk; endpoints on EZ-line. Reproduced with permission under Creative Commons CC-BY (Cabral et al., 2017).

1.5 Treatment of Retinitis Pigmentosa

Though retinitis pigmentosa as a clinical entity was introduced in 1853, there is still no established standard treatment modalities for this disease. The large heterogeneity associated with RP has made effective therapies elusive. Currently therapeutic strategies can be classified into photoreceptor rescue (or neuroprotective) treatments, e.g., gene therapy and vitamin/protein supplementation) and vision restoration (e.g., artificial prostheses, cell-based therapy, and optogenetics). Several studies have evaluated the use of nutritional and vitamin supplementation, particularly vitamin A (15,000 IU/day) and lutein (12 mg/day) (Aonuma et al., 1997; Bahrami et al., 2006; El-Hifnawi et al., 1995; Kiuchi et al., 2002; T. Li et al., 1998; Pasantes-Morales et al., 2002; Zhao et al., 2019).

Although early trials reported clinical benefits, later studies have shown no detectable changes or efficacy of such therapies in slowing disease progression (T. S. Aleman et al., 2001; Frasson et al., 1999; Organisciak & Bicknell, 1992; Pawlyk et al., 2002). Furthermore, vitamin A could pose a risk as some cases of suspected RP can present similarly to Stargardt disease, which is caused by mutations in the ABCA4 gene that result in vitamin A metabolism dysfunction, leading to the accumulation of the A2E by-product and lipofuscin deposits in the macula (Tanna et al., 2017).

1.5.1 Gene Therapy for Retinitis Pigmentosa

To date, only one gene-based treatment has been approved for the treatment of RPE65-associated retinopathy. No universally accepted therapies are currently available for RP, but many trials are ongoing, evaluating different therapeutic approaches. Neuroprotection, stem cells, gene therapy, optogenetics, electrical stimulation and retinal prosthesis represent possible potential future approaches to slow down the progression of the disease or to restore visual function in patients affected by retinal dystrophies (Acland et al., 2001; Bainbridge et al., 2008; Busskamp & Roska, 2011; Dacruz et al., 2013; Falsini et al., 2016; He et al., 2014; Humayun et al., 2012; S. G. Jacobson et al., 2013; Kitiratschky et al., 2014; Léveillard et al., 2014, 2004; A. Schatz et al., 2011; Strettoi et al., 2010; Uy et al., 2013; A. F. Wright, 2015; Zrenner et al., 2011).

Gene therapy is the most promising approach as the retina's immune-privileged environment, as well as its accessibility for surgical procedures, makes it a suitable candidate for such treatments (Prado et al., 2020). Therapies can be delivered to the subretinal space through viral vectors, commonly adeno-associated viruses (AAVs), to provide a functional copy of a gene (augmentation) or to correct a mutation (editing)

(Planul & Dalkara, 2017). Table 3 highlights several completed and ongoing clinical trials evaluating gene therapies for RP.

Table 3. Selected interventional therapy clinical trials for retinitis pigmentosa.
This table highlights several completed and ongoing clinical trials evaluating new therapies for specific genotypes of RP. Current trials use gene augmentation, silencing, editing, optogenetics, and stem cell replacement approaches. Reproduced with permission from Jobson Medical Information LLC (Jimenez-Davila et al., 2022)

Clinical Trial #	Inheritance	Gene	Phase	Status	Vector	Administration Route	Country	Sponsor
Gene Therapy								
NCT03328130	arRP	PDE6B	I/II	Recruiting	AAV2/5	Subretinal	France	Horama SA
NCT03252847	XLRP	RPGR	I/II and II/III	Active, not recruiting	AAV2/5	Subretinal	US/UK	MeiraGTx Holdings/Janssen
NCT03316560	XLRP	RPGR	I/II	Recruiting	AAV2	Subretinal	US	AGTC
NCT04850118	XLRP	RPGR	II/III	Not yet recruiting	AAV2	Subretinal	US	AGTC
NCT03116113	XLRP	RPGR	I/II	Completed	AAV8	Subretinal	US/UK	Nightstar
NCT04123626	adRP	RHO (Pro23His)	I/II	Recruiting	QR-1123	Intravitreal	US	ProQR Therapeutics NV
NCT00999609		RPE65	Completed	FDA-Approved	AAV2	Subretinal	US	Spark
NCT03374657	arRP	RLBP1	I/II	Recruiting	AAV8	Subretinal	Sweden	NOVARTIS
NCT01482195	arRP	MERTK	I	Completed	AAV2	Subretinal	Saudi Arabia	King Khaled Eye Hospital
Usher Syndrome								
NCT01505062	arRP	MYO7A	I/II	Terminated	N/A	Subretinal	US	Sanofi
NCT03780257	arRP	USH2A	I/II	Active, Not yet recruiting	QR-421a	Intravitreal	US	ProQR
Stem-Cell Therapy								
NCT02320812	RP		II	Completed	Human retinal pro-genitor cells	Intravitreal	US	jCyte
NCT04604899	RP		II	Active, not recruiting	Human retinal pro-genitor cells	Intravitreal	US	jCyte
NCT02464436	RP		I/II	Recruiting	Human retinal pro-genitor cells	Subretinal	US/UK	ReNeuron
NCT04284293	RP		I	Recruiting	CNS10-NPC	Subretinal	US	Cedars-Sinai Medical Center
NCT04925687	RP		I	Recruiting	Autologous CD34+	Intravitreal	US	University of California, Davis
Optogenetics								
NCT02556736	RP		I/II	Active, not recruiting	AAV2	Intravitreal	US	Allergan
NCT03326336	RP		I/II	Recruiting	AAV2	Intravitreal	US, UK, France	GenSight
NCT04278131	RP		I/II	Recruiting	AAV	Intravitreal	US	Bionic Sight
NCT04945772	RP		II	Recruiting	AAV2	Intravitreal	US	Nanotherapeutics

1.5.2 Clinical Trial Endpoints

Choosing appropriate functional and structural endpoints is a crucial step in designing clinical trials. A clinically meaningful endpoint is used to determine whether an intervention being studied exhibits substantial evidence of efficacy (Aronson, 2008; Biomarkers Definitions Working Group., 2001). Clinically meaningful endpoints acceptable to the Food and Drug Administration (FDA) and European Medicines Agency (EMA) and used in inherited retinal disease clinical trials (Csaky et al., 2017) include the mean change or mean rate of change in:

1. Best corrected visual acuity (BCVA) (Beck et al., 2007)
2. Visual field sensitivity (including analysis of hill of vision volumes) (Chew et al., 2019; Weleber et al., 2015)
3. Retinal sensitivity measured by full-field stimulus testing (FST) (Roman et al., 2007)
4. Multi-luminance mobility tests (MLMT)

A surrogate endpoint, as defined by the FDA is a biomarker that is 'reasonably likely, based on epidemiologic, therapeutic, pathophysiologic, or other evidence to predict clinical benefit'. Surrogate endpoints used in IRD clinical trials include the mean change or mean rate of change in:

1. Electrophysiological measures of retinal function (Robson et al., 2018)
2. Optical coherence tomography (OCT) documenting the rate of photoreceptor loss (Birch et al., 2013; Hariri et al., 2016)
3. Hypo- or hyperfluorescent lesion size on fundus autofluorescence (Rupert W. Strauss et al., 2019).

Change in BCVA, specifically a loss or gain of 15 or more Early Treatment Diabetic Retinopathy Study (ETDRS) letters, is generally the most accepted visual function

endpoint by regulators and stakeholders and has been successfully adopted in large landmark multicentre clinical trials in ophthalmology over the last decades (Brown et al., 2009; Ferris et al., 1987; Heier et al., 2012; Rosenfeld et al., 2006). However, its value in assessing functional deficits in early disease and tracking small but important amounts of progression is limited (Dimopoulos et al., 2016; Lesmes et al., 2013; R. W. Strauss et al., 2016). Furthermore, in studies evaluating interventions targeted at halting disease progression, a lack of significant change in BCVA may serve as a promising indicator of therapeutic effectiveness.

The first phase 3 gene therapy trial for a form of RP was one which tested voretigene neparvovec (AAV2-hRPE65v2) in RPE65-mediated inherited retinal dystrophy. Individuals aged 3 years or older with a confirmed genetic diagnosis of biallelic *RPE65* mutations were eligible for enrolment if both eyes had visual acuity of 20/60 or worse and/or visual field less than 20 degrees in any meridian, as well as sufficient viable retinal cells as determined by retinal thickness on SD-OCT (>100 microns within the posterior pole). The primary efficacy endpoint was the change in multi-luminance mobility testing performance (change in lux score for the lowest passing light level) at 1 year relative to baseline. This test is designed to quantify participants' ability to navigate around obstacles in varying environmental illuminations, including very low light levels, integrating aspects of visual acuity, visual field, and light sensitivity. Secondary efficacy endpoints were FST testing and BCVA. Additional efficacy endpoints were visual field testing by GVF for kinetic fields and HVF for macular static fields with foveal sensitivity thresholds, score on the visual function questionnaire, contrast sensitivity, pupillary light reflex (PLR), and in-home orientation and mobility assessments. Both kinetic and static visual field tests were chosen as exploratory endpoints to evaluate alterations in function of different regions of the retina. This study

was a success and is now approved by the FDA as LUXTURNA™. Other published gene therapy trials target mutations in GUCY2D (Samuel G. Jacobson et al., 2021), MERTK (Ghazi et al., 2016) and RPGR (Cehajic-Kapetanovic et al., 2020). A recent trial used the optogenetics to target the inner retina in a patient with advanced RP (Sahel et al., 2021).

1.5.3 Common pathway of cell death

While the mechanisms that cause disease initiation are unclear, a large body of literature in cell culture and in various animal models of retinal degeneration suggests that apoptosis (Adler, 1996; Carmody et al., 1998; Green et al., 2000; Hafezi et al., 1997; Luthert & Chong, 1998; Nickells & Zack, 1996; Portera-Cailliau et al., 1994; Remé et al., 1998; Travis, 1998), necroptosis (Sato et al., 2013; I. A. Viringipurampeer et al., 2014; Ishaq A. Viringipurampeer et al., 2016), and inflammation are involved in cell death (Appelbaum et al., 2017; Murakami et al., 2018, 2015; Nagasaka et al., 2016; Ishaq A. Viringipurampeer et al., 2016). Apoptosis, or programmed cell death, is the body's natural mode of clearing away unwanted or damaged cells and is essential for normal development and homeostasis. It is mediated by a family of intracellular cysteine endopeptidases called caspases which trigger the apoptotic cascade, causing DNA fragmentation, cell-membrane blebbing, and eventually cell death (Elmore, 2007). Apoptosis itself is not a disease process but the induction of massive apoptosis may lead to dystrophic states. In the case of the photoreceptor cell, mutations in genes underlying the phototransduction cascade, the ability of opsin to respond to light, the integrity of the photoreceptor cell structure, and its ability to interact with either retinal pigment epithelial cells or bipolar cells, as well as a great many other things, could lead to an abnormal or dysfunctional photoreceptor cell, which then undergoes apoptosis. This scenario leads directly to tissue regression, retinal degeneration, visual cell loss, and blindness.

1.5.4 X-linked Inhibitor of Apoptosis (XIAP)

Addressing specific molecular defects with targeted therapies will be effective only for a limited patient population due to the multitude of genes associated with RP and the numerous possible mutations within each gene. Decreasing the susceptibility of retinal cells to multiple forms of cell death represents a broad-based therapeutic approach to different types of retinal disease, irrespective of the underlying genetic or environmental basis and pathology. XIAP is one such therapy which represents a potential means of targeting cell death mechanisms. XIAP directly interacts with and inhibits the activity of caspases 3, 7 (effector caspases) and 9 (initiator caspase) (Chai et al., 2001; Y. Huang et al., 2001; Riedl et al., 2001; R. Takahashi et al., 1998), and is recognised as the most potent anti-apoptotic member of the inhibitor of apoptosis (IAP) family (M. E. Wright et al., 2000). XIAP has also been demonstrated to control tumour necrosis factor (TNF) and receptor-interacting protein 3 (RIP3)-dependent inflammasome formation (Yabal & Jost, 2015; Yabal et al., 2014). A role for XIAP in inflammation is further suggested by the fact that patients with X-linked lymphoproliferative disease-2 or inflammatory bowel disease have mutations in the XIAP gene (Chirieleison et al., 2017). Furthermore, it has been suggested that XIAP and other members of the IAP family function as inhibitors of the ripoptosome, a RIP1-containing complex involved in necroptosis (Imre et al., 2011; Selmi et al., 2015; Tenev et al., 2011). The therapeutic potential of the XIAP protein is enormous for the treatment of neurodegenerative diseases such as RP, and for all disease where photoreceptor cell death via programmed cell death is concerned.

Given XIAP's role in caspase-dependent apoptosis, inflammation and caspase-independent necroptosis, XIAP has been tested in a wide variety of *in vivo* neuronal cell death models, including the 4-VO (vessel occlusion) model of forebrain ischemia (D. Xu et al., 1999), experimental models of Parkinson's disease (Crocker et al., 2003; Eberhardt

et al., 2000), cisplatin-induced ototoxicity (Chan et al., 2007; Cooper et al., 2006; Tabuchi et al., 2007) and age-related hearing loss (J. Wang et al., 2010). The Tsilfidis lab at the University of Ottawa Eye Institute has tested XIAP gene therapy in animal models of retinal ischemia, retinal detachment, Leber hereditary optic neuropathy (LHON) and glaucoma, and found it to be effective in protecting retinal ganglion cells and PRCs in all of these models (Leonard et al., 2007; Petrin et al., 2003; Renwick et al., 2006; Visuvanathan et al., 2022; Wassmer et al., 2020, 2017; Yao et al., 2011; Zadro-Lamoureux et al., 2009),. Importantly, the Tsilfidis lab and its collaborators have shown that XIAP is neuroprotective in 5 different animal models of RP. In the rd10 mouse model of RP, collaborator David Zacks (University of Michigan) showed that XIAP protected PRCs and increased the therapeutic window by preserving PRC viability until mutation-correction therapy could be applied (Yao et al., 2012). In two transgenic RP rat models that carry rhodopsin mutations (Leonard et al., 2007), Leonard et al. showed that XIAP delivery conferred dramatic long-term structural protection to PRCs. One of the models, the P23H rat, carries a mutation in the rhodopsin gene (Illing et al., 2002) that is responsible for the most common form of autosomal dominant RP in North America (Dejneka & Bennett, 2001). In this model, XIAP also conferred significant long-term functional protection. Degeneration occurs early in P23H rats, such that there is already considerable PRC loss prior to the XIAP therapy. Given the degeneration present when gene therapy is administered and the degree of protection that is seen at the end of the experiments, this suggests that very little degeneration is occurring after the administration of XIAP gene therapy and that XIAP can severely slow down or halt PRC degeneration, thus offering great promise for long-term protection of photoreceptors.

1.6 Overview of Thesis Research

IRDs, particularly retinitis pigmentosa, refer to a heterogeneous and clinically variable group of diseases that lead to a progressive and irreversible loss of vision. It is marked by clinical and genetic heterogeneity, with varying rates of vision loss and levels of disease severity, different modes of inheritance, and more than 100 genes whose mutations have been found to cause RP. There is currently no known cure for RP, but the recent ground-breaking FDA-approved gene therapy treatment (LUXTURNA™) for Leber's congenital amaurosis and RPE65 has shown dramatic improvements in vision and give promise that gene therapy is a viable strategy for treating inherited retinal diseases. Mutation-independent approaches targeting shared pathogenic mechanisms at early stages of disease poses an alternative strategy for developing therapies for larger segments of the RP population. It also offers a potential path for treatment for patients whose genotype for RP has not yet been identified. The X-linked inhibitor of apoptosis (XIAP) is a potent inhibitor of caspases which targets common pathogenic pathways driving retinal degeneration and offers the potential to provide functional rescue of vision independent of the genetic cause. It has shown success in various animal models with respect to retaining visual function but has not been tested in humans to date. The current study aims to support the effort to bring XIAP towards a clinical trial by conducting a retrospective cohort study of University of Ottawa Eye Institute RP patients. It is crucial to have data regarding RP natural disease history and appropriate outcome measurements from a gene-agnostic or pan-genomic standpoint given the heterogeneity of the disease.

The purpose of the study is to determine the size of the RP population in Ottawa, Canada and determine the rate of disease progression and correlations between structural and functional measures. An ideal diagnostic test would be capable of being easily and frequently measured, be repeatable with minimal variability, and be sensitive to change

over time and treatment effect (Lesmes et al., 2013; Meinert, 1986). Although this study aims to describe overall gene-agnostic rates of disease progression, differences between progression rates based on genetic inheritance information (where available) will be determined to inform researchers about expected efficacy endpoints for certain inheritance groups. Ultimately, the study will reveal if there is a sufficient patient population seen at the University of Ottawa Eye Institute for a clinical trial or if it will be necessary to expand to other test centres. We will determine how many patients are available, which types of test results are available for most patients, what is the frequency of these tests, observe patterns of progression, and assess which tests can provide reliable and sensitive measures of short-term changes to assess the safety and efficacy of XIAP gene therapy in a Phase I clinical trial.

Study Aims:

1. Multimodal structural and functional progression rates as well as correlations between them
2. The identification of the ideal diagnostic procedures for assessing short-term disease progression
3. An approximate timeline for disease progression sufficient to determine efficacy of a gene therapy
4. The determination of appropriate criteria for including or excluding candidates from participation in the forthcoming Phase I clinical trial of XIAP gene therapy

Chapter 2 Materials and Methods

2.1 Study design

This is a 10-year retrospective cohort study using medical records from The University of Ottawa Eye Institute (OEI) at The Ottawa Hospital (TOH) and Ottawa Hospital Research Institute (OHRI). The OEI's catchment area is the Champlain Local Health Integration Network (Figure 2.1) and parts of Western Quebec, and it sees 5,000 patients a month. The types of records that were accessed included electronic charts on EPIC electronic medical record (EMR) systems, physical charts located in locked offices at OEI, as well as diagnostic media on Synergy and Heidelberg HEYEX. The charts contain clinical and demographic information, including data on admission, patient providers, diagnoses, interventions, laboratory and diagnostic testing, and all testing ordered across various specialty departments at TOH. Patient medical record numbers (MRNs) were collected from EPIC and existing databases. The MRNs were kept only on the master enrolment list. All data was de-identified at the time of collection and before data analysis. None of the data presented in this study, including images and genetic testing results, is identifiable to individual patients. All files were exclusively stored in a secured folder on SharePoint on the hospital server. This study adhered to tenets of the Declaration of Helsinki and was approved by the research ethics and review board of the Ottawa Hospital. The review board waived the need for written informed consent, because the study design comprised a retrospective chart review.

Figure 2.1. Champlain Local Health Integration Network. This health network includes the entirety of Ottawa, as well as the surrounding western and eastern Champlain area. Reproduced with permission under Creative Commons CC-BY (Ontario, 2022).

2.2 Study participants

The study cohort was identified from the rosters of retinal ophthalmic specialists at the Ottawa Eye Institute and includes all patients with a diagnosis of retinitis pigmentosa from the 1st of January 2011 to the 5th of May 2021. No data reported in the chart before or after the specified dates was collected. EPIC's slicer dicer feature was used to generate a list of these patients using diagnosis keywords retinitis pigmentosa and retinal degeneration. Diagnosis of RP was based on clinical signs (characteristic bone spicule pigmentation, optic disc pallor, retinal vessel attenuation, visual field constriction, non-detectable scotopic electroretinographic waves) and, if available, confirmed by results of genetic analysis.

Personal health information and identifying information collected included:

1. Partial date of birth
2. Age
3. Sex
4. Date of first visit to the OEI
5. Follow-up frequency
6. Genetic form of disease, if known
7. Types and results of tests recorded (visual fields, OCTs, Fluorescein Angiography, Fundus Photos, ERGs, results of ophthalmology assessments including visual acuity), when and how often conducted and results from those tests)

2.3 Genetic Testing

Genetic testing data that was available in the MRN was conducted for consenting patients at the Children's Hospital of Eastern Ontario (CHEO) Genetics clinic. Blood was drawn and DNA was extracted and tested on the published retinitis pigmentosa genes at either CHEO Genetics diagnostic laboratory or SickKids Genome diagnostics laboratory in Toronto, Canada. Test methods included Next Generation sequencing and Sanger sequencing technologies. One study participant had genetic testing results from London Health Science Centre's General Genetics Clinic and its respective laboratory in London, Canada. There, a depletion/integrity panel was performed for the purposes of mitochondrial genome sequencing.

2.4 Diagnostic Testing

2.4.1 Electrophysiology

ERGs were performed at the OEI by licensed technicians according to ISCEV recommended standards and entered into the clinical record. The following protocols were typically used to record ERGs.

2.4.1.1 Full-field testing

Pupils were maximally dilated following topical application of 1% tropicamide and 10% phenylephrine. ERGs were recorded with Dawson, Trick, and Litzkow (DTL)-Plus (Diagnosys LLC, Lowell, MA, USA) micro-conductive thread electrodes secured on the temporal and nasal canthus with the fibre positioned at the lower limbal margin of the iris after topic anaesthesia with proparacaine hydrochloride 0.5% (Alcaine, Alcon, Fort Worth, TX, USA). Ganzfeld ERGs were recorded with the E^2ERG Espion system (Diagnosys LLC, Massachusetts, USA). Patients were dark adapted for a minimum of 20

minutes before any recordings were obtained. Scotopic responses were recorded using a stimulus of 0.01 cd·s/m^2 intensity. Stimulus flashes were presented every 15 seconds and 4 artifact-free ERG responses were then averaged. Scotopic combined rod/cone responses were then recorded using a stimulus of 3.0 cd·s/m^2 intensity. Stimulus flashes were presented every 15 seconds and 4 artifact-free ERG responses were then averaged. Photopic cone and photopic oscillatory potential responses were recorded using a stimulus of 3.0 cd·s/m^2 intensity against a 30 cd/m^2 background luminance following 10 minutes of light adaptation. Stimulus flashes were presented every 2 seconds and 4 artifact-free ERG responses were then averaged. 30Hz flicker responses were recorded using a stimulus of 3.0 cd·s/m^2 intensity against a 30 cd/m^2 background luminance, flickering at a 30 Hz rate. 15 artefact-free responses were averaged. The results were read by an experienced electrophysiologist (S.C.), who was blinded to clinical examination. Each response was assessed for abnormally reduced amplitude or prolonged implicit times against age-matched normative data established at the Ottawa Eye Institute's testing centre. Differences of 2 SDs or more were classified as abnormal. ERG marker table values were exported as Microsoft Excel files (Microsoft Corporation, Seattle, WA, USA). For this study, additional normative values per age group were obtained from N.D. of Diagnosys (Diagnosys LLC, Lowell, Massachusetts, USA).

2.4.1.2 Multi-focal testing

Multifocal ERGs were performed according to ISCEV recommended standards. Pupils were maximally dilated with 1% tropicamide and 10% phenylephrine before the electrophysiological examination. Patients underwent correction of their refractive error before testing. The Espion Profile Multifocal ERG system was used (Diagnosys LLC, Lowell, Massachusetts, USA). With a liquid-crystal display monitor having a luminance of 1000 cd/m2, a stimulus containing 61 hexagonal elements was projected

onto the central 30° area surrounding the fovea in the light-adapted eyes of study subjects. Micro-conductive DTL thread electrodes (Diagnosys LLC, Lowell, Massachusetts, USA) were draped on the conjunctiva at the inferior limbus following topical anaesthesia with proparacaine hydrochloride 0.5% (Alcaine, Alcon, Fort Worth, TX, USA). ERG signals were extracted using the fast m-transform algorithm (m = 14) in eight 30-second epochs. The results were read by S.C., who was blinded to clinical examination. Individual waveforms composed of trace arrays were assessed for abnormally reduced amplitude or prolonged implicit times, and ring-average analysis was assessed by using age-matched normative data established at the Ottawa Eye Institute's testing centre. Differences of 2 SDs or more were classified as abnormal. The lower limit of test reliability was set at 98%. Ring ratios were computed as the ratio of rings 1–5. Trace arrays, ring averages, and response density topographic maps were exported as Microsoft Excel files (Microsoft Corporation, Seattle, WA, USA). Normative values per age group were obtained from N.D. of Diagnosys (Diagnosys LLC, Lowell, Massachusetts, USA).

2.4.2 Perimetry

Perimetry data was obtained from the medical records of RP patients, de-identified and imported into a secure hospital SharePoint folder. Perimetry tests were conducted on RP patients by trained technicians using the following protocols.

2.4.2.1 Humphrey static visual field

Central 30-2, 24-2, or 10-2 SITA Standard protocols we carried out using the Humphrey Field Analyzer (HFA) (Carl Zeiss Meditec Inc., Dublin, CA). The targets consisted of Goldmann size III (0.43°) white lights presented on a 10 cd/m^2 illuminated white background. Patients were asked to press a response button to report the presence of target lights. Single field analysis read-outs were generated using the analyser's own statistical

software, STATPAC™ for Windows software package (version A3, Humphrey Instruments Inc), then de-identified and exported to a secure hospital SharePoint folder. Tests with any of the three reliability indexes (fixation losses, false positive, or false negative) above 25% were excluded. Clinical records were reviewed to exclude patients with other diseases that could cause visual field loss. Eyes with cataracts dense enough to affect vision at any time in the serial field testing were excluded. For the current study, the analysis focused on the global indices. The mean deviation (MD) of the visual field obtained using Humphrey perimetry autosoftware was used to evaluate the extent of visual field loss. This value was recorded in a Microsoft Excel (Microsoft Corporation, Seattle, WA, USA) spreadsheet.

2.4.2.2 Goldmann kinetic visual field

Goldmann visual fields were hand-drawn on a standard calibrated Goldmann perimeter (Haag Streit Group, Köniz, Switzerland). For the standard exam, four target sizes (V4e, I4e, I3e, and I2e) were used to estimate threshold boundaries. For the Esterman driver's exam, commonly requested for proof of minimum driving standards, the III4e target alone was used. In some cases, the III4e target was also incorporated into the standard exam. Patients were asked to press a response button to report when the target light was sighted. After completion of the exam, the visual field map sheet was scanned and imported as a digital image into the electronic medical record.

For this study, visual field sheets were only accessible through the electronic medical records, and the historic nature of the data meant that over the years the digital scans came in various resolutions and orientations. This made standardization of manual measurements extremely difficult. Without a scale on the sheet, we are only able to measure area in pixels, which we need to calculate as a percentage over the resolution of the scanned image. As this introduced a great deal of error, it was decided to take an

alternative approach by using the existing degree labels on the visual field map itself and counting the number of degrees manually. To my knowledge, I have not observed this approach in previous literature, but I hypothesized that this protocol may offer more value in analysis as it relates to the same anatomical boundaries of the ellipsoid zone and autofluorescence measurements from the central foveal b-scan on OCT. For example, if loss of ellipsoid zone length meant a total loss of photoreceptor cell bodies, then this would indicate a complete loss of function and would show as an absolute scotoma of similar length on GVF. Moreover, although a cartographic distortion arises from plotting data generated in a perimeter bowl in a flat visual field chart and the projection of visual field onto the retina is nonlinear in a schematic eye (Dagnelie, 1990b), the majority of studies on visual field progression in retinitis pigmentosa have not applied corrections to their perimetry data (E. L. Berson et al., 1985; Eliot L. Berson et al., 2002; S. Grover et al., 1997; Hafler et al., 2016; Holopigian et al., 1996; A. Iannaccone, 2004; Alessandro Iannaccone et al., 2004; D. Nagy et al., 2008; Michael A. Sandberg et al., 2007). Therefore, in order to remain consistent and to be able to compare results to previous ones, the same approach was taken.

Two iJCAPHO (International Joint Commission on Allied Health Personnel in Ophthalmology) certified OCT graders (L.K. and M.E.) independently calculated the central horizontal length of each isopter from the nasal to the temporal boundary. The degrees were subjectively determined with the use of a 10-tick ruler and any scotomas or islands of vision along this meridian were subtracted and added (Figure 2.2). Where a scotoma was drawn with a target size larger/brighter than the measured target, the scotoma length was included in the overall calculation (Figure 2.2). All values were recorded in a Microsoft Excel spreadsheet.

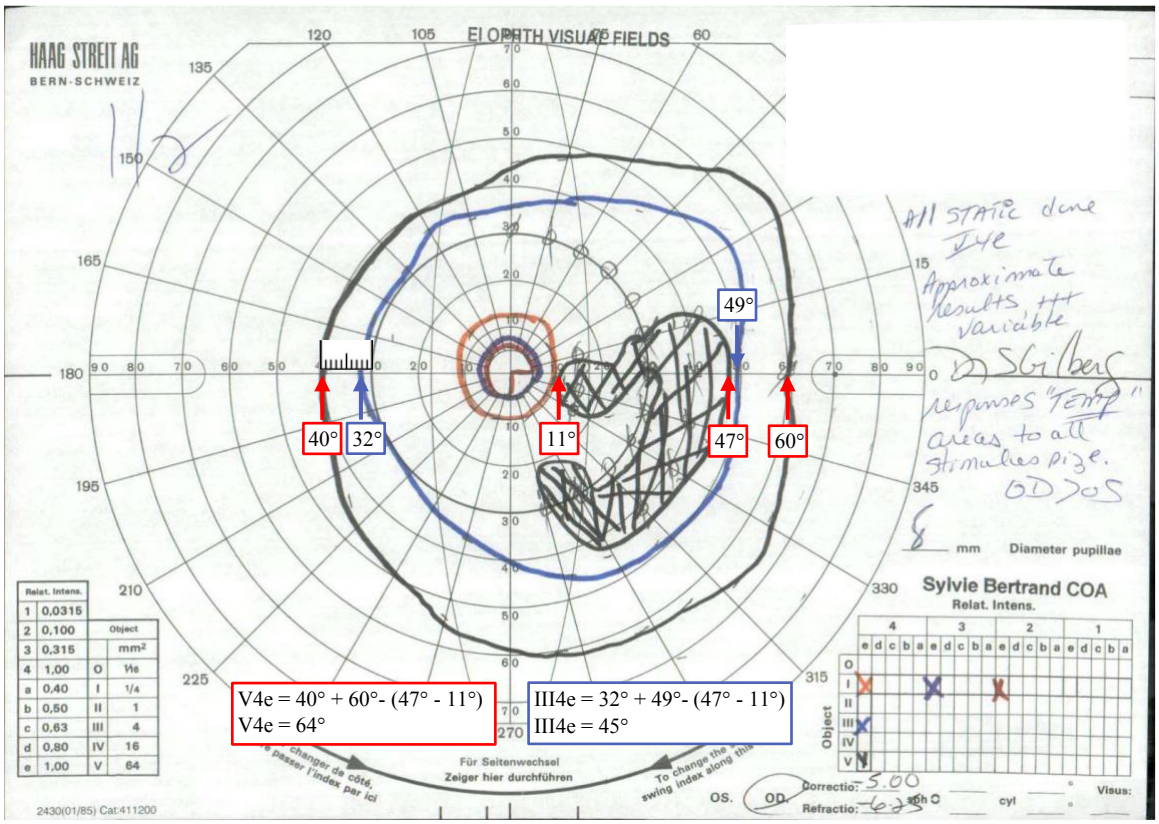

Figure 2.2. Goldman visual field isopter measurement. The patient's subjective limits of vision are represented as a cartographic chart where the centre indicates the position of the macula, and the numerical labels indicates distance from the macula in degrees. For this patient's right eye (OD – oculus dexter), the V4e stimulus size (black) is first seen 40° nasally and 60° temporally, for a total of 100°. There is a scotoma between 11° and 47° temporally, 36° in length. Subtracting this scotoma from the overall length gives 64° of functional vision in this longitude. It is important to note that as the V4e target is larger/more visible than the III4e target (blue), this scotoma will have to be subtracted from the III4e length as well. Therefore, the III4e stimulus has an overall length of 45°. Image obtained from study data.

2.4.3 Optical Coherence Tomography

SD-OCT images were acquired by a trained technician using a single device: Spectralis HRA + OCT (Heidelberg Engineering, Dossenheim, Germany) using an 870 nm light source, and entered into the clinical record. Full thickness 3D macular scans were captured using a 30° x 25° volumetric protocol of 8x8 mm^2 grid oriented on the foveal-Bruch's membrane opening (BMO) axis. The volume consisted of 19 transverse B-scan slices, each containing 512 sagittal A-scans. The SD-OCT images of all included patients

were imported into the OCT manufacturer's software (HEYEX Heidelberg Eye Explorer, version 1.9.10.0; Heidelberg Engineering).

For this study, the centremost B-scan through the fovea was selected for every eye. The brightness and contrast were adjusted within the software as needed to reduce signal noise and achieve the highest visual distinction between the preserved ellipsoid zone (EZ) and the surrounding area. The resulting adjusted b-scan and en-face view was exported as a .jpg file to a secure hospital SharePoint folder and de-identified.

Two iJCAPHO (International Joint Commission on Allied Health Personnel in Ophthalmology) certified OCT graders (L.K and M.E.) independently measured ellipsoid zone length by manually delineating the preserved EZ using the "segmented line" tool in ImageJ software (version 1.53m, Wayne Rasband, National Institutes of Health, Bethesda, MD, USA, http://imagej.nih.gov/ij) (Figure 2.3). The "Segmented Line' tool was chosen due to the non-linearity of the EZ band, which was defined as the second hyperreflective layer beginning from the RPE. EZ limit was considered where the hyperreflective band was no longer visible. For the purpose of the study horizontal scans were analysed: limits were nasal and temporal to the fovea. Scale was set in ImageJ using the 200 μm scale bar at the bottom-left corner of the B-scan and was re-calibrated for each scanned image (expected to be 33±2 μm per pixel). Once the ellipsoid zone had been traced, ImageJ's "Measure" function outputs a quantitative length analysis in μm. The comprehensive step-by-step ImageJ protocol is found in Appendix A.

As the true ellipsoid zone area can only be quantified if the full extent of the ellipsoid zone falls within the scanning window, if the EZ was observed to extend to the nasal or temporal border of the B-scan, the scan was excluded (Figure 2.4a). Exclusion criteria also included scans with significant central macular oedema (CME), macular hole, or any secondary conditions which caused total ellipsoid line breaks or rendered the EZ

indiscernible for measurement (Figure 2.4b,c). Scans with artefacts (such as due to cataracts, low image quality or insufficient brightness) causing the EZ to briefly disappear at the centre were included (Figure 2.4d,e). In instances where a patient had more than one macular OCT taken within the same month, the higher quality scan was chosen.

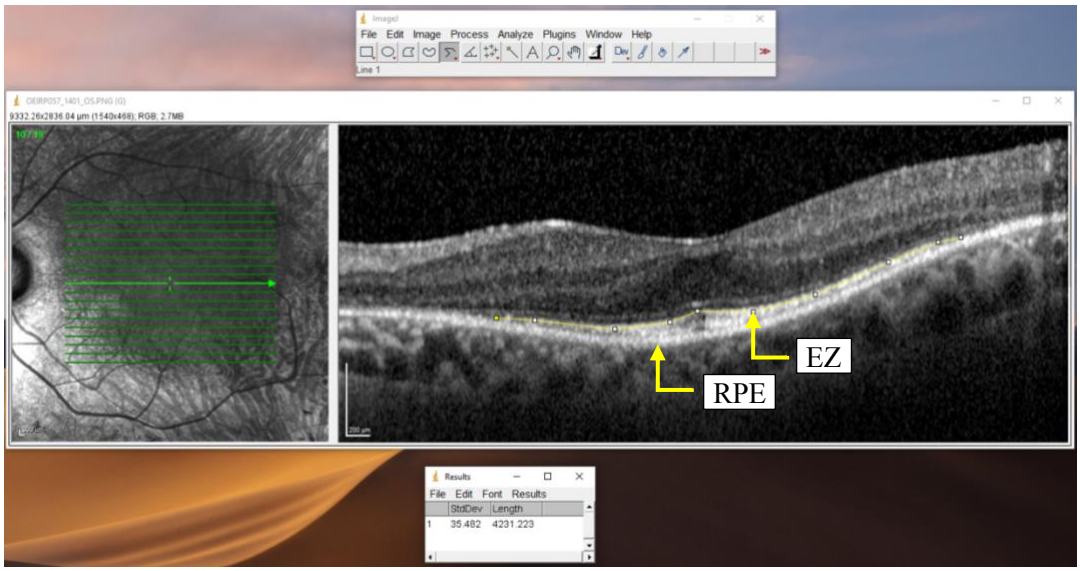

Figure 2.3. Ellipsoid zone measurement using ImageJ. The SD-OCT scan is composed of the enface fundus image (left) and the traverse foveal B-scan (right). The ellipsoid zone is the 2nd inner retinal hyperreflective band above the RPE. EZ limit was considered where the hyperreflective band was completely undetectable. The length scale was set using the 200 µm reference scale at the bottom left of the B-scan. Using the segmented line tool in ImageJ, the EZ is continuously traced from its first appearance to its complete disappearance, ensuring contours are followed with the use of callipers. ImageJ then outputs a measurement, which is 4231.22 for this scan. Image obtained from study data.

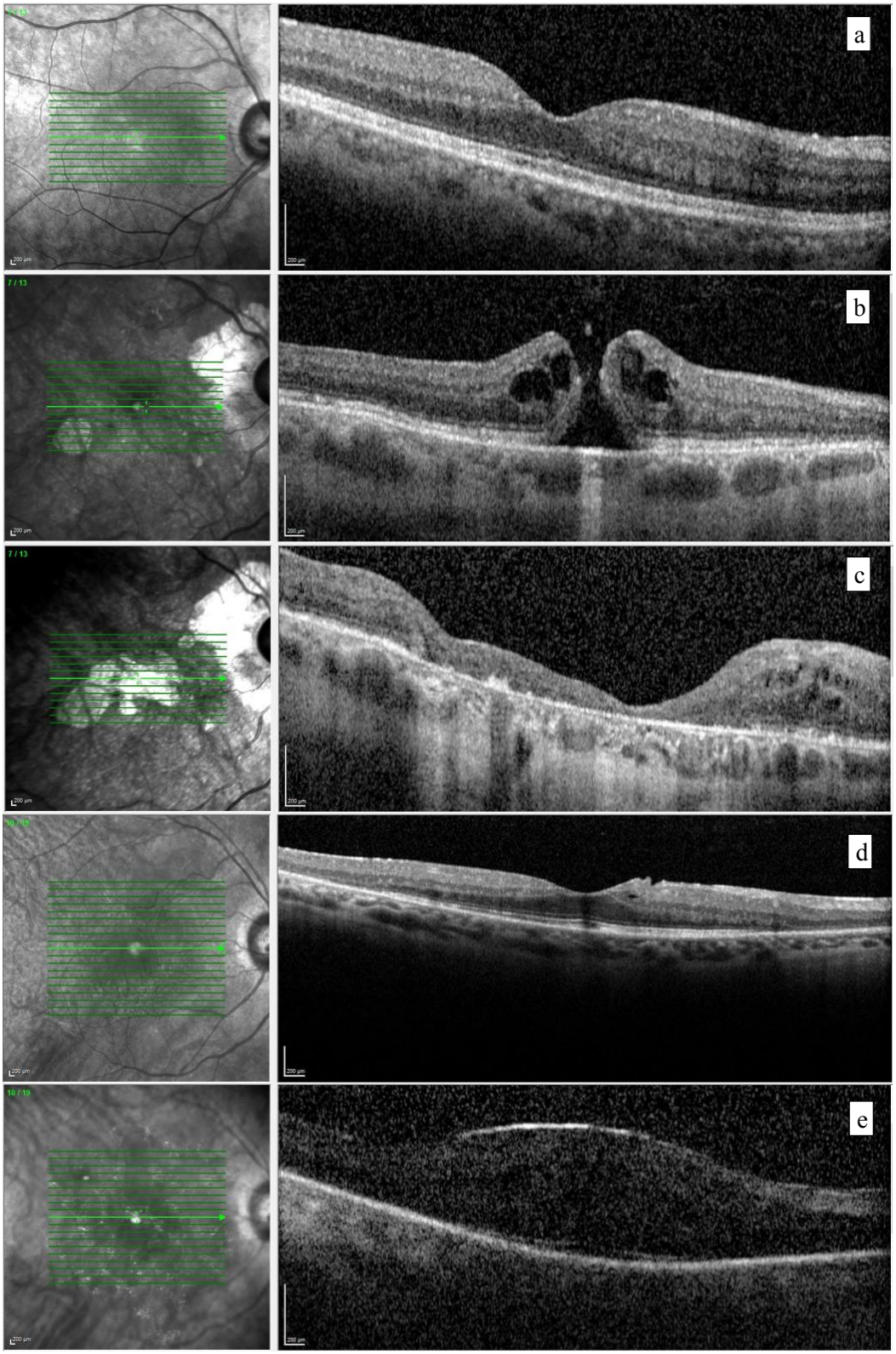

Figure 2.4. Various OCT presentations within study cohort. (a) A "full-length" EZ line, which extends beyond both the temporal and nasal limits of the OCT scan raster. (b) Macular hole causing a complete break of the full thickness of the retina. (c) Complex case of retinal dystrophy with loss of clarity of the retinal layers. (d) Central artefact seen in the full thickness of the retina. (e) CME and low image quality; adjustments to denoise the image allowed faint but sufficient visualization of the ellipsoid zone. 200 µm scale is visible on the bottom-left corner of both the en-face and OCT raster image. Images obtained from study data.

2.4.4 Fundus Autofluorescence

Fundus autofluorescence (FAF) images were acquired by a trained technician on dilated patients using either the TRC NW100 fundus camera (Topcon, Tokyo, Japan) or with Spectralis HRA + OCT (Heidelberg Engineering, Heidelberg, Germany) at a resolution of 1536 × 1536 pixels and a field of view of 30 degrees. A 521 nm barrier filter was used to filter emitted light after excitation with a wavelength of 486 nm. The images of all included patients were imported either into Synergy imaging records (Synergy Medical Inc., Lake St. Louis, USA) or the OCT manufacturer's software (HEYEX Heidelberg Eye Explorer, version 1.9.10.0; Heidelberg Engineering), then de-identified and exported to a secure hospital SharePoint folder for analysis.

2.5 Statistical Analysis

Distribution of all categorical and numerical data, both at baseline and at last visit was described using descriptive statistics. Deviation from normal values was calculated from the median due to the skewed nature of the dataset. Structural measurements, including EZ length and GVF isopter length were measured twice six months apart by the first author (L.K.) and another certified reader (M.E.), and the average was used for all analyses. Intergrader reproducibility was assessed by calculating the one-way intraclass correlation coefficient (ICC) where a higher ICC indicates better reproducibility of the variable. Bland-Altman plots were also generated to show the agreement between the graders by calculating the coefficient of repeatability, defined as the 95th percentile of the difference between both measurements. The rate of progression was calculated for each parameter by taking the difference between the value from the most recent visit and the value from the first visit, divided by the length of follow-up. Left and right eyes were compared by calculating the absolute difference between measurements for each diagnostic modality and using Pearson correlation to quantify the asymmetry.

To model the trajectories of each of the variables measured, linear mixed models (LMMs) were fit. LMMs are an extension of regular linear regression models that account for the correlation and heterogeneity in the data by including both fixed and random effects, which included:

- Fixed effects: relationship between independent variable (time) and dependent variable (structural measurement) similar to regular linear regression models
- Random effects: capture differences between groups or individuals not explained by the fixed effects. In this study involving multiple participants, random intercepts capture the variability in baseline measurements for each individual, while random slopes capture how the effect of predictors varies across individuals.

Regular linear regression treats all observations as independent, which can lead to incorrect standard errors and biased parameter estimates. LMMs are also flexible in handling unevenly spaced and unbalanced longitudinal data. They can accommodate missing data and different time intervals between measurements, which is a common challenge in disease progression studies. Thus, progression rates were estimated using a best fit LMM with an average intercept and slope.

The Pearson correlation coefficient was used to examine the relationship between all diagnostic modalities, and the average of the 2 measurements for each parameter was used for this analysis. Statistical analyses in this study were conducted using R programming (version 4.3.1; R Development Core Team) within the Jupyter Notebook environment (version 6.5.2; Project Jupyter). All data are presented as means ± SD.

Chapter 3 Results

3.1 Clinical Data

A total of 85 patients were diagnosed with retinitis pigmentosa (RP) between January 1st, 2011, and May 5th, 2021. Table 4 describes this cohort's demographics and outlines the diagnostic tests used to evaluate their clinical status. Forty-nine (57.65%) patients were female and thirty-six (42.65 %) were male. The average age of patients at the initial visit was 43.99 ± 16.53 (range 14.83–72.92) years. The average follow-up time was 1.02 ± 1.36 years (range 0.08–8.16 years), and the frequency of follow-up ranged from 1 to 29 visits, with the average patient returning to the OEI approximately 3.90 ± 4.35 times. Of the 85 patients, 54 did not have genetic testing results and 4 declined to be tested. Of the 27 who had genetic testing performed, 10 patients did not have any results uploaded in their electronic medical record (EMR), 3 were inconclusive, and 14 (16.47%) had a confirmed genetic causation. Four had ADRP (28.57%), eight (57.14%) had ARRP, one had XLRP, and one had mitochondrial RP (Figure 3.1).

Regarding diagnostic testing, 64 patients (75.29%) had at least one spectral-domain optical coherence tomography (SD-OCT) exam, 27 patients (31.76%) had at least one Humphrey automated visual field (HVF), 36 patients (42.35%) patients had at least one Goldmann visual field (GVF), 41 patients (48.24%) had at least one full-field electroretinogram (ffERG), 30 patients (35.29%) had at least one multi-focal electroretinogram (mfERG).

Additionally, 9 patients had an ocular ultrasound (10.59%), 11 patients had fluorescein angiography (FA) (12.94%), and 18 patients had fundus photography (21.18%). While the latter three diagnostic modalities are valuable tools for imaging the retina and assessing blood flow and vasculature, their appropriateness as measures of progression and efficacy in a clinical trial for retinitis pigmentosa is limited. They enable

big picture imaging of the entire globe and retina but are not sensitive enough to detect subtle changes in disease progression, and do not directly measure visual function or the patient's experience with the disease. Another common characteristic of these procedures is the invasiveness and associated risk, including close contact and pressure on the eye and great discomfort. In the case of FA, the use of a contrast dye may cause allergic reactions or complications at the injection site. In a clinical trial, the potential risks of this procedure may outweigh the benefits, even more so as a recurring procedure at efficacy checkpoints. Moreover, this procedure can only be carried out on one eye at a time, which would hinder efforts to assess the treated eye against the control eye for efficacy. For the described reasons, ocular ultrasound, fundus photography and FA were also excluded from the analysis.

Table 4. Demographics, metrics, and diagnostic summary of study cohort

Cohort total (n)	85		
Demographics	**n**	**%**	
Female (n)	49	57.65	
Male (n)	36	42.35	
Caucasian (n)	66	77.65	
Non-Caucasian (n)	19	22.35	
Patient Metrics	**Mean ± SD**	**Range**	
Age at first visit (y)	43.99 ± 16.53	14.83 – 71.92	
Age at last visit (y)	46.86 ± 16.23	16.42 – 72.33	
Interval between visits (y)	1.02 ± 1.36	0.08 – 8.16	
Number of visits (n)	3.90 ± 4.36	1 – 29	
Diagnostic tests	**patients (n)**	**%**	**with follow-up (n)**
Genetics	14	16.47	-
Optical Coherence Tomography (OCT)	64	75.29	44
Automated Visual Fields (Humphrey)	27	31.76	9
Manual Visual Fields (Goldmann)	36	42.35	11
Full-field Electroretinogram (ffERG)	41	48.24	8
Multi-focal Electroretinogram (mfERG)	30	35.29	3
Fundus Auto-fluorescence (FAF)	16	18.82	2
Ultrasound (b-scan)	9	10.59	1
Fluorescein Angiography (FA)	11	12.94	1
Fundus Photography	18	21.18	3

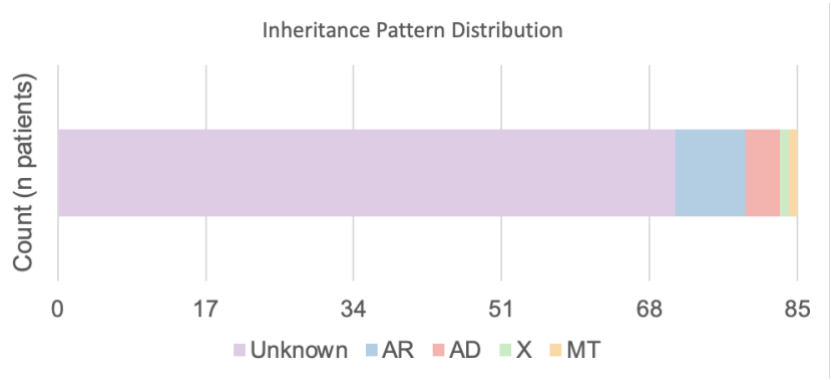

Figure 3.1. Genetic inheritance distribution of study cohort. While a substantial portion remains uncharacterised (83.53%), the cohort still reflects the heterogeneity of RP transmission modes. Of those with confirmed genetic causation, autosomal recessive (AR; 57.14%) and autosomal dominant (AD; 28.57%) are the most common, whereas X-linked (X) and mitochondrial (MT) are the least (7.14% each).

There were 16 (18.82%) patients who had at least one fundus autofluorescence (FAF) image, 11 (68.75%) of which had an OCT FAF and 5 (37.50%) had a fundus camera FAF. Of the two patients with repeat FAFs (3 FAFs each), one was solely examined using the fundus camera, while the other was solely examined via OCT. Unfortunately, the quality of images for a substantial proportion of the patients (9 individuals, or 56.25%) was notably suboptimal, including low exposure, high grain and signal noise, and the presence of other comorbidities (Supplemental Figure I). This left us with a dataset of 7 patients with FAF where the hyperautofluorescent ring (HAR) was sufficiently visible for measurement purposes, one of which had a repeat image. However, the FAF images from both OCT and fundus photography lacked a standardized scale to convert raw measurements. Due to the absence of a standardized measurement scale and the predominantly poor quality of FAF images within the study cohort, despite the promising potential of fundus autofluorescence for providing objective structural assessments closely correlated with changes in the ellipsoid zone, it was decided to exclude this dataset from the subsequent analysis.

Of the five diagnostic tests examined in this study (OCT, HVF, GVF, ffERG and mfERG), 71 patients (83.53%) had at least one of the diagnostic tests performed over the

course of their visits to the OEI, 51 patients (60.00%) had at least 2 of the diagnostic tests done, 38 patients (44.71%) had at least 3 of the diagnostic tests, 31 patients (36.47%) had at least 4 of the diagnostic tests, and 8 patients (9.41%) had all 5 diagnostic tests performed. The combinations of diagnostic testing are displayed in Table 5, which indicates that the most common diagnostic pair performed for patients with RP is an OCT and ffERG (40 out of 85; 47.06%). Fourteen patients (14 out of 85; 16.47%) did not have any diagnostic testing and were thus excluded from the statistical analysis. However, these patients were still included in the demographics portion, as they represent a potential cohort for future clinical trials or interventions. Their inclusion in the demographic data allows us to consider them in the broader context of our patient population and paves the way for future research endeavours aimed at addressing their specific healthcare needs.

Table 5. Intersections of diagnostic testing by number of patients

	OCT	HVF	GVF	ffERG	mfERG
OCT	64	23	33	40	28
HVF	23	27	13	20	14
GVF	33	13	36	29	22
ffERG	40	20	29	41	30
mfERG	28	14	22	30	30

3.2 Genetics

Table 6 summarises the full genetic characterisation of each patient with confirmatory results uploaded in their EMR, including genotypic variants, affected protein/function, and resulting phenotype. Among 8 patients with autosomal recessive RP, half presented with syndromic RP, including 3 with Usher's Syndrome (2 caused by mutations in CDH23 and 1 by a mutation in USH2A) and 1 with Bardet-Biedl Syndrome (with a mutation in TTC8). The other half included 2 patients with non-syndromic RP (caused by mutations in TULP1 and LRAT) and the remaining 2 did not have a genotype/phenotype reported. Among 4 patients with autosomal dominant RP, the affected genes were RP1, RHO, TOPORS, and CA4. Maternal inheritance accounted for 2 patients; 1 case of X-

linked RP caused by an RPGR mutation and 1 mitochondrial case resulting in Kearns-Sayre Syndrome (caused by a mutation in MT-TL1).

Table 6. Genotype, proteins, and their functions in study subjects with genetic results available

ID	Sex	Genotype	Protein	Function	Phenotype	Inheritance
OEI-RP-017	M	RP1 (c. 2029C>T p.Arg677*)	RP-1 protein	Tissue development and maintenance	RP 1	Autosomal dominant
OEI-RP-022	M	RHO (c.638C>T p.Pro180Ser)	Rhodopsin	Phototransduction	RP 4	Autosomal dominant
OEI-RP-026	F	TOPORS (n/a)	Topoisomerase I binding, arginine/serine-rich	Localized in the basal body of connecting cilia in photoreceptors	RP 31	Autosomal dominant
OEI-RP-027	F	n/a	n/a	n/a	n/a	Autosomal recessive
OEI-RP-029	M	TULP1 (c.373G>T p.Glu125* and c.191-7G-T)	Tubby-like protein 1	Tissue development and maintenance	Leber Congenital Amaurosis 15 and RP 14	Autosomal recessive
OEI-RP-036	F	MT-TL1 (m.3265T>C)	tRNA leucine 1 (UUA/G)	Protein assembly	Kearns-Sayre Syndrome	Mitochondrial
OEI-RP-042	F	CA4	Carbonic Anhydrase IV	Zn-containing enzyme that catalyses hydration of carbon dioxide	RP 17	Autosomal dominant
OEI-RP-045	F	CDH23 (c.6050-9G>A)	Cadherin 23	Inner ear tip link formation and retinal periciliary maintenance	USH1D	Autosomal recessive
OEI-RP-050	M	CDH23 (c.3844_3847dupAATG p.Val1283Glufs*6 and c.7823G>A p.Arg2608His)	Cadherin 23	Inner ear tip link formation and retinal periciliary maintenance	USH1D	Autosomal recessive
OEI-RP-059	M	TTC8 (c.380C>A p.Thr127Lys)	Tetratricopeptide repeat domain 8	Cellular structure	RP 51 and Bardet-Biedl Syndrome 8	Autosomal recessive
OEI-RP-063	F	USH2A: (c2276G>T and c.2299del)	Usherin	Inner ear ankle links formation and cochlear development and retinal periciliary maintenance	USH2A	Autosomal recessive
OEI-RP-071	F	n/a	n/a	n/a	n/a	Autosomal recessive
OEI-RP-073	M	LRAT (c.12del:p.Met5Cysfs*54)	Lecithin retinol acyltransferase	Retinal metabolism	Leber Congenital Amaurosis 14 and RP	Autosomal recessive
OEI-RP-084	M	RPGR (c.2405_2406del p.Glu802Glyfs*32)	Retinitis pigmentosa GTPase regulator	Intraflagellar transport	RP 3	X-linked

3.3 Current Status, Distribution, and Symmetry of Study Cohort

Figures 3.2 through 3.15 reveal a comprehensive assessment of the RP cohort seen at the Ottawa Eye Institute based on each patient's most recent diagnostic assessment, through a diverse range of diagnostic modalities. This reveals valuable descriptive statistics on the current disease severity level, which is critical for identifying the eligible candidates for a future clinical trial. To visualise the distribution of RP data from the expected range of a healthy patient, data points were plotted with normal range of each diagnostic outcome. Exceptionally, the ellipsoid zone does not have normal range due to the limited range of view of the OCT, so the OCT raster boundaries was used instead. For electroretinography, the normal value ± 2 SDs was used, keeping in line with clinical practice. Normative data was provided by Diagnosys LLC (Appendix B and C).

The OCT images were used to measure the length of the ellipsoid zone for each patient. Ellipsoid zone measurements were taken from the central-most b-scan of the OCT. The majority of patients have an ellipsoid zone length between 1500 and 2500 μm (Figure 3.2), translating to approximately 15 – 25° of the central retina (based on average OCT raster horizontal length of 6000 μm/60° = 100 μm per 1°). Due to the limitations of OCT technology, the true extent of the ellipsoid zone may be obscured, making it challenging to discern whether it terminates just outside the captured OCT borders or extends further into the peripheral retina. Measurements where the ellipsoid zone limits are the limits of the OCT raster (Figure 3.2 grey box) were excluded from subsequent analysis. The EZ lengths are shown to be highly symmetrical between eyes, with a correlation of 0.981 ($p<0.001$) (Figure 3.3).

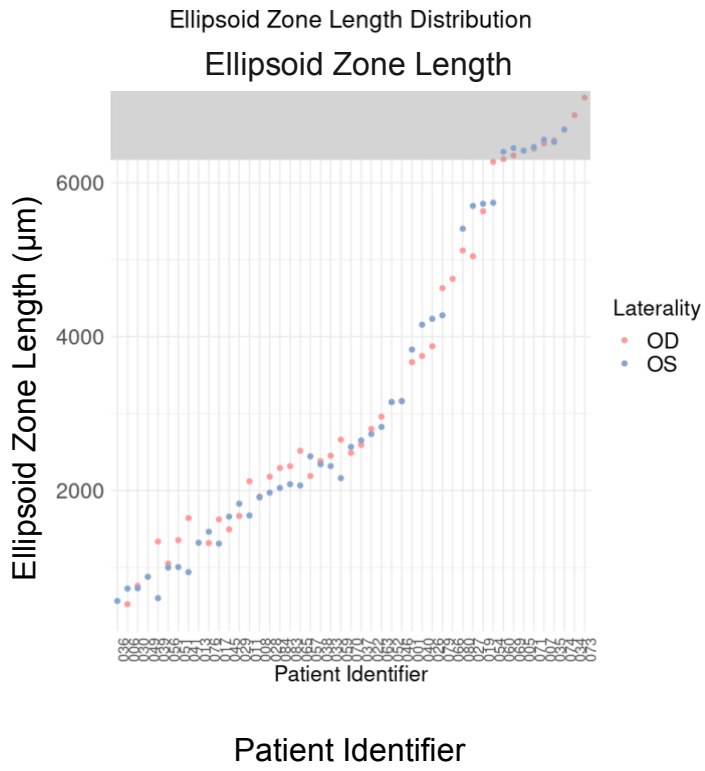

Figure 3.2. Distribution of ellipsoid zone lengths. Scatterplot reflecting the most recent status of the ellipsoid zone for all patients with an OCT, from each patient's most recent EZ length measurement. The vertical grey bar demarcates the limits of the OCT raster. If a patient's EZ length falls within this grey bar, the true length is unknown, and the patient is likely still in the early stages of the disease. For both eyes, here is significant concentration of ellipsoid zone lengths between 1500 and 2500 µm. Laterality: OD (oculus dexter, right eye) and OS (oculus sinister, left eye). µm=micrometres.

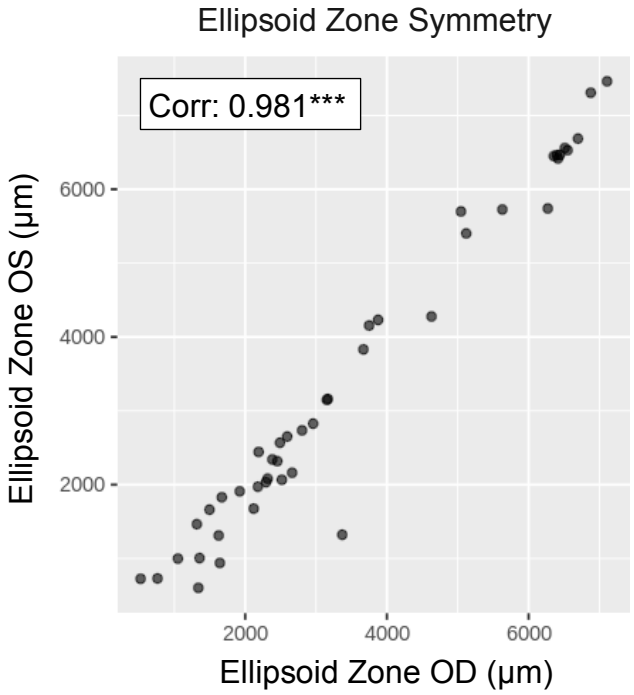

Figure 3.3. Correlation of ellipsoid zone length between eye pairs for patients with data for both eyes. The scatter plot represents each patient's measurement pair as a single point with the Pearson's correlation coefficient and degree of significance. The EZ lengths are highly symmetrical between eyes, with r=0.981 ($p<0.001$).

The Humphrey visual field measures mean deviation (MD), which refers to the difference of light sensitivity between the tested eye and that of a person with normal vision from the same age group. MD is measured for each of 3 different sized fields: 30-2 (central 30°), 24-2 (central 24°) and 10-2 (central 10°). MD is overall uniformly distributed (Figure 3.4) but as the field of view tested decreases from 30° to 10°, a skew to increasingly negative values is observed (Figure 3.4 B). MD measurements are symmetrical between eyes with a correlation of 0.947 ($p<0.001$; Figure 3.5).

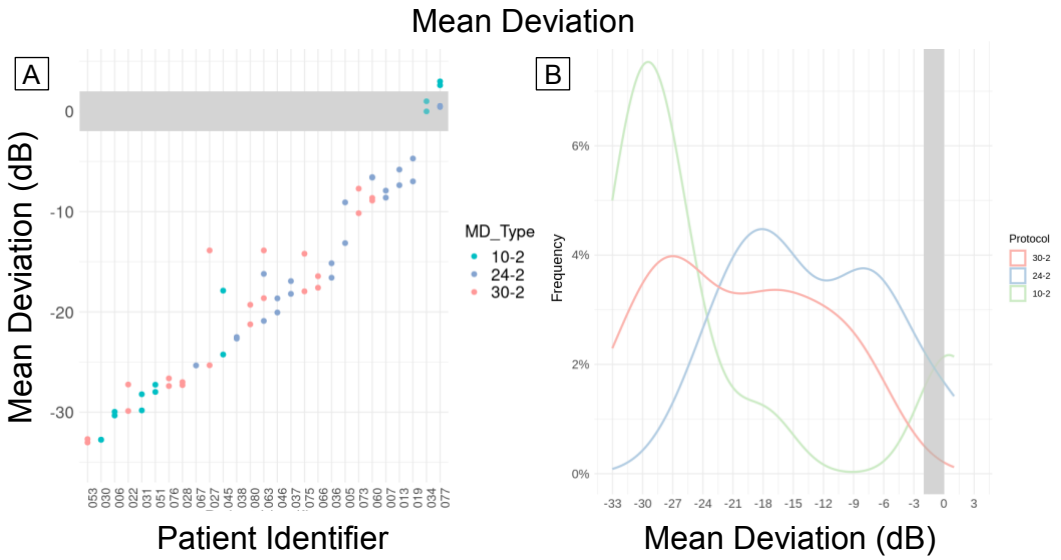

Figure 3.4. Distribution of mean deviations across various testing protocols. (A) Scatterplot reflecting the most recent status of the central visual field for all patients with an automated visual field, based on each patient's most recent mean deviation value. For 27 patients with a HVF, 11 underwent 30-2, 12 underwent 24-2, and 7 underwent a 10-2 testing protocol. (B) Density plot of mean deviation for the 3 HFA protocols. The vertical grey bar indicates the normal range for all testing protocols, which is 0 ± 2. Patients whose MD is within this range have preserved function in their central 30°. Except for 2 patients, all patients' mean deviation fall below the normal range.

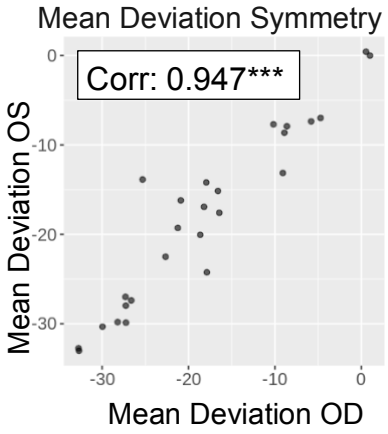

Figure 3.5. Correlation of mean deviation between eye pairs. The correlation of mean deviation across all testing protocols between OD and OS for patients with data for both eyes. The scatter plot represents each patient's mean deviation pair as a single point with the Pearson's correlation coefficient and degree of significance. The mean deviation is highly symmetrical between eyes, $r=0.947$ ($p<0.001$). dB=decibels.

The Goldmann visual field measures the size of the visual field using stimuli of different sizes and intensities, from largest and most intense to smallest and least intense in the following order: V4e, III4e, I4e, I3e, I2e. Here, isopter lengths decrease as one moves from V4e to I2e, with all isopters distributed significantly below their normal ranges (Figure 3.6). Peak isopter length is 75 degrees for V4e, 27 degrees for III4e, 15 degrees for I4e, 10 degrees for I3e, and 6 degrees for I2e. Isopter lengths are shown to be highly symmetrical between eyes, with a correlation of 0.905 ($p<0.001$; Figure 3.7).

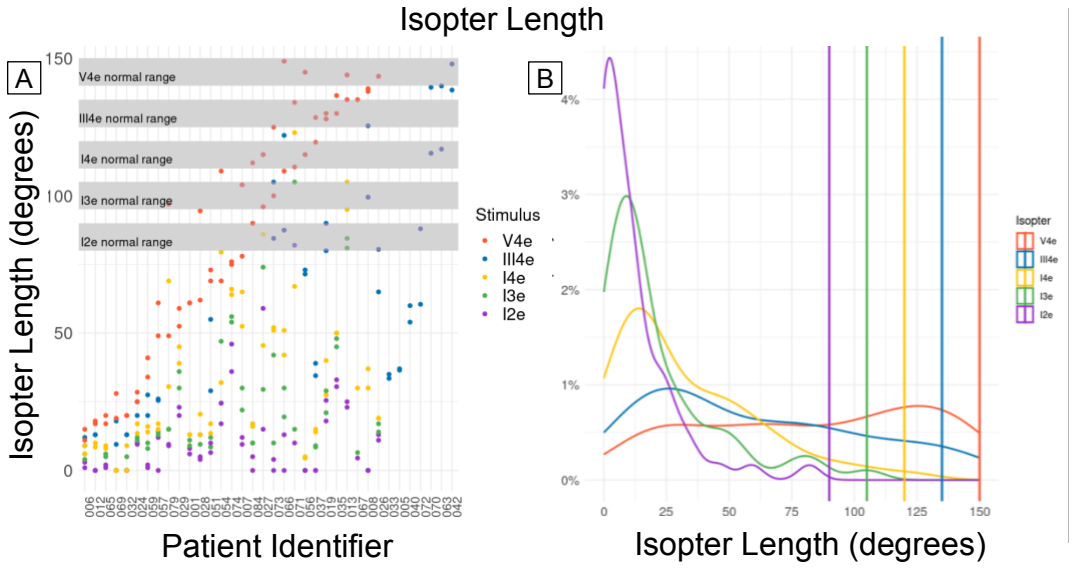

Figure 3.6. Distribution of isopter lengths across five stimulus sizes. (A) Scatterplot reflecting the most recent status of the full visual field for all patients with a manual visual field. The vertical grey bar indicates the normal range for each isopter. The majority of data points fall under the normal range for each stimulus size. (B) Density plot of isopter length values, which reveals a pattern of progressive loss of sensitivity prior to total loss of function. The x-intercepts represent the normal value per isopter.

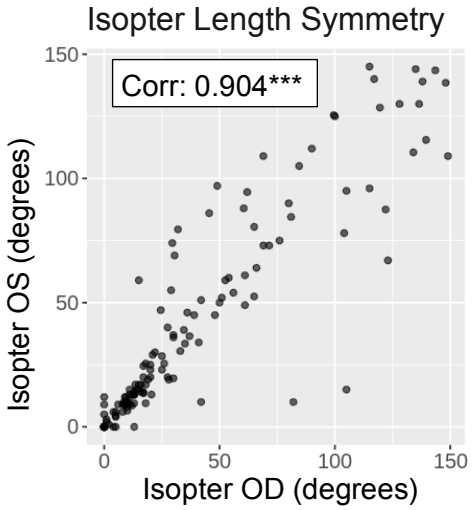

Figure 3.7. Correlation of isopter lengths between eye pairs. The correlation of isopter lengths across all stimuli between OD and OS for patients with data for both eyes. The scatter plot represents each patient's isopter length pair as a single point with the Pearson's correlation coefficient and degree of significance. Isopter lengths are shown to be highly symmetrical between eyes, with a correlation of 0.904 ($p<0.001$). Isopter lengths are also highly concentrated in the bottom-left corner, indicating a severely diminished field.

Multi-focal ERG measures the electrical responses of 5 rings within 30° to assess localized retinal function. Most of the patients have N1 and P1 latencies that are in the normal range for all rings (Figure 3.8A, B), although some show increased latencies for some of the rings, indicating a shift towards a delayed mfERG response. Amplitudes for a significant proportion of the rings is lower in most patients and are mostly distributed between 0 and 10 nv/deg^2, indicating diminished photoreceptor function, particularly for rings 3-5 (Figure 3.8C). Values for amplitude and latency were very similar between eyes with correlation coefficients of 0.948 to 0.992 ($p<0.001$ for all; Figure 3.9).

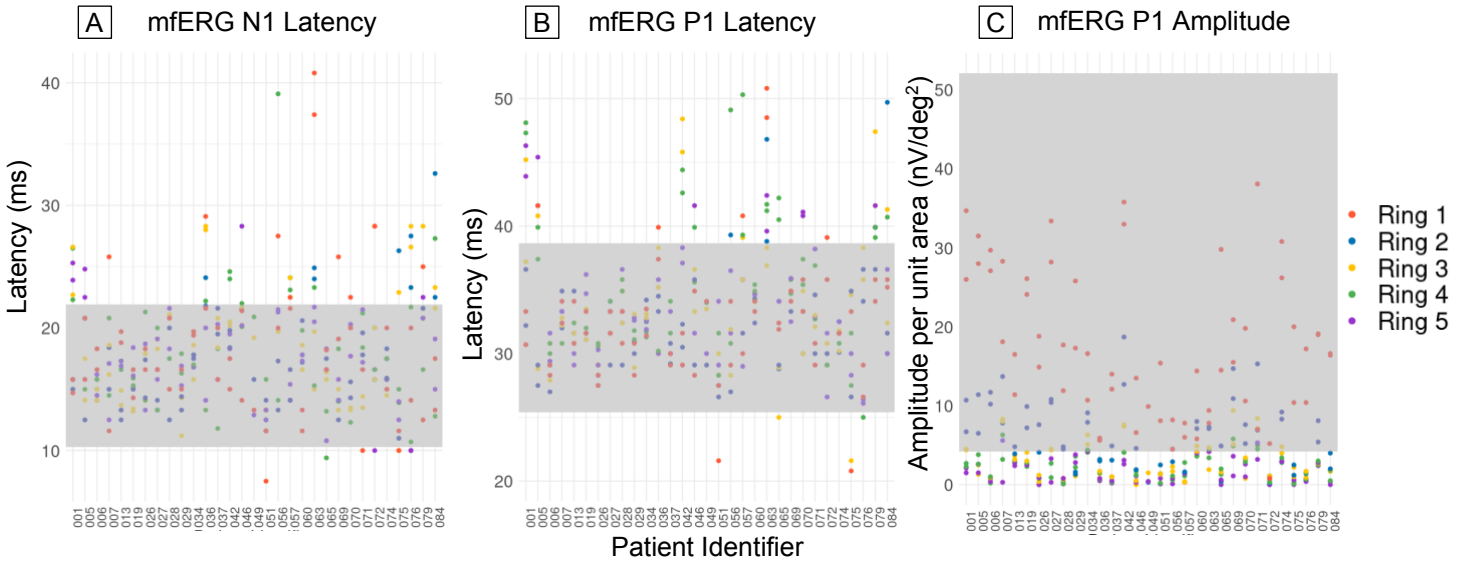

Figure 3.8. Distribution of multifocal ERG responses across five rings. Scatterplot reflecting the most recent status of the N1 latency (A), P1 latency (B), and P1 amplitude (C) for all patients with a mfERG, based on each patient's most recent mfERG. The vertical grey bar indicates the normal range ± 2 SD for latency across all rings and for each ring amplitude. Although the distribution of latency is varied, a portion of patients exhibit delayed mfERG responses. Amplitude is mostly distributed between 0 and 10 nv/deg^2, indicating diminished photoreceptor function, particularly for rings 3-5. µV = microvolts. ms = millisecond. nV/deg^2 = nanovolts per degree area (amplitude per unit area).

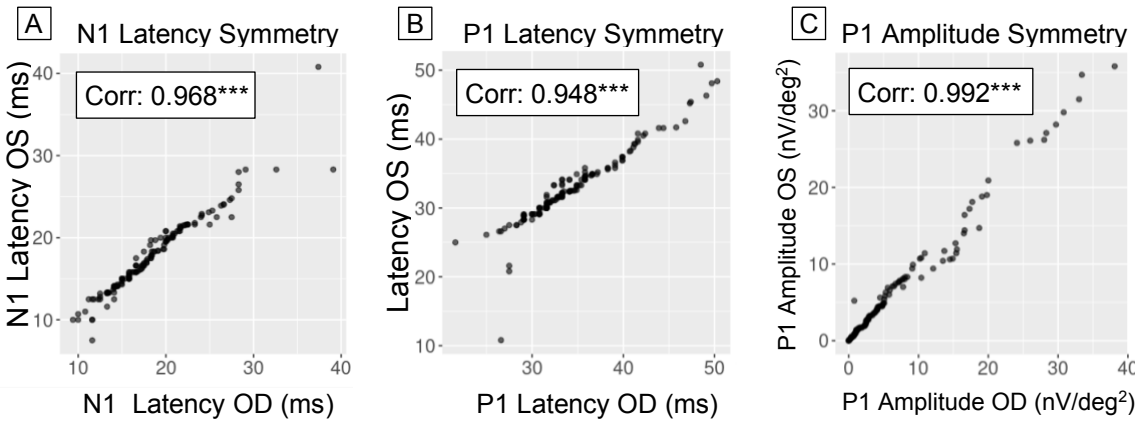

Figure 3.9. Correlation of mfERG responses between eye pairs. The correlation of N1 latency, P1 latency, and P1 amplitude between OD and OS across all five rings for patients with data for both eyes. Each scatter plot represents each patient's mfERG response pair as a single point with the Pearson's correlation coefficient and degree of significance. (A) N1 latency is shown to be highly symmetrical between eyes, with a correlation of 0.968 ($p<0.001$). (B) P1 latency is shown to be highly symmetrical between eyes, with a correlation of 0.948 ($p<0.001$). (C) P1 amplitude is shown to be nearly perfectly symmetrical between eyes, with a correlation of 0.992 ($p<0.001$). ms = millisecond. nV/deg^2 = nanovolts per degree area (amplitude per unit area).

Full-field electroretinography (ffERG) measures the overall electrical responses of the entire retina, providing a global assessment of retinal function under light and dark conditions. For the photopic condition, a- and b-wave latencies in RP patients were often in the normal range with a slight tendency toward longer than normal response times (Figure 3.10A) whereas a- and b-wave amplitudes were found mostly outside the normal range (Figure 3.10B), indicating diminished photoreceptor function. Values were highly asymmetric between eyes for a-wave latency with a correlation of 0.023 ($p>0.05$) and moderately symmetrical for b-wave latency with a correlation of 0.591 ($p<0.001$) (Figure 3.11A), and for a- and b-wave amplitude with correlations of 0.663 and 0.816 ($p<0.001$ for all; Figure 3.11B, C, D). For the 30Hz flicker test, the majority of peak and trough latency values, although highly varied, fell within acceptable normal ranges (Figure 3.12B). 30Hz flicker peak amplitudes were mostly lower than normal values (Figure 3.12A). Values for amplitude and latency were moderately similar between eyes with correlation coefficients of 0.528 to 0.771 ($p<0.001$ for all; Figure 3.13).

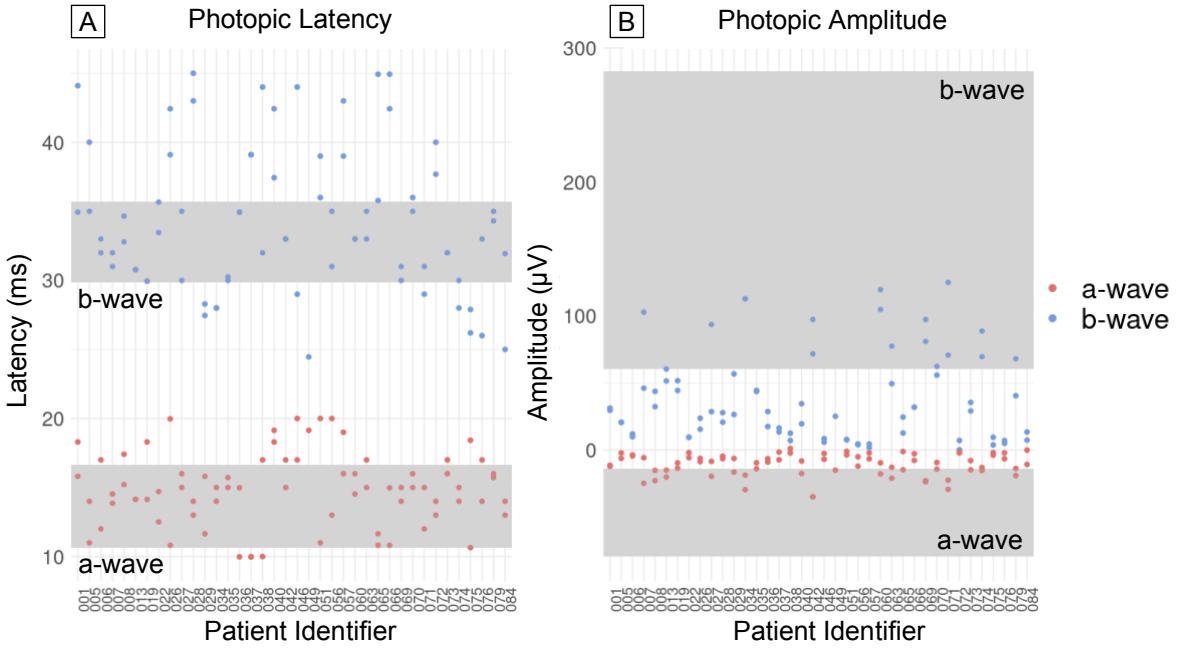

Figure 3.10. Distribution of photopic ffERG responses. Scatterplot reflecting the most recent status of the a-wave and b-wave latency (A), and a-wave and b-wave amplitude (B) for all patients with a ffERG, based on each patient's most recent ffERG. The vertical grey bar indicates the normal range + 2 SD of a-wave and b-wave for each response. While a-wave and b-wave latency was mostly in the normal range for RP patients, the majority of a-wave and b-wave amplitude values were distributed outside of the normal range. µV = microvolts. ms = millisecond.

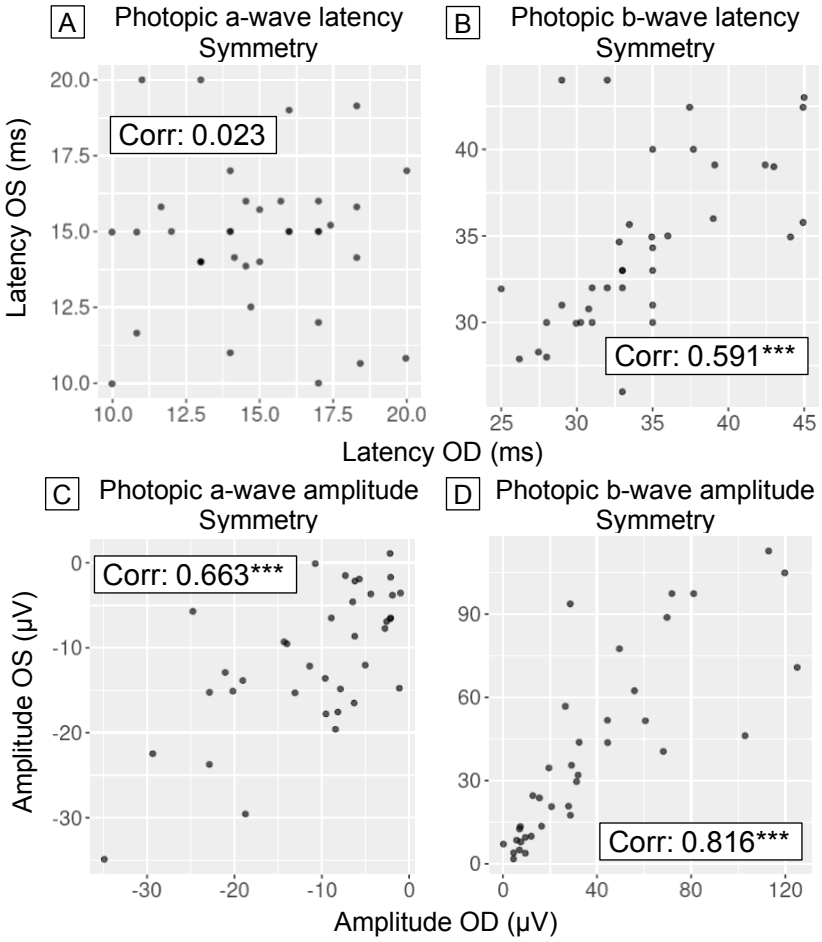

Figure 3.11. Correlation of photopic ERG responses between eye pairs. The correlation of a- (A) and b-wave (B) latency, and a- (C) and b-wave (D) amplitude between OD and OS for patients with data for both eyes. Each scatter plot represents each patient's response pair as a single point. (A) a-wave latency is not symmetrical between eyes, r=0.023 (p>0.05). (B) b-wave latency is moderately symmetrical between eyes, r=0.591 (p<0.001) (C) a-wave amplitude is moderately symmetrical between eyes, r=0.663 (p<0.001) (D) b-wave amplitude is moderately symmetrical between eyes, r=0.771 (p<0.001). ms = millisecond. µV = microvolts.

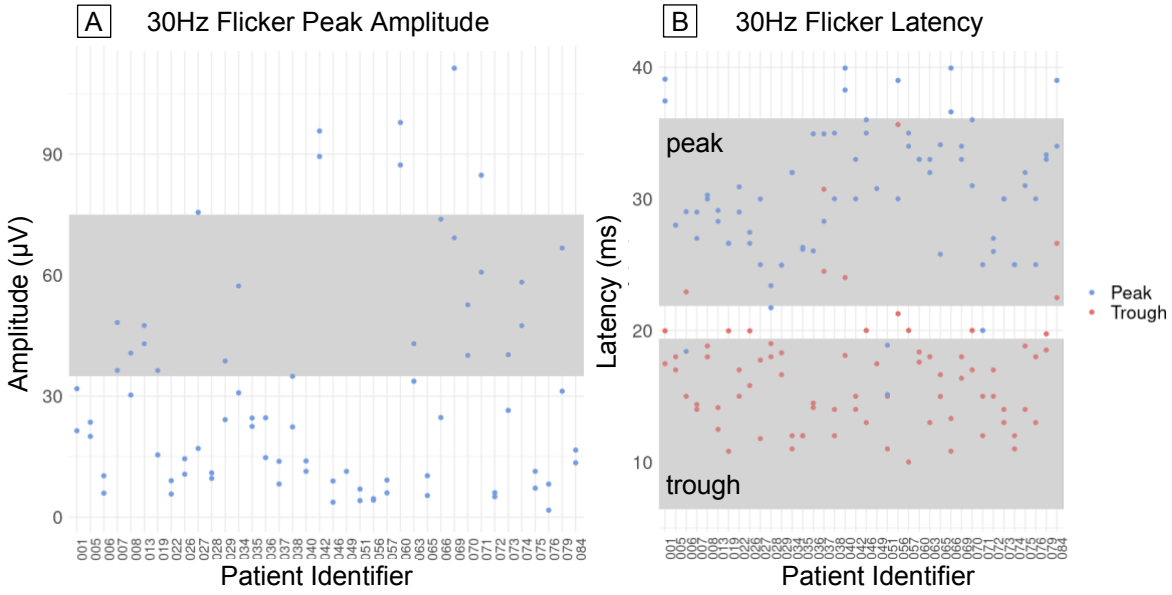

Figure 3.12. Distribution of photopic 30Hz flicker responses. Scatterplot reflecting the most recent status of the 30Hz flicker peak amplitude (A) as well as peak and trough latency (B) for all patients with a ffERG, based on each patient's most recent ffERG. The vertical grey bar indicates the normal range + 2 SD for each response. While peak and trough latency did not appear to be significantly distributed outside the expected normal range, the majority of amplitude values were distributed underneath the normal range. µV = microvolts. ms = millisecond.

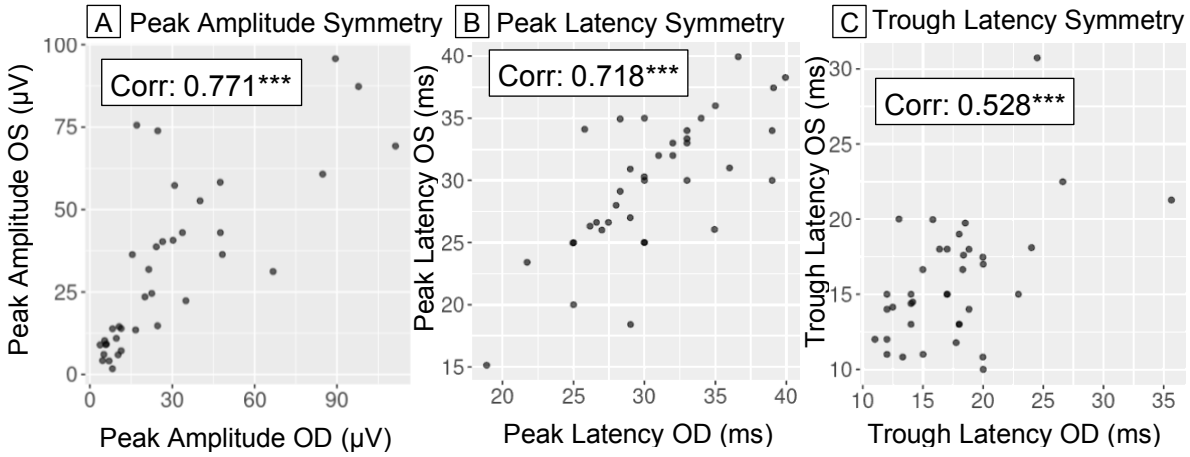

Figure 3.13. Correlation of 30Hz Flicker ERG responses between eye pairs. The correlation of 30Hz flicker peak amplitude (A), and peak (B) and trough (C) latency between OD and OS for patients with data for both eyes. Each scatter plot represents each patient's 30Hz flicker response pair as a single point with the Pearson's correlation coefficient and degree of significance. (A) Peak amplitude is highly symmetrical between eyes, r=0.904 (p<0.001). (B) Peak latency is highly symmetrical between eyes, r=0.921 (p<0.001). (C) Trough latency is moderately symmetrical between eyes, r=0.528 (p<0.001). µV = microvolts. ms = millisecond.

Lastly, for the scotopic condition, a- and b-wave amplitudes across the three constant luminance intensities (0.01, 3.0, and 10.0 cd·s/m^2) were found to be consistently lower than normal values (between 0 ± 100 μV), whereas a- and b-wave latencies for all intensities were relatively unimpacted (Figure 3.14). Values for amplitude showed moderate asymmetry between eyes for the a-wave 0.01 cd·s/m^2 with a correlation of 0.275 ($p>0.05$), moderate symmetry for a-wave 3.0 and 10.0 cd·s/m^2 with correlation coefficients of 0.729 ($p<0.001$) and 0.757 ($p<0.001$) respectively (Figure 3.15A), and high symmetry for b-wave 0.01, 3.0 and 10.0 cd·s/m^2 with correlation coefficients of 0.811 ($p<0.001$), 0.907 ($p<0.001$) and 0.904 ($p<0.001$), respectively (Figure 3.15B). Values for latency showed moderate asymmetry between eyes for the a-wave 0.01, 3.0 and 10.0 cd·s/m^2 with correlations of 0.275 ($p<0.01$), 0.318 ($p>0.05$), and 0.285 ($p>0.05$) respectively (Figure 3.15C), and moderate symmetry for b-wave 0.01, 3.0 and 10.0 cd·s/m^2 with correlation coefficients of 0.637 ($p<0.001$), 0.711 ($p<0.001$) and 0.600 ($p<0.001$), respectively ($p<0.001$ for all; Figure 3.15B).

Due to an overwhelming number of diagnostic variables for mfERG and ffERG, this analysis provided a means to evaluate which responses are most deviated from normal. As latency was observed to show high variability and low symmetry of values, it was decided that the amplitude responses of all testing strategies would form the basis of subsequent analysis.

Overall, the majority of the OEI RP population is in moderate-advanced stages of RP. Given the strong correlation between both eyes for most outcomes, we can assume that changes in one eye are highly predictive of changes in the other. Furthermore, clinicians typically assess RP patients based on both eyes together. As such, the left and right eye were averaged to provide a more robust estimate of overall disease progression.

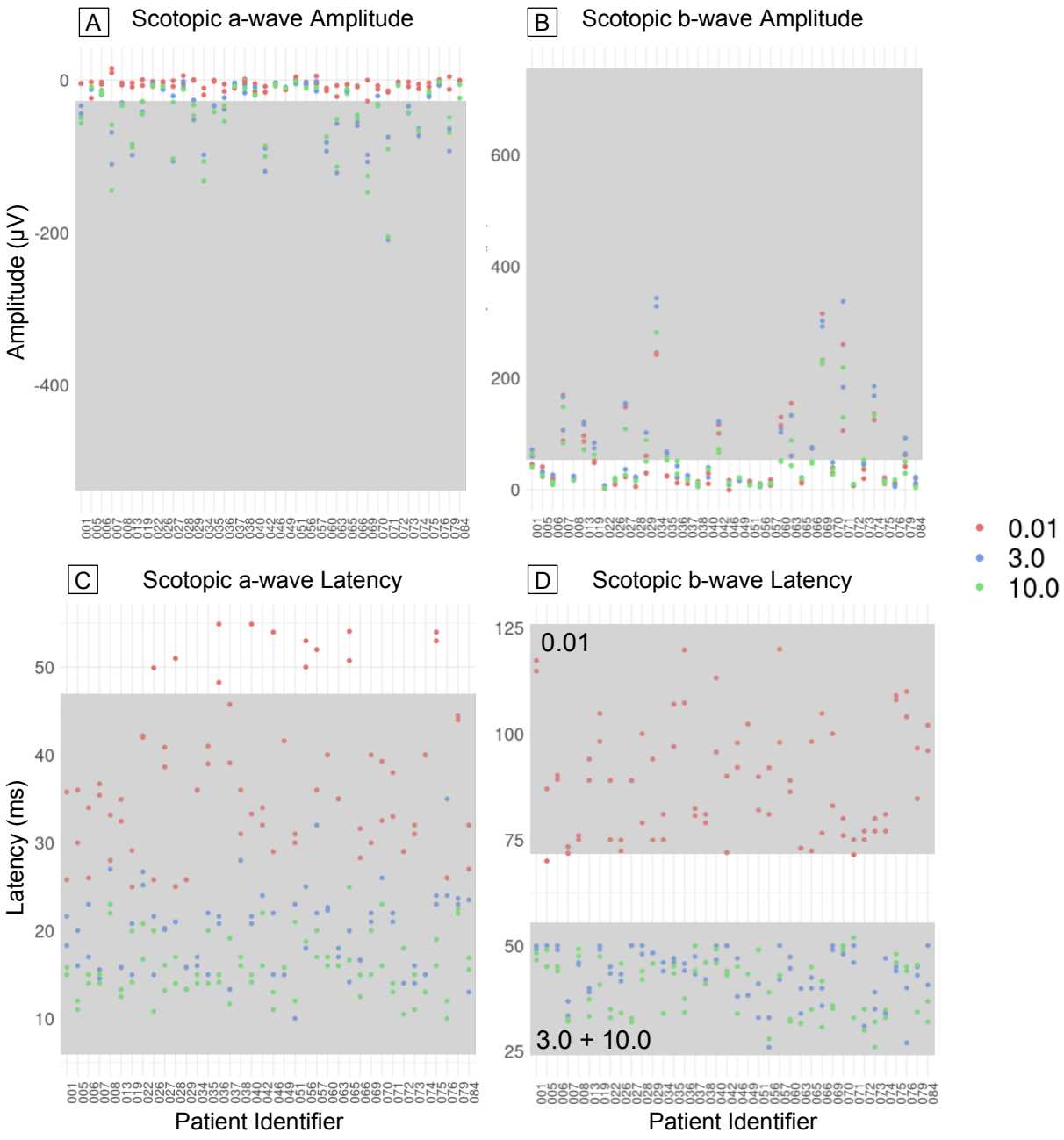

Figure 3.14. Distribution of full-field ERG scotopic responses. Scatterplot reflecting the most recent status of the scotopic a-wave (A) and b-wave (B) amplitudes as well as the a-wave (C) and b-wave (D) latencies for all patients with a ffERG, based on each patient's most recent ffERG. The vertical grey bar indicates the normal range + 2 SD for each response. Amplitude was severely diminished, particularly for the 0.01 cd·s/m^2 stimulus intensity. Latency, for all stimulus intensities, is in the normal range. µV = microvolts. ms = millisecond. Luminance = 0.01, 3.0, and 10.0; cd·s/m^2 = candela second per square meter (constant luminance).

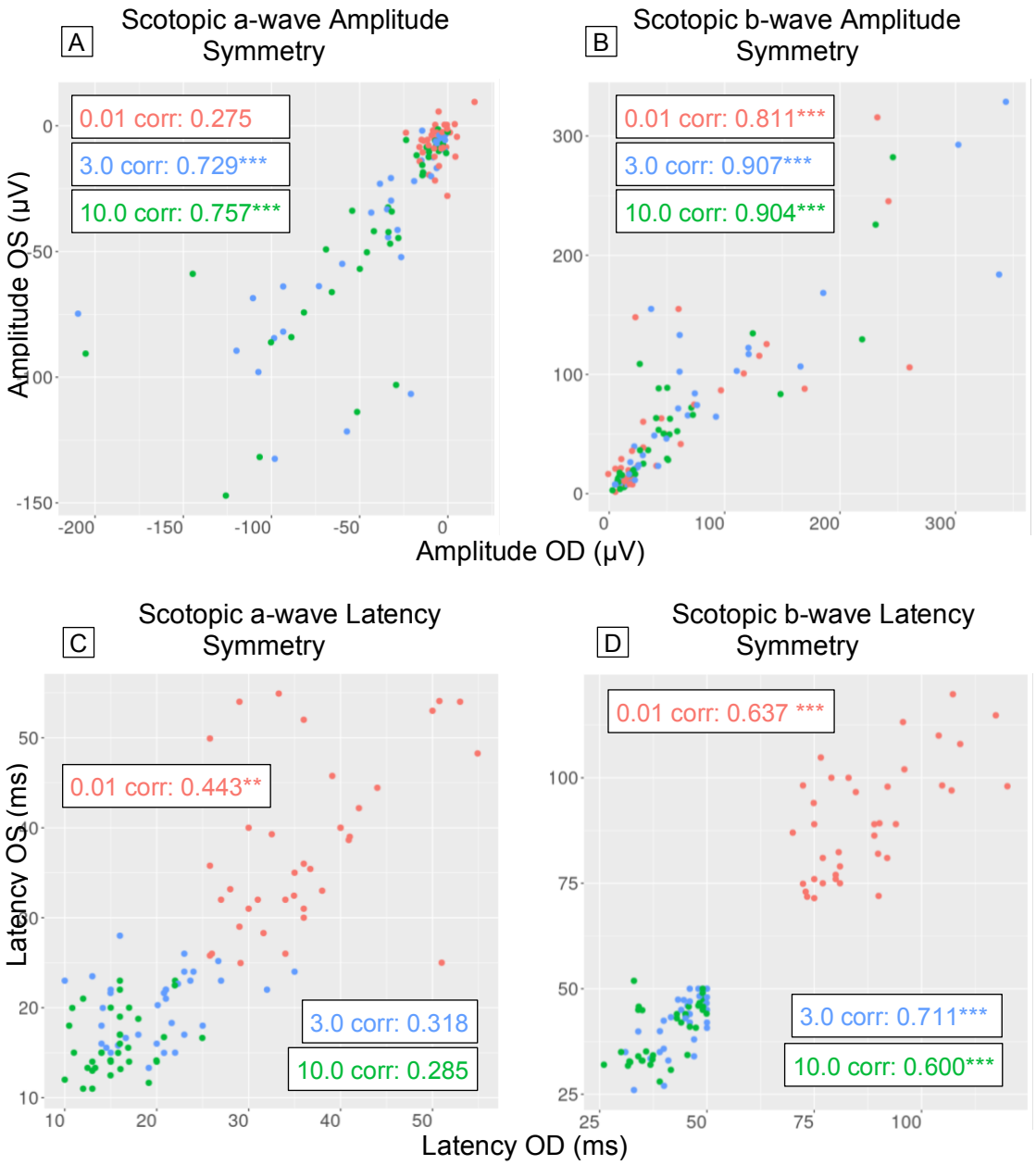

Figure 3.15. Correlation of scotopic ERG responses between eye pairs. The correlation of scotopic a-wave (A, C) and b-wave (B, D) amplitude (A, B) and latency (C, D) between OD and OS for patients with data for both eyes. Each scatter plot represents each patient's scotopic response pair as a single point with the Pearson's correlation coefficient and degree of significance. (A) a-wave amplitude is not symmetrical between eyes for 0.01 (r=0.275, p>0.05) and moderately symmetrical for 3.0 (r=0.729, p<0.001) and 10.0 (0.757, p<0.001) (B) b-wave amplitude is shown to be highly symmetrical between eyes for 0.01 (r=0.811, p<0.001), 3.0 (r=0.907, p<0.001) and 10.0 (r=0.904, p<0.001). (C) a-wave latency has low symmetry between eyes for 0.01 (r=0.443, p<0.01), and no symmetry between eyes for 3.0 (r=0.318, p>0.05) and 10.0 (r=0.285, p>0.05). (D) b-wave latency is moderately symmetrical between eyes for 0.01 (r=0.637, p<0.001), 3.0 (r=0.711, p<0.001) and 10.0 (r=0.600, p<0.001). µV = microvolts. ms = millisecond.

3.4 Rates of disease progression for each of the parameters

3.4.1 Ellipsoid zone shortening with time

EZ measurements were taken on each OCT image by two independent readers. The EZ measurements between the two readers showed excellent agreement with an intraclass coefficient (ICC) of 99.9% (95% Cl, 0.999 – 0.999; P < 0.001). The mean difference between lengths was 43.85 µm and 95% of all values fell within ±109.88 µm, as shown in the Bland-Altman plot in Figure 3.16. For 64 patients who had an OCT acquired, 20 patients only had one scan taken and 44 patients had at least 2 scans or more. After exclusion of scans where the ellipsoid zone was not discernible or extended past the OCT raster, 68 eyes of 36 patients were analysed. Mean baseline ellipsoid zone length was 3170.11 ± 1431.62 µm, with a median of 2966.44 µm while the mean EZ length at last follow up visit was 2448.56 ± 1321.14 µm with a median of 2190.28 µm. The average number of OCTs per patient was 3.76 ± 4.25 up to a maximum of 27 OCTs for one patient in the cohort. Progression calculations were based on 31 patients with at least 2 ellipsoid zone length measurements.

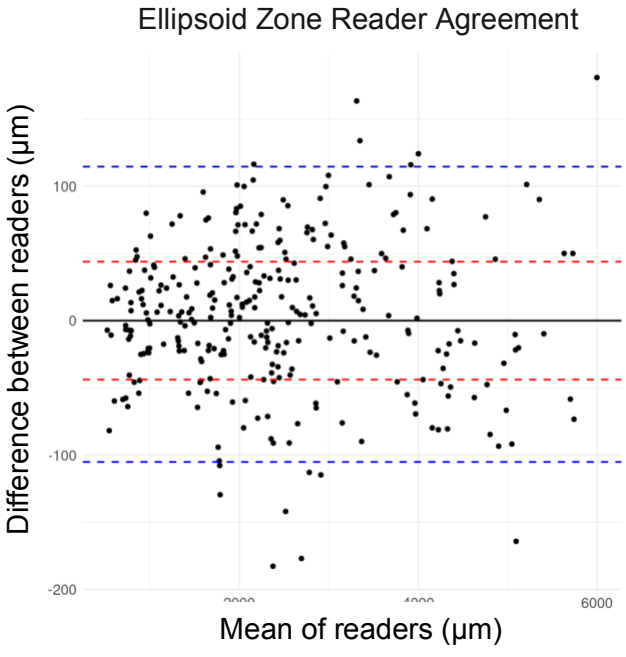

Figure 3.16. Bland-Altman plot showing the difference in ellipsoid zone length measurements between readers. Mean difference in EZ length (dashed red lines) and 95% limits of agreement (blue dashed lines) are shown. Difference of 0° is shown as a solid black line. There is less variation with "full-length" measurements, due to less ambiguity and subjective influence in determining the ellipsoid zone limits. µm = micrometres.

The structural measurements at each follow up time are shown in Figure 3.17. The data points were best fit with linear regression, which provided an estimate of the progression rate for each patient. All patients showed an EZ length decrease with a mean annual progression rate from baseline of 195.05 µm/year (7.65% per year, SE = 55.87, p-value < 0.0001). A significant difference in rate of structural progression was observed when comparing the ellipsoid zone length when patients were grouped by baseline size (<3000 µm and ≥ 3000 µm), which indicated a slowdown in disease progression as photoreceptor death approaches the fovea. Larger measurements (≥3000 µm) at baseline showed a markedly faster rate of progression at 322.62 µm/year (10.20% per year, SE = 101.50, p-value < 0.0001), and smaller measurements (<3000 µm) showed a slower rate of progression at 102.51 µm/year (5.28% per year, SE = 54.28, p-value < 0.0001) (see Table 7). An independent two-sample t-test confirmed that the difference between progression rates was statistically significant ($p < 0.05$).

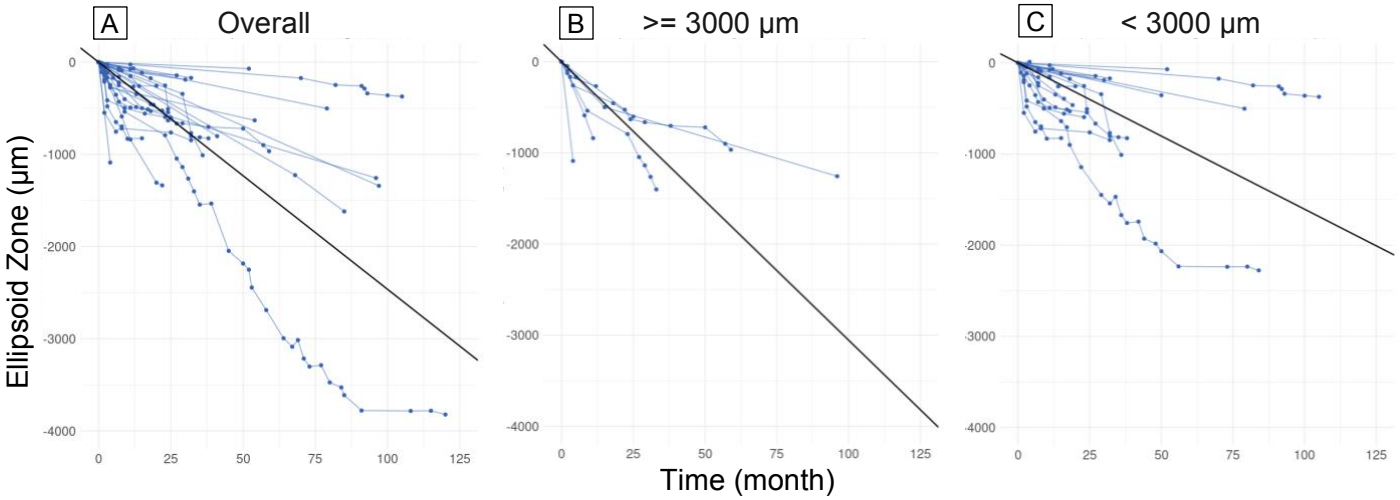

Figure 3.17. Structural progression of ellipsoid zone for patients with retinitis pigmentosa over a 10-year follow-up period. Subjects (n=31) have been centred to start at the same time to show the change over time more clearly. Each blue line represents one patient's progression based on the average of left and right eye measurements. A solid black line depicts the mean rate of decline across all patients. (A) The overall progression based on the entire dataset. (B) Progression based on data from subjects with a baseline EZ length ≥ 3000 µm. (C) Progression based on data from subjects with a baseline EZ length < 3000 µm. µm = micrometres.

Table 7. Rate of progression in RP via SD-OCT					
Outcome	**Progression (%/year)**	**Progression (µm/year)**	**Standard Error**	**p-value**	
Overall Ellipsoid Zone	7.65	195.05	55.87	< 0.001	
Baseline ≥ 3000 µm	10.20	322.62	101.50	< 0.001	0.042
Baseline <3000 µm	5.28	102.51	54.28	< 0.001	

This suggests that retinitis pigmentosa progresses in 1st order rate with exponential decay, modelled in Figure 3.18. In a first-order decay process, the rate of decay is directly proportional to the quantity of the substance present. In other words, as time progresses, the rate at which the quantity decays decreases, but the decrease is continuous and gradual. In the context of RP, this indicates that the rate of ellipsoid zone shortening is directly proportional to the density and number of remaining healthy photoreceptor cells, but the photoreceptor cell death is continuous and gradual. As there was sufficient data, the progression of autosomal recessive and autosomal dominant subgroups were also modelled (Figure 3.18), which showed that the autosomal dominant group experiences a lower and stable rate of progression (4.75% annually, $p<0.05$) compared to the autosomal recessive RP group (6.01% annually, $p<0.01$) (Table 8). An analysis of variance (ANOVA) test revealed a statistically significant difference in the regression lines among the two inheritance groups ($p < 0.05$). The observed progression rate within the cohort characterized by genetic ambiguity exhibited the most pronounced annual decrease in EZ length, reaching 7.49% ($p<0.001$), likely attributable to the presence of X-linked RP cases. The autosomal recessive exponential slope is very closely aligned with the overall exponential slope, which may suggest that many patients in the OEI cohort with unknown genetic aetiology could also share an autosomal recessive inheritance pattern.

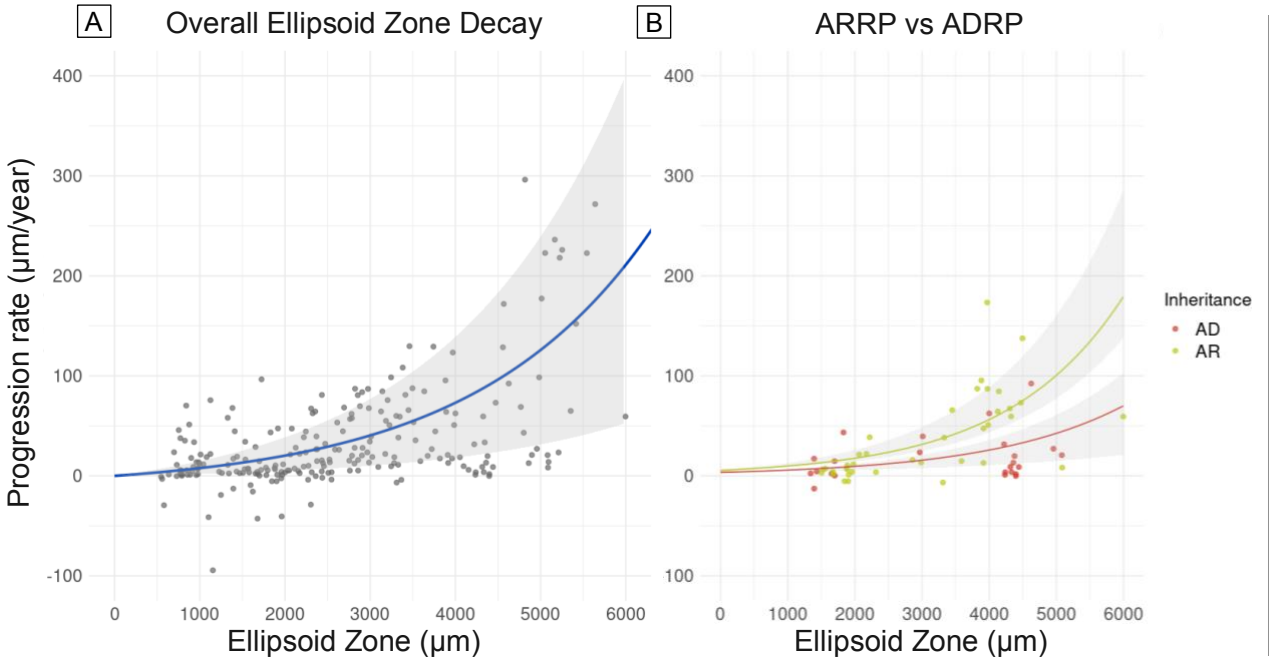

Figure 3.18. Relationship between the initial ellipsoid zone width and progression rate over one month. (A) For 31 patients with multiple ellipsoid zone (EZ) measurements, the rate of change between each consecutive b-scan was examined. The blue line shows the progression rate (in microns/year) of the ellipsoid zone length decrease at different baseline lengths (in microns). There is an increasing density of photoreceptors closer to the fovea and the exclusive presence of cone photoreceptors in the central 10° of the retina (approx. 1000-1100 µm). As the density of photoreceptors increases, the rate of total photoreceptor loss decreases. (B) The difference in progression rates between genetic inheritance groups for 10 patients. Red points represent data points from patients with autosomal dominant (AD) RP and green points from patients with autosomal recessive (AR) RP. The ADRP group experiences a lower and stable rate of progression compared to the ARRP group (p=0.037). The grey bands represent the 95% point-wise confidence intervals. µm = micrometres.

Table 8. Rate of ellipsoid zone progression in RP as a factor of genetic inheritance. SE = Standard Error.

Inheritance	%/year	µm/year	SE	p-value	
Unknown	7.49	177.51	43.31	<0.001	
Autosomal recessive	6.01	153.21	50.15	0.006	0.035
Autosomal dominant	4.75	51.81	32.29	0.020	

3.4.2 Humphrey mean deviation decrease with time

For 27 patients who had a Humphrey visual field exam, 11 underwent at least one 30-2 protocol, 12 underwent at least one 24-2 protocol, and 7 underwent at least one 10-2 testing protocol. Baseline mean deviation (MD) was -20.23 ± 7.81 dB with a median of -20.27 dB for 30-2, -9.62 ± 7.60 dB with a median of -16.21 dB for 24-2, and -20.23 ±

16.13 dB with a median of -27.62 dB for 10-2. The average number of HVFs per patient was 2.43 ± 2.41 up to a maximum of 9 HVFs for one patient in the cohort. Following the exclusion of visual field examinations impacted by secondary conditions affecting the central visual field, such as cataracts, a total of 22 patients were analysed. Progression calculations were based on patients with at least 2 or more HVF exams, which consisted of 4 patients for 30-2, 3 patients for 24-2, and 2 patients for 10-2 (Figure 3.19). Since MD values are logarithmically converted from retinal sensitivity, a decrease in MD values can be considered in linear fashion (rather than needing to convert from a logarithmic dB scale to a linear 1/Lambert scale). All patients showed a decline in mean deviation between 0.40-1.03 dB a year, but with poor statistical significance due to the small sample size for each protocol (Table 9).

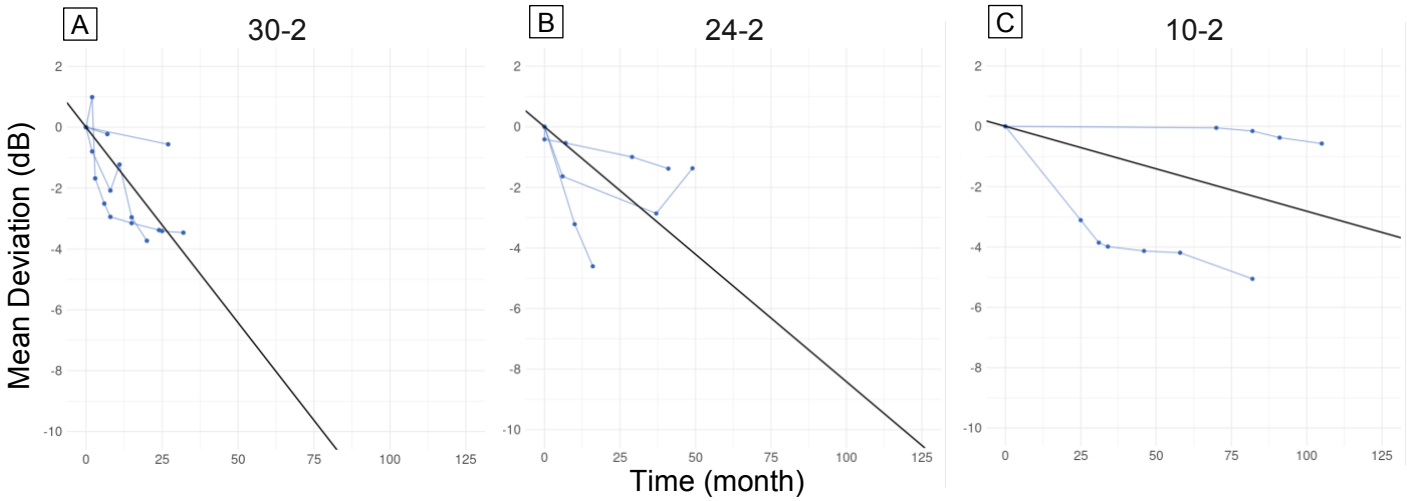

Figure 3.19. Functional visual field progression via automated perimetry for patients with retinitis pigmentosa over a 10-year follow-up period. Subjects (n=9) have been centred to start at the same time to show the change over time more clearly, where each line represents each patient's progression based on the average of left and right eye measurements. A solid black line depicts the mean rate of decline for the data of each graph. (A) The overall progression based on the 30-2 protocol. (B) Progression based on the 24-2 protocol. (C) Progression based on the 10-2 protocol. dB = decibels.

Table 9. Rate of progression in RP via HVF. SE = Standard Error.

Protocol	%/year	dB/year	SE	p-value
30-2 MD	6.35	1.03	0.46	0.111
24-2 MD	4.29	0.93	0.35	0.086
10-2 MD	1.57	0.40	0.19	0.131

3.4.3 Goldmann rate of isopter constriction

Isopter length measurements were recorded by two independent readers for each GVF test. The isopter length measurements between the two readers showed near-perfect agreement with an ICC of 99% (95% Cl, 0.99 – 0.99; P < 0.001). The mean difference between lengths was 0.32 degrees and 95% of all values fell within ± 1.35 degrees, as shown in the Bland-Altman plot in Figure 3.20. The inter-technician variability was also examined. Where HVF is more objective and "improvements" could be due to management of secondary conditions or patient fatigue, GVF has a human-operator factor. I compared percent variation between consecutive exams where there was an improvement and categorized them by either technician if the technician changed between the consecutive exams, or by patient if the technician remained the same. In 11 instances where there was an improvement between consecutive scans, 8 had a tech change and 3 did not. On average, there was 21.52% variation upon examiner change, and 12.62% when the examiner remained the same (Figure 3.21).

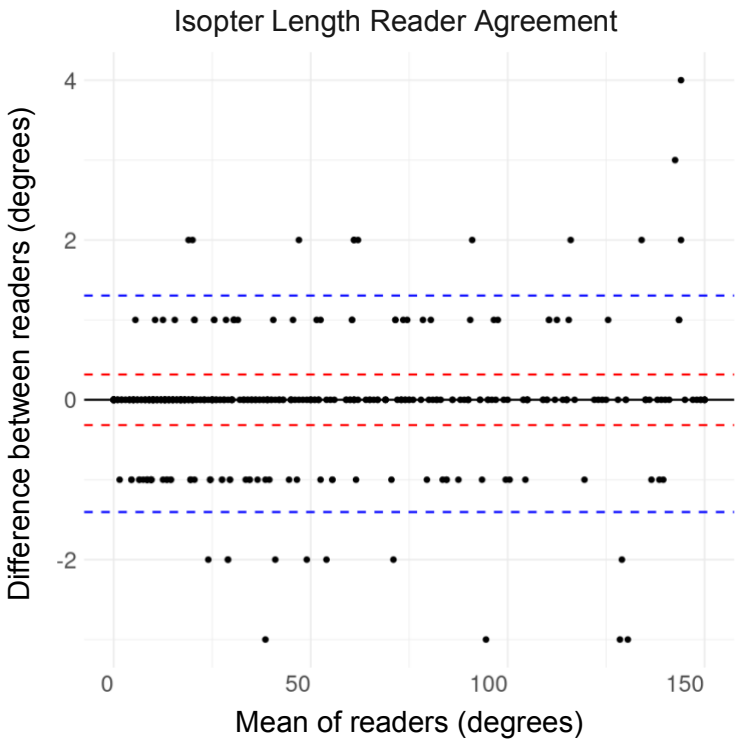

Figure 3.20. Bland-Altman plot showing the difference in isopter length measurements between readers. Mean difference in isopter length (dashed red lines) and 95% limits of agreement (blue dashed lines) are shown. Difference of 0° is shown as a solid black line. As the field grows larger, the deviation between the readers is a bit higher.

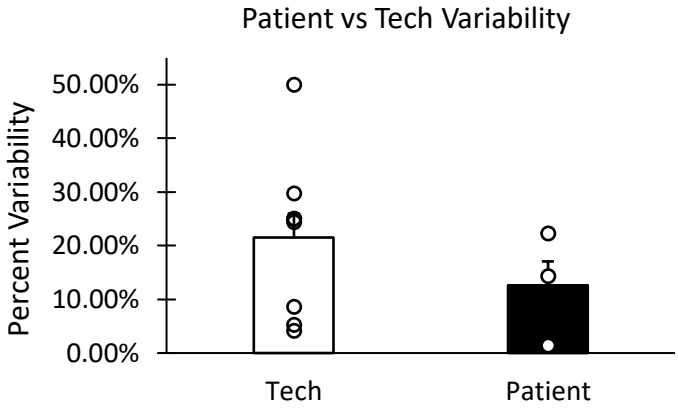

Figure 3.21. Technician contribution to test-retest variability. The test-retest variability was examined when there was a technician change between exams for the same patient and when the technician remained the same. On average, readings varied by 21.52% upon examiner change, and 12.62% when the examiner remained the same.

For 36 patients who had a GVF exam, 24 patients had only one exam performed and 12 patients had at least 2 exams or more. Mean baseline isopter length was 79.18 ± 43.59° with a median of 96° for V4e, 59.78 ± 37.82° with a median of 60° for III4e, 31.95 ± 28.30° with a median of 19° for I4e, 20.64 ± 22.37° with a median of 14° for I3e, and 13.57 ± 17.22° with a median of 9° for I2e. The average number of GVFs per patient was 1.67 ± 1.35 up to a maximum of 8 GVFs. Progression calculations were based on 11 patients with at least 2 length measurements for isopters V4e, I4e, I3e and I2e, and 9 patients with at least 2 length measurements for isopter III4e. This difference was due to the use of isopter III4e primarily for Goldmann driving license maintenance exams. Most patients showed an isopter boundary constriction (Table 10), with annual decreases of 5.14° for V4e (4.86%, $p < s0.001$), 3.44° for III4e (7.77%, $p < 0.001$), 2.41° for I4e (6.77%, $p < 0.001$), 1.48° for I3e (6.80%, $p < 0.05$), and 2.15° for I2e (12.45%, $p < 0.05$) (Figure 3.22). The difference in progression rates between isopters was significant when there was at least 2 stimulus sizes of difference (i.e., V4e to I4e, or I4e to I2e) (Table 11).

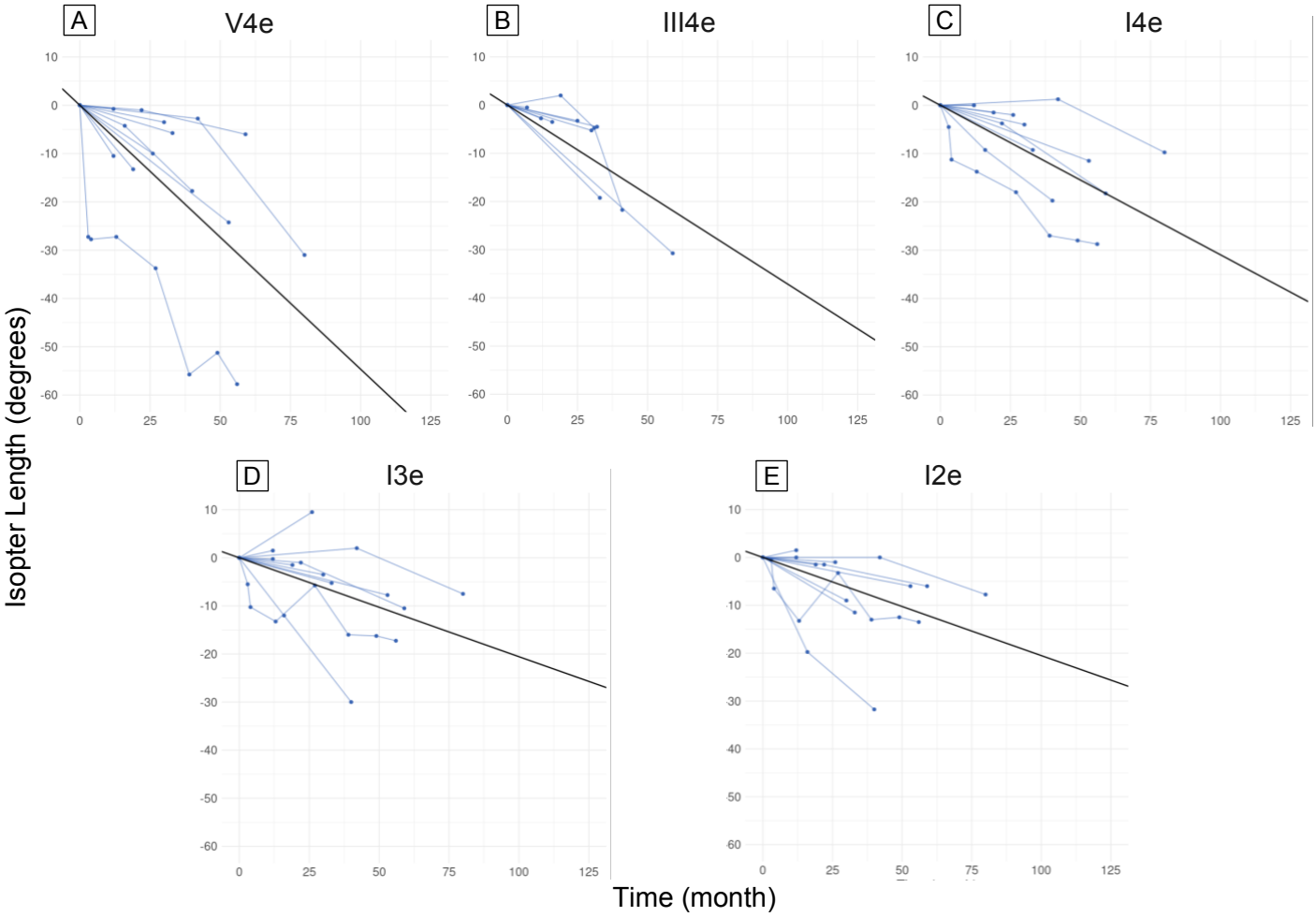

Figure 3.22. Goldmann isopter constriction for patients with retinitis pigmentosa over a 10-year follow-up period. Subjects (n=9-11) have been centred to start at the same time to show the change over time more clearly, where each line represents each patient's progression based on the average of left and right eye measurements. A solid black line depicts the mean rate of decline for the data of each graph. (A) The overall progression for the V4e isopter. (B) Progression for the III4e isopter. (C) Progression for the I4e isopter. (D) Progression for the I3e isopter. (E) Progression for the I2e isopter.

Table 10. Rate of progression in RP via GVF. SE = Standard Error.

Isopter	%/year	deg/year	SE	p-value
V4e	5.22	5.14	0.81	<0.001
III4e	7.77	3.44	0.54	<0.001
I4e	6.77	2.41	0.45	<0.001
I3e	6.80	1.48	0.68	0.042
I2e	12.45	2.15	0.61	0.002

Table 11. Difference in progression rates (deg/year) between isopter sizes.

	V4e	III4e	I4e	I3e	I2e
V4e		-1.70, p=0.088	-2.73, p<0.01	-3.67, p<0.01	-2.99, p<0.01
III4e	-1.70, p=0.088		-1.03, p=0.150	-1.97, p<0.05	-1.29, p<0.05
I4e	-2.73, p<0.01	-1.03, p=0.150		-0.94, p=0.258	-0.26, p=0.734
I3e	-3.67, p<0.01	-1.97, p<0.05	-0.94, p=0.258		0.68, p=0.462
I2e	-2.99, p<0.01	-1.29, p<0.05	-0.26, p=0.734	0.68, p=0.462	

3.4.4 ERG amplitude attenuation and latency increase

Of the 41 patients who had a full-field ERG and 30 who had a multi-focal ERG, 8 patients had at least two full-field ERGs and 3 had at least two multi-focal ERGs. The maximum number of ERGs performed on one patient was 3; 4 patients had 3 full-field ERGs and only one patient had 3 multi-focal ERGs. Amplitude alone was assessed as justified in section 3.3. For mfERG, progression of P1 amplitude per unit area revealed unexpected overall trends of improvement for rings 1-3, and a slight decline for rings 4-5 (Figure 3.23). Clinical notes for each patient did not explain this change but could possibly be due to management of a secondary condition or monitoring the effect of a medication. In any case, due to the small sample size, the trends were not deemed to be statistically significant for all responses of each ring.

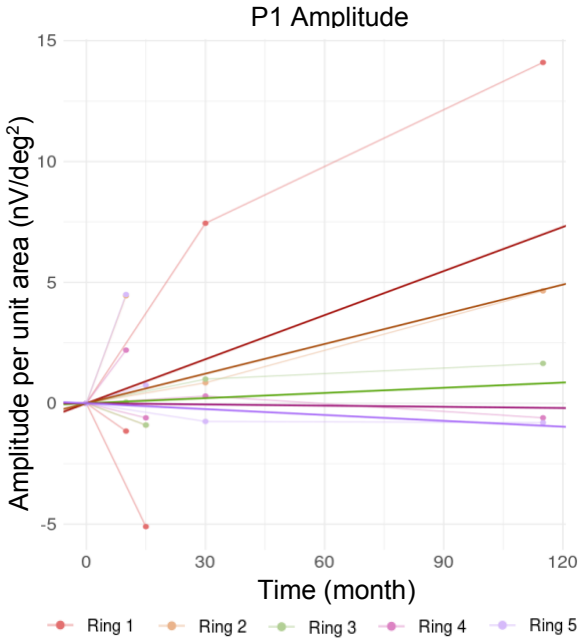

Figure 3.23. mfERG P1 Amplitude attenuation for patients with retinitis pigmentosa over a 10-year follow-up period. Subjects (n=3) have been centred to start at the same time to show the change over time more clearly, where each line represents each patient's progression based on the average of left and right eye measurements, colour-coded by ring. A matching darker line depicts the mean rate of change for each ring. There is a positive change over time for Rings 1-3, and a slight decline for Rings 4-5.

For ffERG, progression of the 30Hz flicker peak amplitude was found to be statistically significant with an attenuation rate of 2.47 µV per year (10.99%, $p<0.05$) (Figure 3.24). Photopic a- and b-waves both showed a mean attenuation of amplitude over time (Figure 3.25), although neither was found to be statistically significant. Note that since a-wave is a negative deflection, values become increasing positive towards zero (hence the positive

slope). Finally, scotopic a- and b-wave also showed a mean attenuation of amplitude over time for all luminance intensities, that increased with increasing luminance (Figure 3.26). Due to the high variability, progression was not deemed to be statistically significant for the 1.0 and 3.0 cd·s/m^2 luminance responses. The strongest luminance, 10.0 cd·s/m^2 showed significant attenuation of 3.98 µV a year (10.53%, $p<0.05$) for the a-wave and 5.68 µV a year (8.41%, $p<0.01$) for the b-wave.

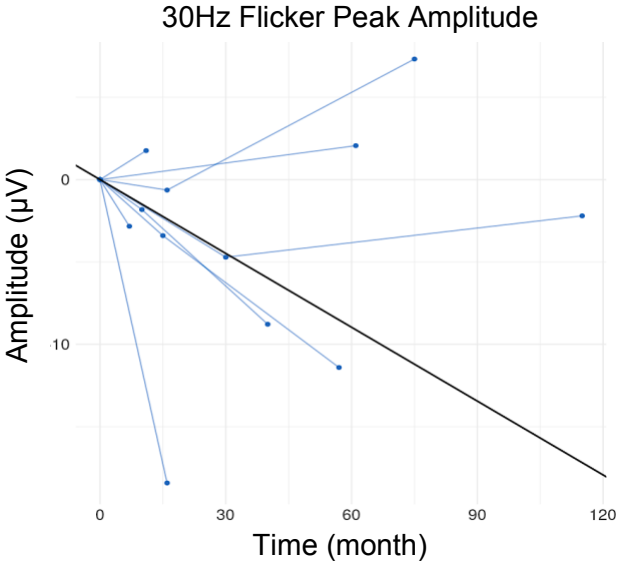

Figure 3.24. ffERG 30Hz flicker peak amplitude attenuation for patients with retinitis pigmentosa over a 10-year follow-up period. Subjects (n=8) have been centred to start at the same time to show the change over time more clearly, where each line represents each patient's progression based on the average of left and right eye measurements. A solid black line depicts the mean rate of decline for all patients. µV = microvolts.

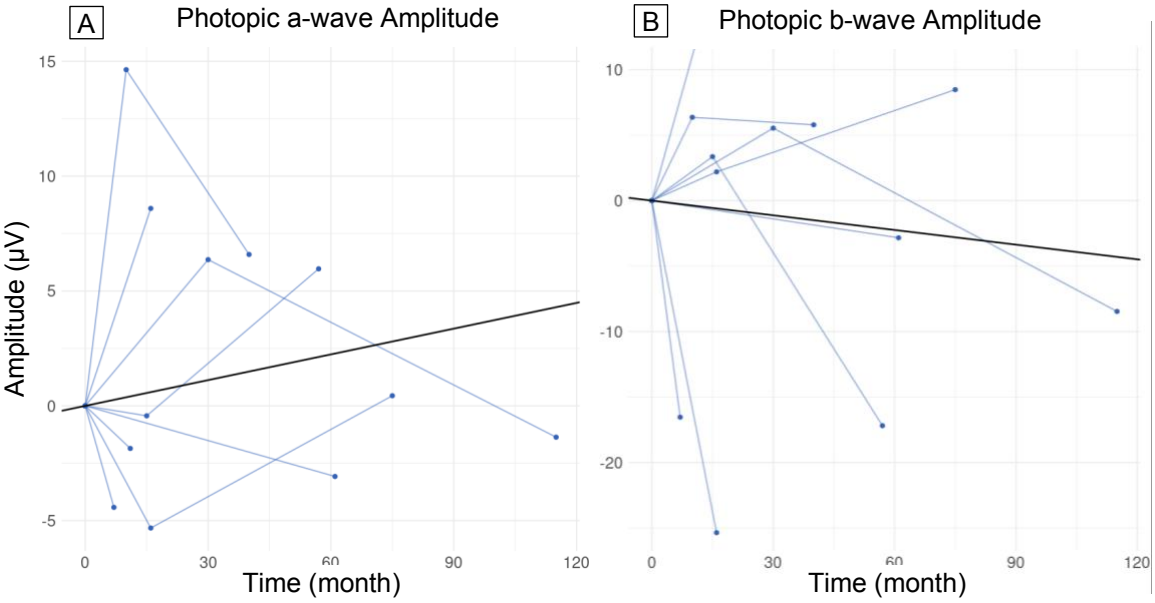

Figure 3.25. ffERG photopic a- and b-wave amplitude change for patients with retinitis pigmentosa over a 10-year follow-up period. Subjects (n=8) have been centred at 0 to show the change over time more clearly, where each line represents each patient's progression based on the average of left and right eye measurements. (A) Change in a-wave amplitude. (B) Change in b-wave amplitude. A solid black line depicts the mean rate of decline for the data of each graph. µV = microvolts.

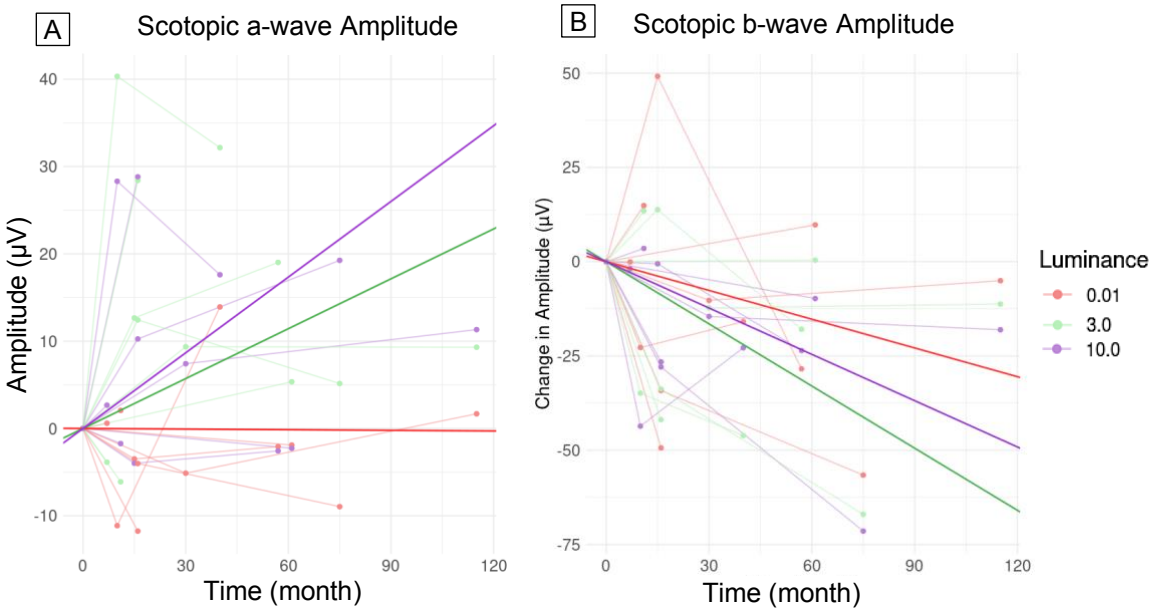

Figure 3.26. ffERG scotopic a- and b-wave amplitude change across 3 luminance intensities for patients with retinitis pigmentosa over a 10-year follow-up period. Subjects (n=8) have been centred to start at the same time to show the change over time more clearly, where each line represents each patient's progression based on the average of left and right eye measurements, colour-coded by luminance intensity. (A) Change in a-wave amplitude. (B) Change in b-wave amplitude. A matching darker line depicts the mean rate of change for each ring. Rate of amplitude attenuation increases with increasing luminance. μV = microvolts. Luminance = 0.01, 3.0, and 10.0; cd·s/m^2 = candela second per square meter (constant luminance).

3.5 Correlations between different diagnostic variables

As retinitis pigmentosa progresses in a 1st order exponential decay pattern, univariate linear regression was used between the five diagnostic modalities with the Pearson correlation coefficient. This section is divided in two parts: one examining the correlation of diagnostic modalities encompassing the entire retinal field (the Goldmann visual field (GVF) and full-field electroretinography (ffERG)) and the other focusing on correlations between diagnostic test that evaluated the central 30° (optical coherence tomography (OCT), Humphrey visual field (HVF), and multifocal electroretinography (mfERG)). The central 30° represents the macular region of the retina centred at the fovea, with a radius of 30° and diameter of 60°. In specific instances, the correlation between diagnostic modalities which overlapped these two retinal fields was examined. These exceptions occurred under the following circumstances: when the isopter lengths in GVF testing were equal to or less than 60°, and when examining the cone-driven photopic and 30Hz flicker response of the ffERG due to the lack of cones outside of the macular region. Tests which analysed the same function were not correlated with one another, such as ffERG and mfERG or HVF and GVF. Ellipsoid zone measurements that extended beyond the OCT limits (approx. > 6000 μm), were not included in the calculation of correlation, since it was difficult to determine the length of the EZ beyond the OCT field of view. However, they were still graphically represented to demonstrate the variability of function. For example, a patient with an ellipsoid zone of 8000 μm would have a different level of functional vision compared to a patient with an ellipsoid zone of 18000 μm. Although both patients might exhibit seemingly "healthy" ellipsoid zones on OCT imaging, there would exist a substantial variance in remaining photoreceptor density between them.

3.5.1 Correlation between diagnostic tests evaluating the central 30° of retina

In this section, I investigate the progression of retinitis pigmentosa through the correlation of diagnostic modalities which centre their analysis on the central 30° of the retinal field.

3.5.1.1 Relationship of ellipsoid zone to mean deviation

This analysis is comprised of 23 patients who underwent both an OCT image capture and automated perimetric exam within 3 months of one another. We investigated whether there would be a similar pattern of decay between the ellipsoid zone length and the mean deviation of each testing protocol. Mean deviation was found to decrease linearly with ellipsoid zone shortening. While all testing protocols showed significant correlation with the ellipsoid zone length, correlation increased the more central the testing protocol strategy. The correlation coefficient for the 30-2 protocol was 0.63 ($p<0.001$), which increased to 0.99 for 24-2 ($p<0.001$), and 0.63 for 10-2 ($p<0.001$) (Figure 3.27).

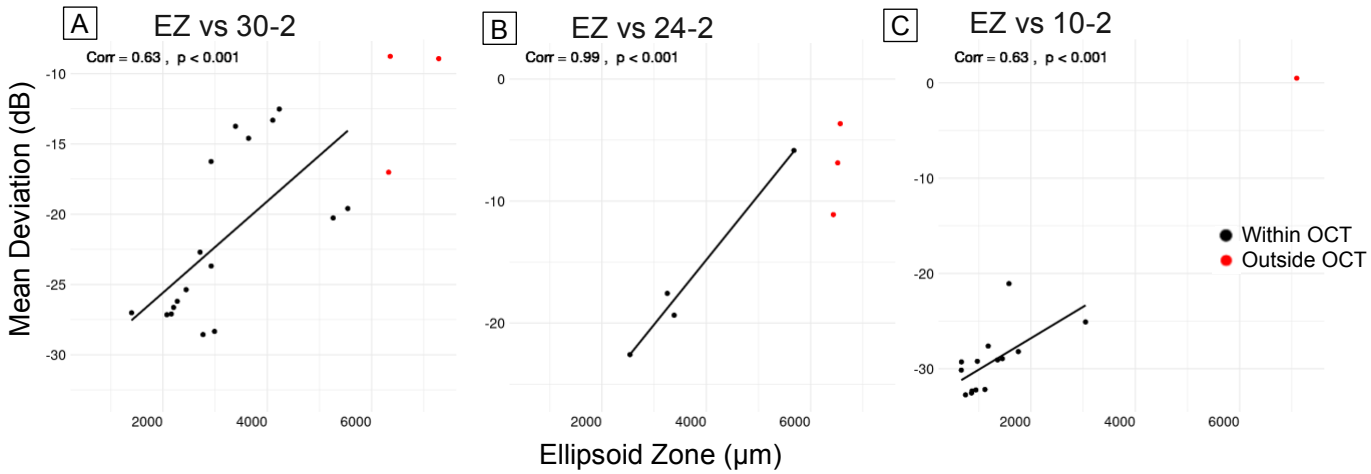

Figure 3.27. Correlation of ellipsoid zone length and Humphrey visual field mean deviation for patients with retinitis pigmentosa. Scatterplots show OCT ellipsoid zone length measurement and mean deviation values taken within 3 months of one another. A solid black line depicts the relationship between the diagnostic tests. Red points represent EZ lengths extending beyond the OCT limits and are not included in the correlation. (A) 30° testing strategy, r=0.63 ($p < 0.001$). (B) 24° testing strategy, r=0.99 ($p < 0.001$). (B) 10° testing strategy, r=0.63 ($p < 0.001$). dB = decibels. µm = micrometres.

3.5.1.2 Relationship of ellipsoid zone to central isopter constriction

This analysis is comprised of 33 patients who underwent both an OCT and GVF exam within 3 months of one another. Correlation was analysed on a subset of the GVF data excluding measurements above 60°. GVF isopter length was overall found to decrease with EZ shortening (Figure 3.28), however V4e showed low correlation (r=0.31, p=0.183), whereas III4e, I4e, I3e, I2e showed moderate correlation coefficients of 0.69 (p<0.05), 0.50 (p < 0.001), 0.52 (p<0.001) and 0.56 (p<0.001), respectively.

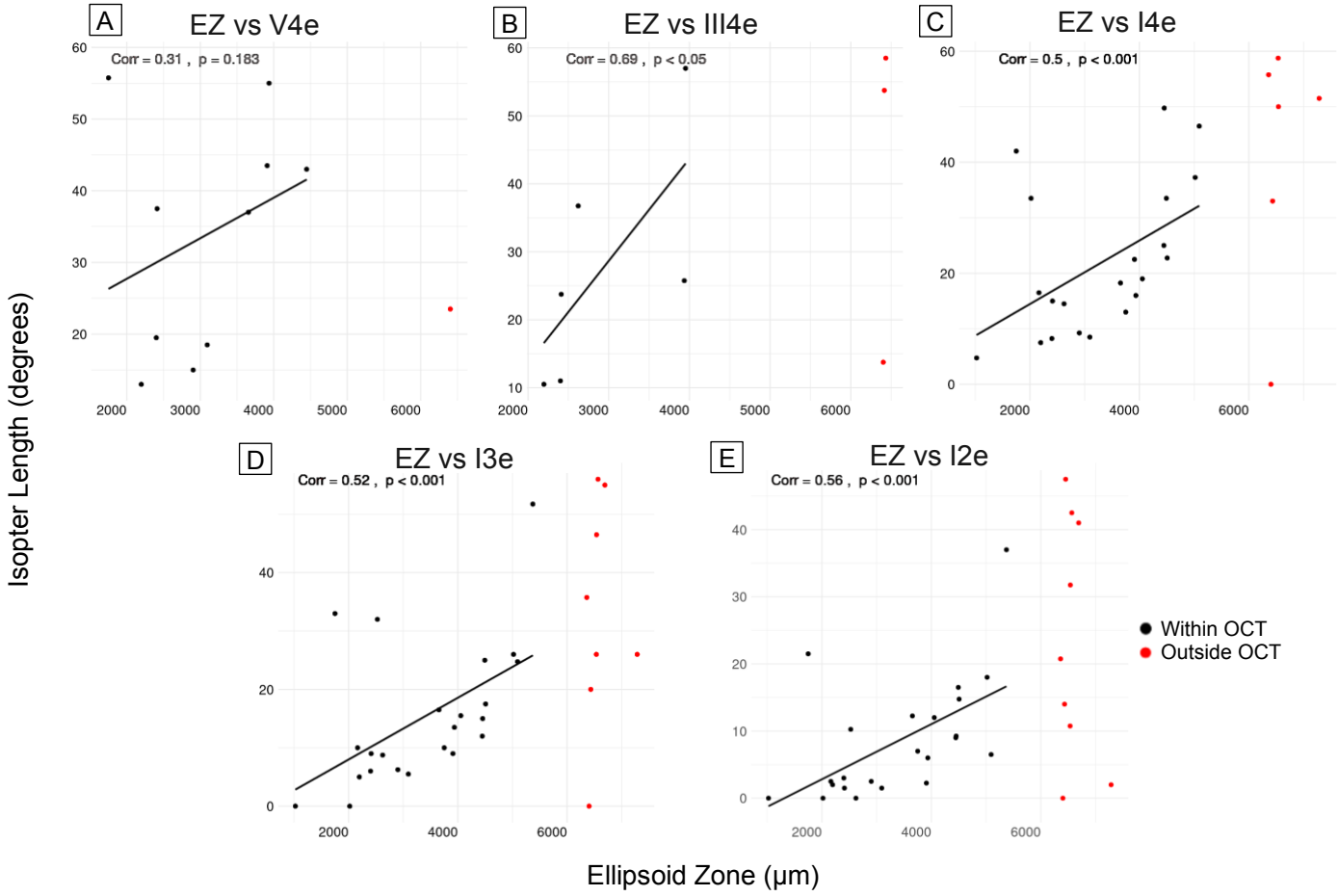

Figure 3.28. Correlation of ellipsoid zone length and Goldmann isopter length for patients with retinitis pigmentosa. Scatterplots show OCT ellipsoid zone length measurement and GVF isopter length measurement taken within 3 months of one another. A solid black line depicts the relationship between the diagnostic tests. Red points represent EZ lengths extending beyond the OCT limits and are not included in the correlation. (A) V4e, r=0.31 (p=0.183). (B) III4e, r=0.69 (p<0.05). (C) I4e; r=0.50 (p<0.001). (D) I3e, r=0.52 (p<0.001). (E) I2e, r=0.56 (p<0.001). µm = micrometres.

3.5.1.3 Relationship of ellipsoid zone to mfERG amplitude

This analysis consists of 28 patients who had both an OCT and mfERG within 3 months of one another. P1 amplitude decreased with EZ shortening across all 5 rings (Figure 3.29). Rings 1 and 2 had moderate correlations of 0.73 ($p < 0.001$) and 0.79 ($p < 0.001$), whereas rings 3 and 5 had low correlations of 0.47 ($p < 0.001$) and 0.57 ($p < 0.001$), and ring 4 had a low correlation and statistical significance of 0.20 ($p=0.208$). The P1 amplitude of Rings 1,2 and 4 exhibited the strongest correlation with EZ length, perhaps attributable to their spatial alignment with regions of the highest photoreceptor density (Rings 1-2 for cones, Ring 4 for rods). A summary of correlations between EZ and mfERG, including latencies, can be found in the Appendix as Supplemental Table I.

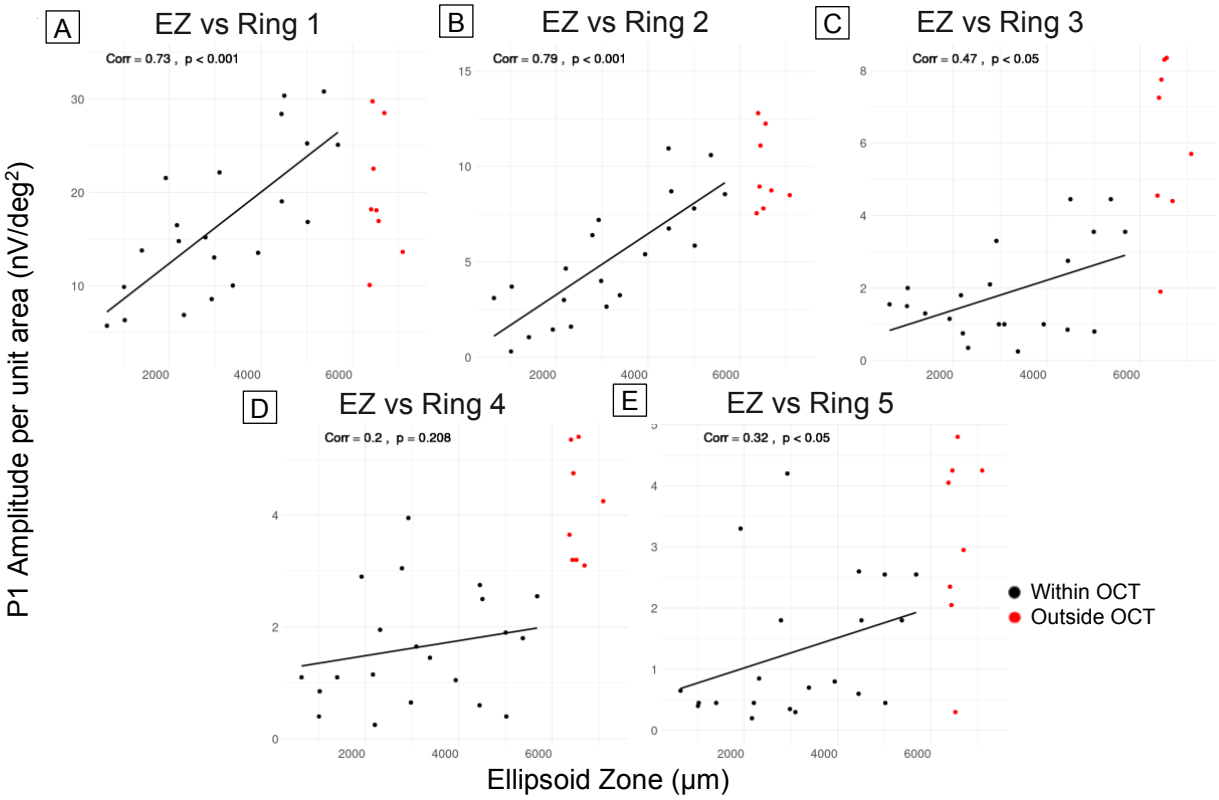

Figure 3.29. Correlation of ellipsoid zone length and multi-focal ERG P1 amplitude for patients with retinitis pigmentosa. Scatterplots show OCT EZ length and mfERG P1 amplitude per unit area readings taken within 3 months of one another. A solid black line depicts the relationship between the diagnostic tests. Red points represent EZ lengths extending beyond the OCT limits and are not included in the correlation. (A) Ring 1, r=0.73 ($p < 0.001$). (B) Ring 2, r=0.79 ($p < 0.001$). (C) Ring 3, r=0.47 ($p < 0.001$). (D) Ring 4, r=0.20 ($p = 0.208$). (E) Ring 5 P1, r=0.32 ($p < 0.05$). nv/deg^2 = amplitude/unit area. µm = micrometres.

3.5.1.4 Relationship of mean deviation to mfERG amplitude

This analysis consists of 10 patients who underwent both a HVF and mfERG test within 3 months of one another, which encompasses 4 patients for 30-2 and 6 patients for 24-2. There were no patients with mfERG and a 10-2 HVF. For 30-2, a significant correlation was found only with Ring 3, where P1 amplitude correlation was 0.74 ($p<0.05$) For 24-2, a significant correlation was found with multiple rings. P1 amplitude was correlated to MD by 0.61 ($p<0.05$) for Ring 2, by 0.74 ($p<0.01$) for Ring 3, 0.72 ($p<0.01$) for Ring 4, and by 0.61 ($p<0.5$) for Ring 5. The most significant correlations for 30-2 (Ring 3) and 24-2 (Ring 4) are displayed in Figures 3.30. The higher number of significantly correlated rings with 24-2 could be a factor of both a larger sample size and its higher spatial resolution (number of points tested) compared to the 30-2 test because it covers a smaller area of the visual field. This finer grid could make it potentially more sensitive to subtle retinal abnormalities that are detectable by mfERG. The complete summary of correlations between HVF and mfERG, including latencies, can be found in the Appendix as Supplemental Table III.

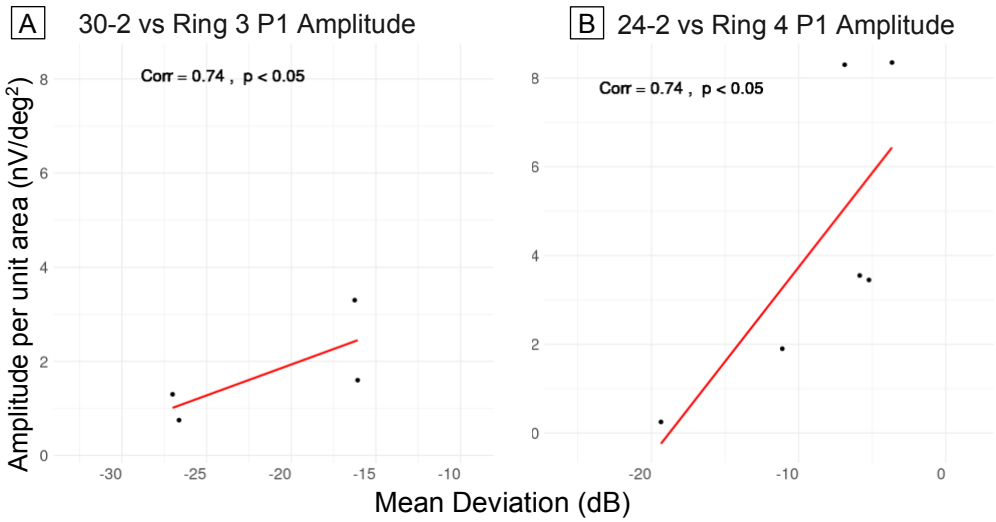

Figure 3.30. Correlation of mean deviation and multi-focal ERG P1 amplitude per unit area for patients with retinitis pigmentosa. Scatterplots show mean deviation and mfERG P1 amplitude readings taken within 3 months of one another. A solid red line depicts the relationship between the diagnostic tests. (A) 30-2 and Ring 3 P1 amplitude per unit area, $r=0.74$ ($p < 0.05$). (B) 24-2 and Ring 4 P1 amplitude per unit area, $r=0.74$ ($p<0.05$). nv/deg^2 = amplitude/unit area. dB = decibels.

3.5.1.5 Relationship of central isopter constriction to mfERG amplitude

Sixteen patients underwent both a GVF and mfERG test within 3 months of one another. Correlation was analysed on a subset of the GVF data excluding measurements above 60°. As there are 5 isopter sizes and 15 mfERG responses (for a total of 75 correlations), this section focuses on the relationship between the P1 amplitude and the length of each isopter. V4e, III4e, and I4e isopter lengths were not significantly correlated with the P1 amplitude of any ring, whereas I3e and I2e lengths were correlated to the P1 amplitude of all rings. I3e isopter lengths showed correlations of 0.43 ($p<0.05$), 0.47 ($p<0.01$), 0.48 ($p<0.05$), 0.52 ($p<0.01$), and 0.65 ($p<0.001$) for Rings 1-5, respectively. I2e showed correlations of 0.41 ($p<0.05$), 0.56 ($p<0.001$), 0.63 ($p<0.001$), 0.68 ($p<0.01$), and 0.74 ($p<0.001$) for Rings 1-5, respectively. Figure 3.31 displays the most correlated ring (ring 5) with isopters I3e and I2e. The complete summary of correlations between GVF and mfERG, including latencies, can be found in the Appendix as Supplemental Table IV.

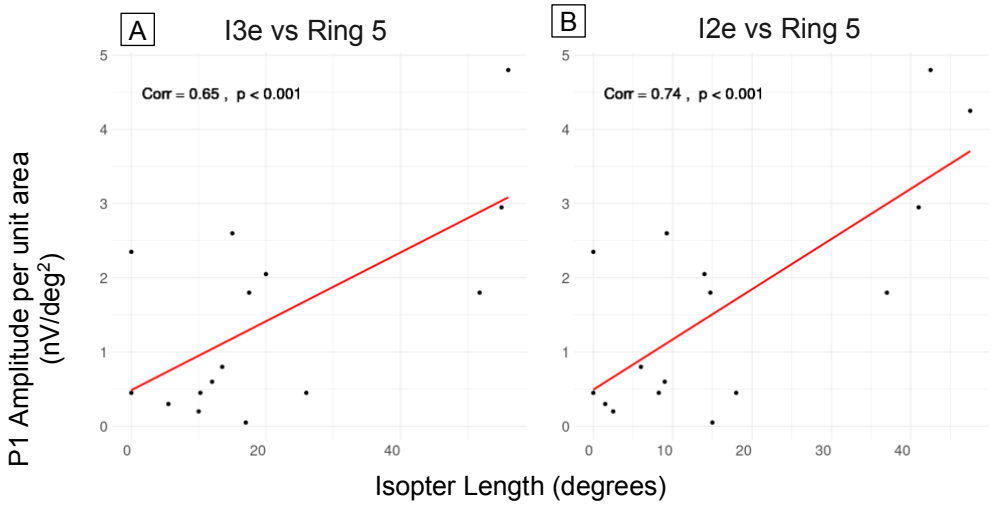

Figure 3.31. Correlation of Goldmann isopters I3e and I2e and multi-focal P1 amplitude responses in patients with retinitis pigmentosa. Scatterplots show the relationship between Goldmann isopter lengths and mfERG ring 5 P1 amplitudes. Measurements were taken within 3 months of one another. A solid red line depicts the relationship between the diagnostic tests. (A) I3e, r=0.65 ($p < 0.001$). (B) I2e, r=0.74 ($p < 0.001$). nv/deg^2 = amplitude/unit area. dB = decibel.

3.5.2 Correlation between diagnostic tests evaluating the total retina

In this section, I investigate the progression of retinitis pigmentosa through the correlation of diagnostic modalities which assess the entirety of the retinal field.

3.5.2.1 Relationship of rod amplitude to ellipsoid zone

Even though the ffERG assesses the function of the entire retina and OCT only examines the central 30°, I examined the relationship between these two parameters since most patients have advanced disease and their ffERG amplitudes would most likely be generated by photoreceptors found in their central retina due to extensive degeneration in the peripheral retina. This analysis consists of 38 patients who had both an OCT and scotopic ffERG within 3 months of one another. All scotopic amplitudes were significantly, although weakly, correlated with ellipsoid zone length, except for the a-wave amplitude of the 0.01 cd·s/m^2 luminance, where no notable relationship was observed ($r=-0.01$, $p=0.940$). This result makes sense in light of prior reports indicating the early extinguishment of the a-wave amplitude in the disease process, which could explain the lack of correlation in moderate to advanced disease. All other responses, including the 0.01 cd·s/m^2 b-wave amplitude and the 3.0 and 10.0 cd·s/m^2 luminance a- and b-wave amplitudes, showed some attenuation with EZ shortening, with correlations of 0.41 ($p<0.05$), -0.37 ($p<0.05$), 0.47 ($p<0.05$), -0.31 ($p<0.001$) and 0.40 ($p<0.001$), respectively (Figure 3.32). A complete summary of correlations for EZ and ffERG, including latencies, can be found in the Appendix as Supplemental Table II.

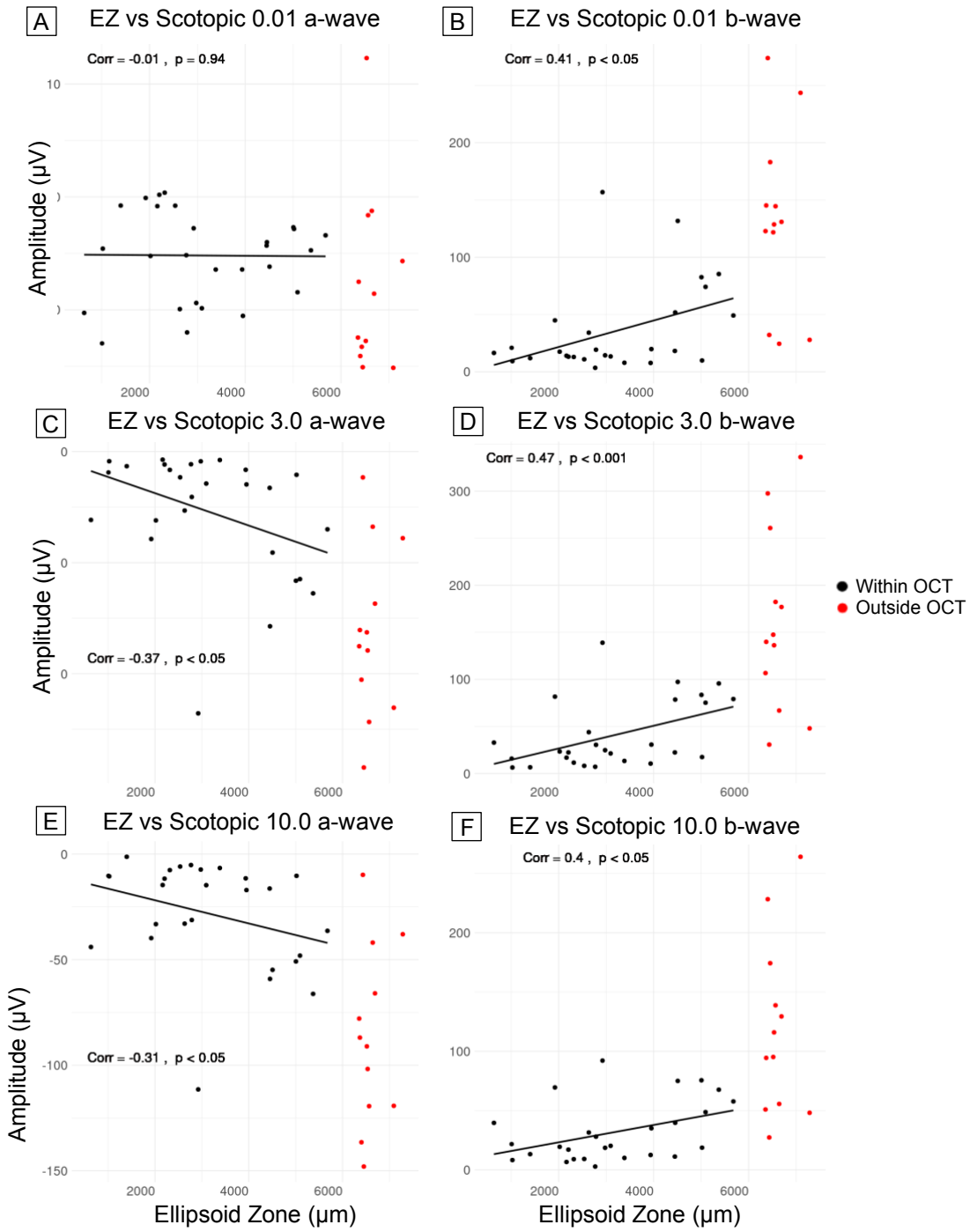

Figure 3.32. Correlation of ellipsoid zone and rod photoreceptor function for patients with retinitis pigmentosa. Scatterplots show EZ length measurements with a-wave (A, C, E) and b-wave (B, D, F) amplitudes taken within 3 months of one another, A solid black line depicts the relationship between the diagnostic tests. Red points represent EZ lengths extending beyond the OCT limits and are not included in the correlation. (A, B) Correlation of mean deviation with scotopic 0.01 cd·s/m^2 luminance; r=-0.01 (p=0.940) for a-wave and r=0.41 (p<0.05) for b-wave. (C, D) Correlation of mean deviation with scotopic 3.0 cd·s/m^2 luminance; r=-0.37 (p<0.05) for a-wave and r=0.47 (p<0.001) for b-wave. (E, F) Correlation of mean deviation with scotopic 10.0 cd·s/m^2 luminance; r=-0.31 (p<0.05) for a-wave and r=0.40 (p<0.05) for b-wave. µV = microvolts. dB = decibels.

3.5.2.2 Relationship of cone amplitude to ellipsoid zone

Even though the ffERG assesses the function of the entire retina and OCT only examines the central 30°, I examined the relationship between these two parameters since the concentration of cone photoreceptor cells are exclusively located in the central 30°. This analysis consists of 38 patients who had both an OCT and photopic ffERG within 3 months of one another. Here, only a- and b-wave amplitudes and 30Hz flicker amplitude were significantly correlated with ellipsoid zone length. Figure 3.33 highlights the correlations between ellipsoid zone length and cone-mediated ERG amplitude responses. Photopic a-wave amplitude was significantly diminished with EZ shortening, with a correlation of -0.42 ($p<0.001$). Photopic b-wave amplitude also showed moderate attenuation with EZ shortening, with a correlation of 0.64 ($p<0.001$). Finally, the 30Hz flicker peak amplitude was also moderately attenuated with EZ shortening, with a corelation of 0.57 ($p<0.001$). The complete summary of correlations for EZ and ffERG, including latencies, can be found in the Appendix as Supplemental Table II.

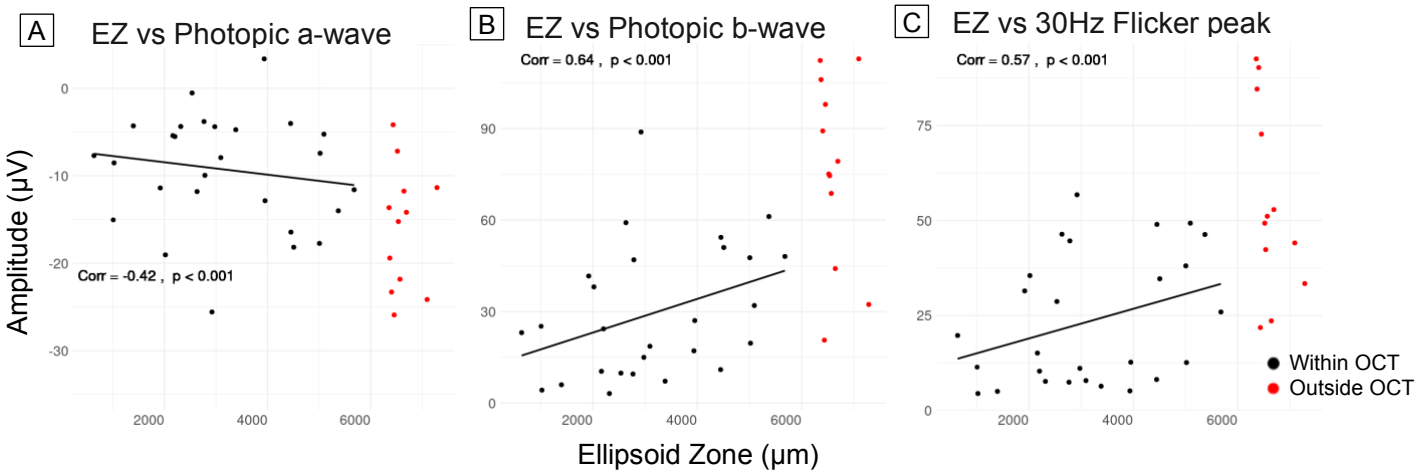

Figure 3.33. Correlation of ellipsoid zone length and cone photoreceptor function tested through various ffERG responses for patients with retinitis pigmentosa. Scatterplots show ellipsoid zone length and ffERG cone-mediated amplitude readings taken within 3 months of one another. A solid black line depicts the relationship between the diagnostic tests. Red points represent EZ lengths extending beyond the OCT limits and are not included in the correlation. (A) a-wave amplitude, r=-0.42 ($p < 0.05$). (B) b-wave amplitude, r=0.64 ($p < 0.001$). (C) 30Hz flicker peak amplitude, r=0.57 ($p < 0.001$). µV = microvolts. µm = micrometres.

3.5.2.3 Relationship of total photoreceptor function to isopter constriction

This analysis is comprised of 21 patients who underwent both a GVF and ffERG test within 3 months of one another. As there are 5 isopter sizes and 19 ffERG responses (for a total of 95 correlations), this section highlights the most significant correlation for each isopter (Figure 3.34). V4e not found to be significantly correlated to any variables. III4e was only significantly correlated to the photopic a-wave amplitude, with a coefficient of -0.50 ($p<0.01$). Out of 13 significant responses each, I4e, 13e and 12e were all most correlated with the scotopic 3.0 cd·s/m^2 a-wave amplitude, with a coefficient of -0.72 ($p<0.001$), -0.63 ($p<0.001$) and -0.61 ($p<0.001$), respectively. A complete summary of correlations for GVF and ffERG can be found in the Appendix as Supplemental Table V.

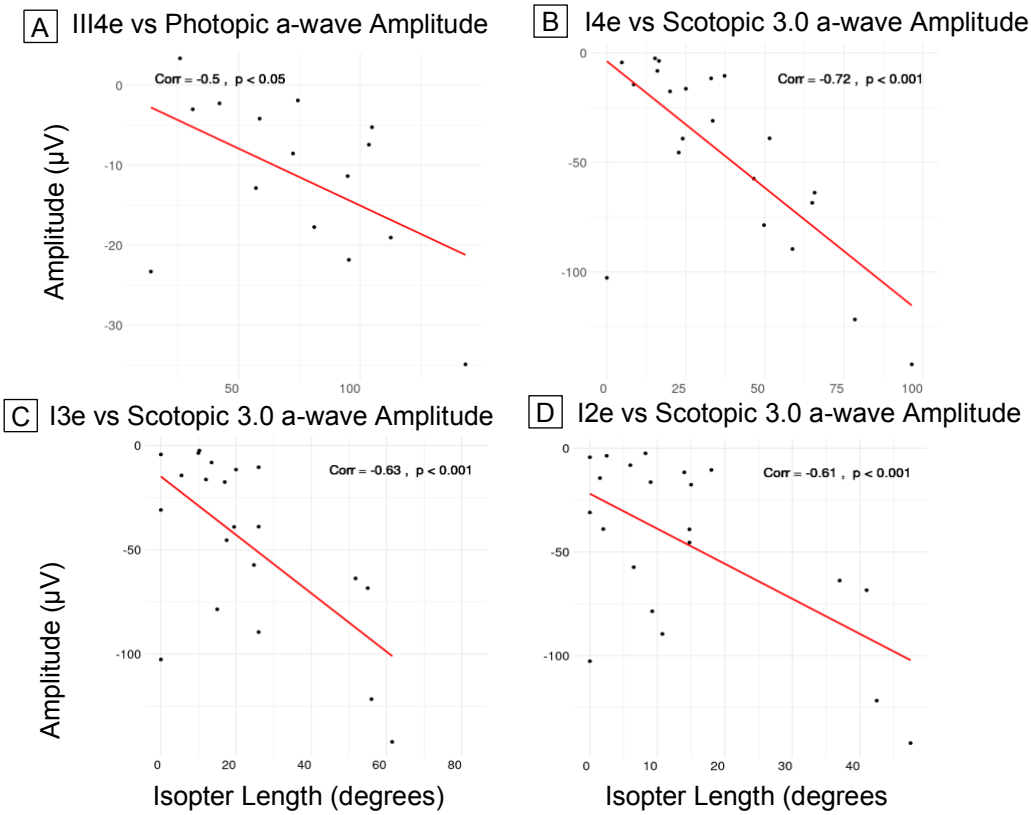

Figure 3.34. Correlation of Goldmann isopters and full-field ERG responses patients with retinitis pigmentosa. Scatterplots show each Goldmann isopter and its most correlated ffERG reading. Measurements were taken within 3 months of one another. A solid red line depicts the relationship between the diagnostic tests. (A) III4e and photopic a-wave amplitude; r=-0.50 ($p<0.05$). (C) I4e and scotopic 3.0 cd·s/m^2 a-wave amplitude, r=-0.72 ($p<0.001$). (C) I3e and scotopic 3.0 cd·s/m^2 a-wave amplitude, r=-0.63 ($p<0.001$). (D) I2e and scotopic 3.0 cd·s/m^2 a-wave amplitude, r=-0.61 ($p<0.001$). µV = microvolts. dB = decibels.

Chapter 4 Discussion

4.1 Discussion of results

In this dissertation, I analysed multimodal progression of retinitis pigmentosa (RP). Although several studies have examined changes in structure and visual function in patients with RP, these studies have typically estimated the rates of change for one or two measures of visual function. This is the first study which examines five modalities to characterise the structural and functional course of a pan-genomic RP cohort. This study aims to inform a clinical trial protocol testing XIAP gene therapy as well as participant inclusion and exclusion criteria. Clinical trial participants will likely comprise a subset of patients from this same cohort, making the study results directly relevant to the trial recruitment. The parameters analysed in this study included one structural: ellipsoid zone length, and four functional: visual field mean deviation, visual field isopter lengths, and multi-focal and full-field electroretinography amplitude and latencies. The data distribution pertaining to each of these parameters reveals that 75% of our cohort has progressed to a stage of RP where remaining photoreceptors are primarily within the central 30° of the retinal field. Given that the macula, which exclusively hosts cone photoreceptors, constitutes the central 5° and the fovea (highest concentration of cones) is the central 1° of the retina (Olman, 2022), this indicates that the majority of the Ottawa Eye Institute RP population has less than 25° of retina with functional rod photoreceptors. This ring is also the location of the highest density of rod photoreceptors (Curcio et al., 1990). Therefore, I suggest that changes in central retinal function may be more indicative of overall photoreceptor health and function in retinitis pigmentosa.

When disease progression is highly symmetrical in the left and right eyes, as we have found in our cohort for each diagnostic modality with correlations between 0.663-0.981, investigators conducting gene therapy and cell-based treatment trials in RP can

utilise the advantage of using the fellow eye as a treatment control (Bainbridge et al., 2008; Massof et al., 1979; Testa et al., 2013). In previous studies, a small proportion of the patients were observed to have baseline asymmetry using OCT structural imaging techniques (Sayaka Aizawa et al., 2010; Fakin et al., 2012; Marsiglia et al., 2012; Sujirakul, Davis, et al., 2015). In this study, only one patient's (1.17%) ellipsoid zone length was found to be significantly asymmetric at baseline with a 1045.64 μm difference (20.97%). In general, RP has been assumed to be bilateral and highly symmetric due to its genetic aetiology (Massof et al., 1979), and asymmetrical disease progression is infrequently described in typical retinitis pigmentosa patients.

This 10-year longitudinal analysis demonstrates that structural measurements of disease progression, particularly ellipsoid zone line width from SD-OCT, is a reliable measure for detecting short-term progression in moderate-advanced RP. OCT offers an objective assessment of retinal layer conditions and was shown to be reproducible with high inter-reader correlation, indicating minimal variance irrespective of the observer. Compared to functional assessments, structural imaging modalities have lower test-retest variability, and hence improved sensitivity to detect the progression of advanced-stage disease in a shorter period of time (Birch et al., 2013; Michael F. Marmor, 2002; R. Ramachandran et al., 2013; Seiple et al., 2004; Sujirakul, Davis, et al., 2015). As such, these imaging modalities are more useful for visualizing the natural course of disease in a slow-progressing disease like RP. The methods in this study differ from previous studies which examined horizontal linear EZ width (Cai et al., 2014) or EZ width and area from en-face OCT images (Hariri et al., 2016). In contrast to these methods, this study obtained exact EZ band length measurements by tracing the counter of the ellipsoid zone band from its nasal to temporal limits. The overall mean rate of ellipsoid zone shortening was found to be 195.05 μm per year or 7.65% per year. Although different statistical

methods have been employed in a variety of published studies monitoring annual changes in functional and structural loss in RP patients, our results approximate previous findings which reported yearly shortening of the ellipsoid zone (Cabral et al., 2017; Hariri et al., 2016; Sujirakul, Lin, et al., 2015). It is important to note that few if any studies examined ellipsoid zone progression in a genetically heterogenous group. Inheritance-specific studies showed approximate annual progression rates of 3-6% for autosomal dominant RP (Cai et al., 2014; Sujirakul, Lin, et al., 2015), 5-7% for autosomal recessive (V. K. L. Takahashi et al., 2018; V. K. L. Takahashi, Xu, et al., 2019), and 7-9% for X-linked RP (Birch et al., 2013). From the genetic inheritance data available in this study cohort, we observed a significant difference of structural progression between autosomal recessive (6.01%/year) and autosomal dominant RP (4.75%/year) groups, similar to previously reported mean annual rates. Progression rates also significantly differ when assessed as a function of initial structural measurement. Ellipsoid zone shortens significantly faster when baseline measurement is ≥ 3000 μm, at a rate of 322.62 μm per year or by 10.20%, and slows down when baseline measurement is < 3000 μm, shortening at a rate of 102.51 μm per year or by 5.28%, This is consistent with the fact that the natural history of RP progresses in an exponential decay (Eliot L. Berson, 2007) and has been observed in a previous study (Cabral et al., 2017). Given this, investigators need to be aware of these factors when designing interventional trials and evaluating efficacy. Despite an overall non-linear pattern of progression, linear modelling would be appropriate for approximating short intervals such as two or three years (Sujirakul, Lin, et al., 2015). Ultimately, investigators can expect EZ length losses of 4.75 – 10.2% per year, depending on stage of disease and mode of inheritance.

Although functional tests, such as visual fields and ERGs, may appear subsidiary for tracking disease progression compared to objective structural measurements, they are

still necessary to represent a patient's functional experience through these outcomes and they most closely capture the patient's perception of visual impairment. Automated perimetry using a Humphrey Visual Field Analyzer remains the simplest, most convenient, and least invasive functional test for patients to undertake. Large changes in visual function determined under consistent testing environments may prove significant as an outcome measure in clinical trials (Bittner et al., 2011; Kiser et al., 2005). Amongst the three testing strategies, which examine either 30° (30-2), 24° (24-2), or 10° (10-2) of the visual field, the majority of previous studies have elected to use only the 10-2 program (Fujiwara et al., 2020, 2018; Hirakawa et al., 1999; Iijima, 2012; Ito et al., 2022; Nakazawa et al., 2011). While some chose to do this to specifically examine cone photoreceptor function, others have argued that the central 10° field could provide more information, especially in patients with advanced disease, because those who tend to show absolute scotomas at most of the tested points in the 24-2 or 30-2 program with 0 dB of sensitivity show measurable and meaningful values at most tested points in the 10-2 program. While this would be advantageous in determining the progression of the disease from a statistical standpoint, a patient with less than 10° of functional visual field might not be a good candidate for a gene therapy trial. Not only would the potential for significant visual improvement be diminished compared to a patient with a larger functional visual field, but patients with very limited remaining vision may be less willing to accept the potential risks associated with the experimental treatment, especially if the likelihood of substantial visual benefit is low. These studies have reported MD rates of change of −0.37, -0.89, and -0.47 dB/year. In this study, 10-2 similarly progresses at a rate of 0.40 dB a year or 1.57% but is slower compared to 24-2 which declines by 0.93 dB a year (4.29%) and 30-2 which declines by 1.03 dB a year (6.35%).

As OCT and HVF are limited to the central 30°, Goldmann visual field and full-field ERG are the only diagnostic tests able to quantify peripheral retinal function in early-stage disease. Up to now, limited studies have assessed the rate of decline in GVF in patients with RP, especially for the III4e and I4e targets. Most studies measured only one single target V4e (Eliot L. Berson et al., 2002; Hafler et al., 2016; Holopigian et al., 1996; Pearlman, 1979; Michael A. Sandberg et al., 2007, 2008; Talib et al., 2017), had short follow-up times (Edwards et al., 1998; Alessandro Iannaccone et al., 2004; Nowomiejska et al., 2016), or evaluated GVF patterns/types (Gerald A. Fishman et al., 2007; S. Grover et al., 1997, 1998; Sadeghi et al., 2006). The methods in this study differ from most previous studies which examine isopter area, either via modern digital kinetic perimetry devices such as Haag-Streit's Octopus 900 or by obtaining the physical visual field sheet and using Photoshop with the method described by Zahid et al (Zahid et al., 2014). At the time of writing, no studies have examined I3e or I2e isopters. For reasons described in section 2.4.2.2, a novel methodology was proposed. The horizontal (nasal-temporal) length of each isopter, via the centremost meridian (through the fovea), was calculated. As the ellipsoid zone measurements came from this same meridian, it was hypothesized that isopter lengths could potentially serve as a complementary pseudo-structural measurement. This resulted in annual declines of 5.22%, 7.77%, 6.77%, 6.80%, and 12.45% for targets V4e, III4e, I4e, I3e, and I2e, respectively. The results of V4e agree with previous findings for the target V4e, with mean annual rate of declines reported to be 4.6% (E. L. Berson et al., 1985), 12% (Holopigian et al., 1996), 6.9% (Hafler et al., 2016) and 5% (Talib et al., 2017). Limited literature has been published regarding the rate of progression for the targets III4e and I4e in RP. Studies for the III4e target reported rates of 14.5% and 10.70% (Ditta Nagy et al., 2008; M. Xu et al., 2020), whereas the rate in our patients (7.77%) was slightly lower. Studies for the I4e target

reported rates of 12.50%, a half-life of 4 years (corresponding to 16% decline annually), and a decline of 13% in I4e area during a 2-year period which corresponds to a 6.7% decline per year, matching this study's findings. These results indicate that visual fields deteriorate at a faster rate for smaller targets than bigger ones, which agrees with the observation that RP begins as a relative scotoma (loss of sensitivity) which gradually deepens with decreasing photoreceptor density before becoming an absolute scotoma (loss of function). Most notably, the I2e target shows the highest rate of progression (12.45%). As the limits of I2e normally fall between 40-50° from the fovea, this once again could be attributed to the higher density of photoreceptors in this region. This suggests that the I2e stimulus is the most sensitive to subtle changes in photoreceptor loss. However, it is important to consider the human factor with this perimetric method. The inter-technician variability was found to be 21.52%, whereas the test-retest variability with a single operator was 12.62%. Previous studies found that test–retest variability ranged up to 20% across most RP patients tested with V4e and III4e targets (Bittner et al., 2011), and was 12% on average for normal subjects and up to 50% in a group of RP subjects (Ross et al., 1984).

ERGs, both multi-focal and full-field, remain useful for providing an objective visual function prognosis in patients with RP. For example, it is estimated that less than 0.5 μV seen on a 30 Hz-flicker ERG can be considered 'virtual blindness' (Eliot L. Berson, 2007). Voltages measured on 30 Hz-flicker can be used to estimate years left of useful vision, information which is invaluable for patient counselling (Eliot L. Berson, 2007). However, previous ERG studies revealed a limitation of ERG in that it is not able to reliably detect small progression, especially in advanced stages of disease, owing to the variability of the testing results and even up to 10-15% variability due to electrode placement (Birch et al., 1999; S. Grover et al., 1997; Holopigian et al., 1996).

Furthermore, as retinal function in patients with moderate disease is often reduced more than 90%, it can be difficult to obtain residual retinal responses. This was also found to be the case in this study, as only a limited number of patients had repeated ERG exams. Although progression of ERG responses did not have statistical significance, graphical representation of the data showed that rod-mediated visual function declines more rapidly than cone-mediated functions, supporting the generally held view for RP. Previous larger-scale studies showed that for patients with RP, the mean annual attenuation of rod ERG was 28% per year compared to 13% per year for cone ERG. Several attempts have been made to measure the residual response in patients with markedly reduced retinal function (Denier Van Der Gon et al., 1956; M. A. Sandberg et al., 1996; Sieving et al., 1998). The 30Hz flicker ERG has been suggested for monitoring these patients (E. L. Berson, 1993), as it has been reported to decline by 13.3% per year (Birch et al., 1999). Small remaining responses could also be measured with mfERG. The yearly progression for mfERG responses was found to be approximately 6% to 10% in the outer three rings (Ditta Nagy et al., 2008). This suggests that cone and mixed rod-cone responses would give more information on remaining visual function for patients with advanced RP.

There has been relatively little research conducted on the agreement between structural and functional diagnostic modalities for RP. Many studies have discussed the relationship between visual acuity (BCVA) and other parameters, namely central retinal thickness (Kim et al., 2013; Michael A. Sandberg et al., 2005), ellipsoid zone length (S. Aizawa et al., 2009; Konieczka et al., 2016; Sousa et al., 2019), and full-field ERG (Fahle et al., 1991). Other studies have investigated the correlation between structural changes on OCT, such as receptor layer thickness (Apushkin et al., 2007; Donald C. Hood et al., 2011), outer segment (Fischer et al., 2008; Rangaswamy et al., 2010), and ellipsoid zone (Donald C. Hood et al., 2011; Yokochi et al., 2012) on visual field constriction. This is

the first study which comprehensively assesses the relationships between ellipsoid zone length, mean deviation, Goldmann isopter length, and full-field and multi-focal electroretinography, for a total of 272 correlations. This study places greater emphasis on structural-functional correlations, but some functional-functional correlations were examined. For structural-functional correlation, the ellipsoid zone had a moderate to high positive correlation with mean deviation from all three testing strategies (30-2 r=0.63, 24-2 r=0.99, and 10-2 r=0.63). Correlation was highest with 24-2, likely since the 30-2 strategy includes high peripheral variability due to low visual sensitivity and patient fatigue (as the outer points are the last ones to be tested) (Ruia & Tripathy, 2023). Although previous studies favour the 10-2, the majority of mean deviation values were between -25 and -35 dB for this study cohort, which, in combination with having the slowest progression rate (0.40 dB a year), reduces its utility as an efficacy endpoint. Ellipsoid zone had a low correlation of 0.31 with Goldmann isopter V4e but a moderate positive correlation with isopters III4e, I4e, I3e, and I2e with correlations of 0.69, 0.50, 0.52, and 0.56, respectively. It was thought that perhaps the limits of the ellipsoid zone would correspond to the borders of an absolute scotoma, which would be identified by V4e. These results suggest that perhaps loss of the ellipsoid zone band signal on OCT does not indicate a total loss of photoreceptor cells. Reflectivity may be lost when cells become limited or cell integrity/organisation is compromised past a threshold, leading to poor backscattering. As such, III4e, I4e, I3e and I2e may be more sensitive to this change. Ellipsoid zone was also moderately positively correlated with mfERG P1 amplitude per unit area by 0.73 in ring 1, 0.79 in ring 2, and 0.47 in ring 3, but had a low correlation of 0.20 in ring 4 and 0.32 in ring 5. The higher correlation with rings 1, 2 and 3 are likely attributed to its spatial alignment with areas of highest photoreceptor densities, where ring 1 and 2 represents the 1–5° field densest in cones and ring 3

represents the 5–10° field denser in rods. Ellipsoid zone showed a neutral correlation with rod-mediated scotopic 0.01 a-wave (r=-0.01), and low correlation with scotopic 0.01 b-wave (r=0.41), 3.0 a-wave (r=-0.37), 3.0 b-wave (r=0.47), 10.0 a-wave (r=-0.31) and 10.0 b-wave (r=0.40). As the 0.01 illumination is extinguished in early stages of RP, changes in amplitude in advanced disease are minimal. Ellipsoid zone showed a low correlation with cone-mediated photopic a-wave (r=-0.42), but a moderate correlation with 0.01 b-wave (r=0.62), 3.0 a-wave (r=-0.61), 3.0 b-wave (r=0.65), 10.0 a-wave (r=-0.61) and 10.0 b-wave (r=0.63). The stronger relationship between the ellipsoid zone length and photopic amplitudes compared to scotopic amplitudes suggests that changes within the central 6000 μm of ellipsoid zone may have a slightly stronger association with cone photoreceptor function than rod photoreceptor function. Between functional tests, mean deviation and P1 amplitude per unit area from mfERG showed a number of moderate positive correlations. Testing strategy 30-2 was only correlated with ring 3 (r=0.74), whereas 24-2 was correlated with rings 2 (r=0.61), 3 (r=0.74), 4 (r=0.72) and 5 (r=0.61). As rings 2-5 represent the 2-25° field and the 24-2 protocol tests the central 24°, the values are highly complementary. Goldmann isopter constriction was also correlated with P1 amplitude per unit area within the 60° field, and a moderate positive correlation was found only with isopters I3e and 12e, particularly for rings 4 (r=0.52 and r=0.68) and 5 (r=0.65 and r=0.74). As mfERG responses are mainly cone-driven, it follows that isopters I3e and I2e, the most sensitive stimuli, will be first impacted by central photoreceptor function. Finally, Goldmann isopter constriction was correlated with total photoreceptor health. Notably, isopters I4e, I3e and I2e all showed a moderate negative correlation with the scotopic 3.0 a-wave amplitude (r=-0.72, r=-0.63, and r=-0.61, respectively). This suggests that Goldmann visual field could offer valuable insight into rod function from a less time-consuming and intensive testing approach, ideal as a repeated efficacy measure.

In summary, this study reveals that the strongest structural-functional relationship for patients with retinitis pigmentosa is that of the ellipsoid zone length and automated visual field 24-2 mean deviation with a coefficient of 0.99 and lends promise for the prospective utility of Goldman visual field as an ERG-alternative measure of rod function.

4.2 Limitations

This study has several limitations. First, the study is retrospective, and each patient was examined by different technicians with various training and experience at baseline and follow-ups. These factors resulted in inter-examiner variability, thus reducing our ability to detect the difference in VF progression among different targets and inheritance patterns. Second, although the size of the cohort (n = 85) made this a larger-scale study relative to some previous RP studies, the number of patients with repeated measurements was variable between diagnostic modalities and small for functional tests (n=3-11). With only one patient for some inheritance patterns (X-linked and mitochondrial), and a small intersection of patients with both a confirmed genetic result and repeated diagnostic testing, it was difficult to perform a stratified analysis for each genetic form. Thirdly, selection bias was inevitable because only those who could test for the various functional tests proceeded to get one. However, this aligns with the target population of a clinical trial, which necessitates a minimum level of vision and capability to undergo diagnostic testing. Extending on this, undercoverage bias or imbalance of data between diagnostic tests was also observed. Eligible candidates, despite being able to undergo certain functional tests, did not receive them possibly due to varying screening protocols across subspecialty clinics or specific directives from ophthalmologists for differential diagnosis. In this case, the central limit theorem was applied under the assumption that the sample size for each diagnostic modality constituted a random sample from the

broader RP population. Lastly, although it was considered appropriate to maintain the logarithmic dB scale for calculating progression rate of mean deviation, a study by Liebmann et el. has pointed out that the rate of progression is underestimated in early stages and overestimated in severe stages when measuring glaucoma progression on a logarithmic scale (Liebmann et al., 2017). Had the values been converted to a linear scale (1/Lambert), the results might be different. There are also limitations to the ellipsoid line shortening method. It requires that the patients have discernible EZ bands within the scan area. Current OCT technology restricts the scans to the central 30° of retina, and as such the disease can only be monitored when it has already reached the macular region. This precludes the tracking of patients with less advanced disease, which accounted for 10 (11.76%) patients in the study.

4.3 Meaningful efficacy measures for a clinical trial

An early-phase gene therapy clinical trial should primarily establish safety of the therapeutic agent (which would be delivered by the subretinal route) and secondarily determine if there is preliminary evidence of efficacy. The initial plan would be to treat a relatively large region of central retina involving not only the cone-rich fovea but also the surrounding rod-rich retina. The analyses of function and structure in the current cohort of RP patients lead to suggestions for what parameters could be used to determine criteria for early and later cohorts and how to monitor them for efficacy. The ideal patient population will depend on whether the study's primary endpoint is safety alone or both safety and efficacy. For safety alone, a diagnosis of RP and stable health are adequate criteria, irrespective of disease severity. For a study assessing both safety and efficacy, the following specific inclusion and exclusion criteria are suggested. Beginning with structural criteria, the ideal candidate would have less than 30° but more than 5° of

ellipsoid zone, which translates to a length between 6000 and 1000 μm (based on an approximation where 6000 μm/60° = 100 μm/1°) on the optical coherence tomography from the foveal b-scan. The results of the study indicate that ellipsoid zone band shortening would serve as a reliable and objective short-term measure. Complementary functional tests would include a Humphrey visual field 24-2 testing strategy, multifocal electroretinogram, and Goldmann isopters I4e, I3e, and I2e. The 24-2 testing strategy is proven to provide information comparable to that provided by the wider 30-2 strategy in a shorter time and with less variability (Khoury et al., 1999). Moreover, the 24-2 showed the most and highest correlations with mfERG ring P1 amplitudes compared to 30-2. Given the advanced stage of RP when reduced to the central 30°, the mfERG offers a sensitive means of simultaneously quantifying rod and cone photoreceptor function within this region. Furthermore, it is better correlated to both the ellipsoid zone length and 24-2 mean deviation compared to the full-field electroretinogram. As a measure of peripheral function, the smaller and dimmer Goldmann isopters I4e, I3e and I2e are well correlated to rod photoreceptor function and have the highest correlations with the outer rings of mfERG compared to other diagnostic measures. Although not analysed in this study, studies have demonstrated that the rate of hyperautofluorescent ring constriction is both correlated with ellipsoid length from all angles and visual field loss progression, and has prognostic value in predicting visual field acuity and visual field preservation (Robson et al., 2008). This may be useful alongside functional assessments as the outcome measurements for future therapeutic trials. Altogether, the ellipsoid zone band, 24-2 mean deviation, multi-focal ERG and Goldman isopters I4e, I3e, and I2e would form a well-complemented and robust clinical trial protocol to assess therapeutic efficacy. A baseline first visit could include a ffERG and fundus photograph for documentation purposes. Genetic testing to confirm the candidate's inheritance pattern is

recommended to guide the investigator's expectations for progression timeline. To minimise test-retest variability, the first OCT should be set as the reference scan from which follow-up scans can be locked into the same exact position. As well, the same ophthalmic technician should be maintained for all Goldmann visual field testing. Exclusion criteria includes patients unable to complete the diagnostic tests described or those with concurrent secondary conditions affecting the central vision or retinal layers, such as central macular oedema, retinal detachment, untreated cataracts, and similar pathologies. Based on the results reported here and the average duration of a combined Phase 1/2 clinical trial being 3 years (Suvarna, 2010; Wouters et al., 2020), a follow-up period of 3 years should be sufficient to assess the efficacy of the gene therapy with 6-month intervals to detect progression.

4.4 Conclusions

This thesis has addressed each of the four study aims. (1) The bulk of the results section looked at multimodal structural and functional progression rates as well as correlations between them. (2) The ideal diagnostic procedures for assessing short term disease progression have been determined as ellipsoid zone length on optical coherence tomography, the 24-2 SITA Standard Humphrey visual field exam, Goldmans visual field with particular emphasis on stimulus sizes 14e, 13e and 12e, and multi-focal electroretinography. (3) The consistent changes observed over time has determined that the average three-year Phase I/II trial timeline with 6-month intervals is sufficient for disease progression and to determine efficacy of the gene therapy. (4) We have also determined the appropriate criteria for including and excluding candidates, identifying an ideal participant as a retinitis pigmentosa patient with between 30° and 5° of structural and functional retina, capable of undergoing multiple diagnostic assessments consistently and reliably, with diagnostic outputs unaffected by concurrent central retinal pathologies.

Bibliography

Acland, G. M., Aguirre, G. D., Ray, J., Zhang, Q., Aleman, T. S., Cideciyan, A. V., Pearce-Kelling, S. E., Anand, V., Zeng, Y., Maguire, A. M., Jacobson, S. G., Hauswirth, W. W., & Bennett, J. (2001). Gene therapy restores vision in a canine model of childhood blindness. *Nature Genetics*, *28*(1), 92–95. https://doi.org/10.1038/ng0501-92

Adler, R. (1996). Mechanisms of photoreceptor death in retinal degenerations. From the cell biology of the 1990s to the ophthalmology of the 21st century? *Archives of Ophthalmology*, *114*(1), 79–83. https://doi.org/10.1001/archopht.1996.01100130075012

Aizawa, S., Mitamura, Y., Baba, T., Hagiwara, A., Ogata, K., & Yamamoto, S. (2009). Correlation between visual function and photoreceptor inner/outer segment junction in patients with retinitis pigmentosa. *Eye*, *23*(2), 304–308. https://doi.org/10.1038/sj.eye.6703076

Aizawa, Sayaka, Mitamura, Y., Hagiwara, A., Sugawara, T., & Yamamoto, S. (2010). Changes of fundus autofluorescence, photoreceptor inner and outer segment junction line, and visual function in patients with retinitis pigmentosa. *Clinical & Experimental Ophthalmology*, *38*(6), 597–604. https://doi.org/10.1111/j.1442-9071.2010.02321.x

Aleman, T. S., Duncan, J. L., & Bieber, M. L. (2001). Macular pigment and lutein supplementation in RP and Usher's syndrome Invest Ophthalmol Vis Sci. *Invest Ophthalmol Vis Sci*, *42*, 1873–1881.

Aleman, Tomas S., Cideciyan, A. V., Sumaroka, A., Schwartz, S. B., Roman, A. J., Windsor, E. A. M., Steinberg, J. D., Branham, K., Othman, M., Swaroop, A., & Jacobson, S. G. (2007). Inner retinal abnormalities in X-linked retinitis pigmentosa with RPGR mutations. *Investigative Ophthalmology & Visual Science*, *48*(10), 4759–4765. https://doi.org/10.1167/iovs.07-0453

Anderson, D. R. (1982). *Testing the Field of Vision*. Mosby.

Anderson, D. R., & Patella, V. M. (1998). *Automated Static Perimetry* (2nd ed.). Mosby.

Aonuma, H., Koide, K., Masuda, K., & Watanabe, I. (1997). Retinal light damage: Protective effect of alphatocopherol. *Jpn. J. Ophthalmol*, *41*, 160–167.

Appelbaum, T., Santana, E., & Aguirre, G. D. (2017). Strong upregulation of inflammatory genes accompanies photoreceptor demise in canine models of retinal degeneration. *PloS One*, *12*(5), e0177224. https://doi.org/10.1371/journal.pone.0177224

Apushkin, M. A., Fishman, G. A., Alexander, K. R., & Shahidi, M. (2007). Retinal thickness and visual thresholds measured in patients with retinitis pigmentosa. *Retina (Philadelphia, Pa.)*, *27*(3), 349–357. https://doi.org/10.1097/01.iae.0000224944.33863.18

Aronson, J. K. (2008). Biomarkers and surrogate endpoints in monitoring therapeutic interventions. In *Evidence-based Medical Monitoring* (pp. 48–62). Blackwell Publishing Ltd. https://doi.org/10.1002/9780470696323.ch4

Bahrami, H., Melia, M., & Dagnelie, G. (2006). Lutein supplementation in retinitis pigmentosa: PC-based vision assessment in a randomized double-masked placebo-controlled clinical trial [NCT00029289]. *BMC Ophthalmology*, *6*(1), 23. https://doi.org/10.1186/1471-2415-6-23

Bainbridge, J. W. B., Smith, A. J., Barker, S. S., Robbie, S., Henderson, R., Balaggan, K., Viswanathan, A., Holder, G. E., Stockman, A., Tyler, N., Petersen-Jones, S., Bhattacharya, S. S., Thrasher, A. J., Fitzke, F. W., Carter, B. J., Rubin, G. S.,

Moore, A. T., & Ali, R. R. (2008). Effect of gene therapy on visual function in Leber's congenital amaurosis. *The New England Journal of Medicine*, *358*(21), 2231–2239. https://doi.org/10.1056/NEJMoa0802268

Battu, R., Khanna, A., Hegde, B., Berendschot, T. T. J. M., Grover, S., & Schouten, J. S. A. G. (2015). Correlation of structure and function of the macula in patients with retinitis pigmentosa. *Eye*, *29*(7), 895–901. https://doi.org/10.1038/eye.2015.61

Beck, R. W., Maguire, M. G., Bressler, N. M., Glassman, A. R., Lindblad, A. S., & Ferris, F. L. (2007). Visual acuity as an outcome measure in clinical trials of retinal diseases. *Ophthalmology*, *114*(10), 1804–1809. https://doi.org/10.1016/j.ophtha.2007.06.047

Berson, E. L. (1993). Retinitis pigmentosa. The friedenwald lecture. *Investigative Ophthalmology & Visual Science*, *34*(5), 1659–1676. https://www.ncbi.nlm.nih.gov/pubmed/8473105

Berson, E. L., Sandberg, M. A., Rosner, B., Birch, D. G., & Hanson, A. H. (1985). Natural course of retinitis pigmentosa over a three-year interval. *American Journal of Ophthalmology*, *99*(3), 240–251. https://doi.org/10.1016/0002-9394(85)90351-4

Berson, Eliot L. (2007). Long-term visual prognoses in patients with retinitis pigmentosa: The Ludwig von Sallmann lecture. *Experimental Eye Research*, *85*(1), 7–14. https://doi.org/10.1016/j.exer.2007.03.001

Berson, Eliot L. (2008). Retinitis Pigmentosa and Allied Diseases. In *Albert & Jakobiec's Principles & Practice of Ophthalmology* (pp. 2225–2252). Elsevier. https://doi.org/10.1016/b978-1-4160-0016-7.50180-6

Berson, Eliot L., Rosner, B., Weigel-DiFranco, C., Dryja, T. P., & Sandberg, M. A. (2002). Disease progression in patients with dominant retinitis pigmentosa and rhodopsin mutations. *Investigative Ophthalmology & Visual Science*, *43*(9), 3027–3036. https://www.ncbi.nlm.nih.gov/pubmed/12202526

Biomarkers Definitions Working Group. (2001). Biomarkers and surrogate endpoints: preferred definitions and conceptual framework. *Clinical Pharmacology and Therapeutics*, *69*(3), 89–95. https://doi.org/10.1067/mcp.2001.113989

Birch, D. G., Anderson, J. L., & Fish, G. E. (1999). Yearly rates of rod and cone functional loss in retinitis pigmentosa and cone-rod dystrophy11The authors have no financial interest in any aspect of this study. *Ophthalmology*, *106*(2), 258–268. https://doi.org/10.1016/s0161-6420(99)90064-7

Birch, D. G., Hood, D. C., Locke, K. G., Hoffman, D. R., & Tzekov, R. T. (2002). Quantitative electroretinogram measures of phototransduction in cone and rod photoreceptors: normal aging, progression with disease, and test-retest variability. *Archives of Ophthalmology*, *120*(8), 1045–1051. https://doi.org/10.1001/archopht.120.8.1045

Birch, D. G., Locke, K. G., Wen, Y., Locke, K. I., Hoffman, D. R., & Hood, D. C. (2013). Spectral-domain optical coherence tomography measures of outer segment layer progression in patients with X-linked retinitis pigmentosa. *JAMA Ophthalmology*, *131*(9), 1143–1150. https://doi.org/10.1001/jamaophthalmol.2013.4160

Bittner, A. K., Iftikhar, M. H., & Dagnelie, G. (2011). Test-retest, within-visit variability of Goldmann visual fields in retinitis pigmentosa. *Investigative Ophthalmology & Visual Science*, *52*(11), 8042–8046. https://doi.org/10.1167/iovs.11-8321

Bittner, A. K., Rosenfarb, A., Gould, J., & Dagnelie, G. (2015). Response to Re: A pilot study of an acupuncture protocol to improve visual function in retinitis pigmentosa patients [Review of *Response to Re: A pilot study of an acupuncture*

protocol to improve visual function in retinitis pigmentosa patients]. *Clinical & Experimental Optometry: Journal of the Australian Optometrical Association*, *98*(1), 100. Informa UK Limited. https://doi.org/10.1111/cxo.12243

Boon, C. J. F., & Wijnholds, J. (2018). *Retinal gene therapy : methods and protocols* (C. J. F. Boon & J. Wijnholds, Eds.). Humana Press.

Branham, K., Schlegel, D., Fahim, A. T., & Jayasundera, K. T. (2020). Genetic testing for inherited retinal degenerations: Triumphs and tribulations. *American Journal of Medical Genetics. Part C, Seminars in Medical Genetics*, *184*(3), 571–577. https://doi.org/10.1002/ajmg.c.31835

Brown, D. M., Michels, M., Kaiser, P. K., Heier, J. S., Sy, J. P., Ianchulev, T., & ANCHOR Study Group. (2009). Ranibizumab versus verteporfin photodynamic therapy for neovascular age-related macular degeneration: Two-year results of the ANCHOR study. *Ophthalmology*, *116*(1), 57-65.e5. https://doi.org/10.1016/j.ophtha.2008.10.018

Bunker, C. H., Berson, E. L., Bromley, W. C., Hayes, R. P., & Roderick, T. H. (1984). Prevalence of retinitis pigmentosa in Maine. *American Journal of Ophthalmology*, *97*(3), 357–365. https://doi.org/10.1016/0002-9394(84)90636-6

Busskamp, V., & Roska, B. (2011). Optogenetic approaches to restoring visual function in retinitis pigmentosa. *Current Opinion in Neurobiology*, *21*(6), 942–946. https://doi.org/10.1016/j.conb.2011.06.001

Cabral, T., Sengillo, J. D., Duong, J. K., Justus, S., Boudreault, K., Schuerch, K., Belfort, R., Jr, Mahajan, V. B., Sparrow, J. R., & Tsang, S. H. (2017). Retrospective analysis of structural disease progression in retinitis pigmentosa utilizing multimodal imaging. *Scientific Reports*, *7*(1), 10347. https://doi.org/10.1038/s41598-017-10473-0

Cai, C. X., Locke, K. G., Ramachandran, R., Birch, D. G., & Hood, D. C. (2014). A comparison of progressive loss of the ellipsoid zone (EZ) band in autosomal dominant and x-linked retinitis pigmentosa. *Investigative Ophthalmology & Visual Science*, *55*(11), 7417–7422. https://doi.org/10.1167/iovs.14-15013

Calzetti, G., Levy, R. A., Cideciyan, A. V., Garafalo, A. V., Roman, A. J., Sumaroka, A., Charng, J., Heon, E., & Jacobson, S. G. (2018). Efficacy outcome measures for clinical trials of USH2A caused by the common c.2299delG mutation. *American Journal of Ophthalmology*, *193*, 114–129. https://doi.org/10.1016/j.ajo.2018.06.017

Carmody, R. J., McGowan, A. J., & Cotter, T. G. (1998). Rapid detection of rod photoreceptor apoptosis by flow cytometry. *Cytometry*, *33*(1), 89–92. https://doi.org/10.1002/(sici)1097-0320(19980901)33:1<89::aid-cyto11>3.0.co;2-s

Cassin, B. (1995). *Fundamentals for ophthalmic technical personnel* (L. M. Hamed, Ed.). W B Saunders.

Cehajic-Kapetanovic, J., Xue, K., Martinez-Fernandez de la Camara, C., Nanda, A., Davies, A., Wood, L. J., Salvetti, A. P., Fischer, M. D., Aylward, J. W., Barnard, A. R., Jolly, J. K., Luo, E., Lujan, B. J., Ong, T., Girach, A., Black, G. C. M., Gregori, N. Z., Davis, J. L., Rosa, P. R., … MacLaren, R. E. (2020). Initial results from a first-in-human gene therapy trial on X-linked retinitis pigmentosa caused by mutations in RPGR. *Nature Medicine*, *26*(3), 354–359. https://doi.org/10.1038/s41591-020-0763-1

Chai, J., Shiozaki, E., Srinivasula, S. M., Wu, Q., Datta, P., Alnemri, E. S., & Shi, Y. (2001). Structural basis of caspase-7 inhibition by XIAP. *Cell*, *104*(5), 769–780. https://doi.org/10.1016/s0092-8674(01)00272-0

Chan, D. K., Lieberman, D. M., Musatov, S., Goldfein, J. A., Selesnick, S. H., & Kaplitt, M. G. (2007). Protection against cisplatin-induced ototoxicity by adeno-associated virus-mediated delivery of the X-linked inhibitor of apoptosis protein is not dependent on caspase inhibition. *Otology & Neurotology*, *28*(3), 417–425. https://doi.org/10.1097/01.mao.0000247826.28893.7a

Chew, E. Y., Clemons, T. E., Jaffe, G. J., Johnson, C. A., Farsiu, S., Lad, E. M., Guymer, R., Rosenfeld, P., Hubschman, J.-P., Constable, I., Wiley, H., Singerman, L. J., Gillies, M., Comer, G., Blodi, B., Eliott, D., Yan, J., Bird, A., Friedlander, M., & Macular Telangiectasia Type 2-Phase 2 CNTF Research Group. (2019). Effect of ciliary neurotrophic factor on retinal neurodegeneration in patients with macular telangiectasia type 2: A randomized clinical trial. *Ophthalmology*, *126*(4), 540–549. https://doi.org/10.1016/j.ophtha.2018.09.041

Chirieleison, S. M., Marsh, R. A., Kumar, P., Rathkey, J. K., Dubyak, G. R., & Abbott, D. W. (2017). Nucleotide-binding oligomerization domain (NOD) signaling defects and cell death susceptibility cannot be uncoupled in X-linked inhibitor of apoptosis (XIAP)-driven inflammatory disease. *The Journal of Biological Chemistry*, *292*(23), 9666–9679. https://doi.org/10.1074/jbc.M117.781500

Clemson, C. M., Tzekov, R., Krebs, M., Checchi, J. M., Bigelow, C., & Kaushal, S. (2011). Therapeutic potential of valproic acid for retinitis pigmentosa. *The British Journal of Ophthalmology*, *95*(1), 89–93. https://doi.org/10.1136/bjo.2009.175356

Cooper, L. B., Chan, D. K., Roediger, F. C., Shaffer, B. R., Fraser, J. F., Musatov, S., Selesnick, S. H., & Kaplitt, M. G. (2006). AAV-mediated delivery of the caspase inhibitor XIAP protects against cisplatin ototoxicity. *Otology & Neurotology*, *27*(4), 484–490. https://doi.org/10.1097/01.mao.0000202647.19355.6a

Crocker, S. J., Liston, P., Anisman, H., Lee, C. J., Smith, P. D., Earl, N., Thompson, C. S., Park, D. S., Korneluk, R. G., & Robertson, G. S. (2003). Attenuation of MPTP-induced neurotoxicity and behavioural impairment in NSE-XIAP transgenic mice. *Neurobiology of Disease*, *12*(2), 150–161. https://doi.org/10.1016/s0969-9961(02)00020-7

Csaky, K., Ferris, F., 3rd, Chew, E. Y., Nair, P., Cheetham, J. K., & Duncan, J. L. (2017). Report from the NEI/FDA endpoints workshop on age-related macular degeneration and inherited retinal diseases. *Investigative Ophthalmology & Visual Science*, *58*(9), 3456–3463. https://doi.org/10.1167/iovs.17-22339

Curcio, C. A., Sloan, K. R., Kalina, R. E., & Hendrickson, A. E. (1990). Human photoreceptor topography. *Journal of Comparative Neurology*, *292*, 497–523.

Dacruz, L., Bf, C., & Dorn, J. (2013). The Argus II epiretinal prosthesis system allows letter and word reading and long-term function in patients with profound vision loss. *Br J Ophthalmol*, *97*, 632–636.

Dagnelie, G. (1990a). Conversion of planimetric visual field data into solid angles and retinal areas. *Clin Vis Sci*, *5*, 95–100.

Dagnelie, G. (1990b). Technical note. conversion of planimetric visual field data into solid angles and retinal areas. *Vis Res*, *5*, 95–100.

Daiger, S. P., Sullivan, L. S., & Bowne, S. J. (2013). Genes and mutations causing retinitis pigmentosa. *Clinical Genetics*, *84*(2), 132–141. https://doi.org/10.1111/cge.12203

Daiger, Stephen P. (2022, October 7). *RetNet: Summaries of Genes and Loci Causing Retinal Disease*. UTHealth Houston School of Public Health. https://web.sph.uth.edu/RetNet/sum-dis.htm?csrt=13212204437533106747#A-genes

Dejneka, N. S., & Bennett, J. (2001). Gene therapy and retinitis pigmentosa: advances and future challenges. *BioEssays: News and Reviews in Molecular, Cellular and Developmental Biology*, *23*(7), 662–668. https://doi.org/10.1002/bies.1092

Delori, F. C., Dorey, C. K., Staurenghi, G., Arend, O., Goger, D. G., & Weiter, J. J. (1995). In vivo fluorescence of the ocular fundus exhibits retinal pigment epithelium lipofuscin characteristics. *Investigative Ophthalmology & Visual Science*, *36*(3), 718–729. https://www.ncbi.nlm.nih.gov/pubmed/7890502

Denier Van Der Gon, J. J., Henkes, H. E., & Van Der Tweel, L. H. (1956). Selective amplification of the electroretinogram. *Ophthalmologica. Journal International d'ophtalmologie. International Journal of Ophthalmology. Zeitschrift Für Augenheilkunde*, *132*(3), 140–150. https://doi.org/10.1159/000302942

Dersu, I., Wiggins, M., Luther, A., Harper, R., & Chacko, J. (2006). Understanding visual fields, Part I; Goldmann perimetry. *J Ophthalmic Med Technol*, *2*, 438–440.

Dimopoulos, I. S., Tseng, C., & MacDonald, I. M. (2016). Microperimetry as an outcome measure in choroideremia trials: Reproducibility and beyond. *Investigative Ophthalmology & Visual Science*, *57*(10), 4151–4161. https://doi.org/10.1167/iovs.16-19338

Donders, F. C. (1857). Beiträge zur pathologischen Anatomie des Auges. *Albrecht von Graefes Archiv für Ophthalmologie*, *3*(1), 139–165. https://doi.org/10.1007/bf02720685

Duncker, T., Tabacaru, M. R., Lee, W., Tsang, S. H., Sparrow, J. R., & Greenstein, V. C. (2013). Comparison of near-infrared and short-wavelength autofluorescence in retinitis pigmentosa. *Investigative Ophthalmology & Visual Science*, *54*(1), 585–591. https://doi.org/10.1167/iovs.12-11176

Eberhardt, O., Coelln, R. V., Kugler, S., Lindenau, J., Rathke-Hartlieb, S., Gerhardt, E., Haid, S., Isenmann, S., Gravel, C., Srinivasan, A., Bahr, M., Weller, M., Dichgans, J., & Schulz, J. B. (2000). Protection by synergistic effects of adenovirus-mediated X-chromosome-linked inhibitor of apoptosis and glial cell line-derived neurotrophic factor gene transfer in the 1-methyl-4-phenyl-1,2,3,6-tetrahydropyridine model of Parkinson's disease. *The Journal of Neuroscience: The Official Journal of the Society for Neuroscience*, *20*(24), 9126–9134. https://doi.org/10.1523/jneurosci.20-24-09126.2000

Edwards, A., Fishman, G. A., Anderson, R. J., Grover, S., & Derlacki, D. J. (1998). Visual acuity and visual field impairment in Usher syndrome. *Archives of Ophthalmology*, *116*(2), 165–168. https://doi.org/10.1001/archopht.116.2.165

El-Hifnawi, E., Hettlich, H.-J., & Falk, C. (1995). Retinal degeneration in rats induced by vitamin E deficiency. In *Degenerative Diseases of the Retina* (pp. 111–118). Springer US. https://doi.org/10.1007/978-1-4615-1897-6_13

Elmore, S. (2007). Apoptosis: a review of programmed cell death. *Toxicologic Pathology*, *35*(4), 495–516. https://doi.org/10.1080/01926230701320337

Fahle, M., Steuhl, K. P., & Aulhorn, E. (1991). Correlations between electroretinography, morphology and function in retinitis pigmentosa. *Graefe s Archive for Clinical and Experimental Ophthalmology*, *229*(1), 37–49. https://doi.org/10.1007/bf00172259

Fakin, A., Jarc-Vidmar, M., Glavač, D., Bonnet, C., Petit, C., & Hawlina, M. (2012). Fundus autofluorescence and optical coherence tomography in relation to visual function in Usher syndrome type 1 and 2. *Vision Research*, *75*, 60–70. https://doi.org/10.1016/j.visres.2012.08.017

Falsini, B., Iarossi, G., Chiaretti, A., Ruggiero, A., Manni, L., Galli-Resta, L., Corbo, G., & Abed, E. (2016). NGF eye-drops topical administration in patients with retinitis

pigmentosa, a pilot study. *Journal of Translational Medicine*, *14*(1). https://doi.org/10.1186/s12967-015-0750-3

Feeney-Burns, L., Berman, E. R., & Rothman, H. (1980). Lipofuscin of human retinal pigment epithelium. *American Journal of Ophthalmology*, *90*(6), 783–791. https://doi.org/10.1016/s0002-9394(14)75193-1

Ferris, F. L., Podgor, M. J., Davis, M. D., & Group, D. R. (1987). Macular edema in diabetic retinopathy study patients: diabetic retinopathy study report number 12. *Ophthalmology*, *7*, 754–760.

Fischer, M. D., Fleischhauer, J. C., Gillies, M. C., Sutter, F. K., Helbig, H., & Barthelmes, D. (2008). A new method to monitor visual field defects caused by photoreceptor degeneration by quantitative optical coherence tomography. *Investigative Ophthalmology & Visual Science*, *49*(8), 3617–3621. https://doi.org/10.1167/iovs.08-2003

Fishman, G. A., Anderson, R. J., & Lourenco, P. (1985). Prevalence of posterior subcapsular lens opacities in patients with retinitis pigmentosa. *The British Journal of Ophthalmology*, *69*(4), 263–266. https://doi.org/10.1136/bjo.69.4.263

Fishman, G. A., Chappelw, A. V., & Anderson, R. J. (2005). Short term inter-visit variability of ERG amplitudes in normal subjects and patients with retinitis pigmentosa. *Retina*, *25*(8), 1014–1021.

Fishman, Gerald A., Bozbeyoglu, S., Massof, R. W., & Kimberling, W. (2007). Natural course of visual field loss in patients with Type 2 Usher syndrome. *Retina (Philadelphia, Pa.)*, *27*(5), 601–608. https://doi.org/10.1097/01.iae.0000246675.88911.2c

Frasson, M., Sahel, J. A., & Fabre, M. (1999). RP: Rod photoreceptor rescue by a calcium channel blocker in the rd mouse. *Nature Medicine*, *5*.

Fujimoto, J. G., Pitris, C., Boppart, S. A., & Brezinski, M. E. (2000). Optical coherence tomography: an emerging technology for biomedical imaging and optical biopsy. *Neoplasia (New York, N.Y.)*, *2*(1–2), 9–25. https://doi.org/10.1038/sj.neo.7900071

Fujiwara, K., Ikeda, Y., Murakami, Y., Tachibana, T., Funatsu, J., Koyanagi, Y., Nakatake, S., Shimokawa, S., Yoshida, N., Nakao, S., Hisatomi, T., Ishibashi, T., & Sonoda, K.-H. (2020). Aqueous flare and progression of visual field loss in patients with retinitis pigmentosa. *Investigative Ophthalmology & Visual Science*, *61*(8), 26. https://doi.org/10.1167/iovs.61.8.26

Fujiwara, K., Ikeda, Y., Murakami, Y., Tachibana, T., Funatsu, J., Koyanagi, Y., Nakatake, S., Yoshida, N., Nakao, S., Hisatomi, T., Yoshida, S., Yoshitomi, T., Ishibashi, T., & Sonoda, K.-H. (2018). Assessment of central visual function in patients with retinitis pigmentosa. *Scientific Reports*, *8*(1), 8070. https://doi.org/10.1038/s41598-018-26231-9

Ghazi, N. G., Abboud, E. B., Nowilaty, S. R., Alkuraya, H., Alhommadi, A., Cai, H., Hou, R., Deng, W.-T., Boye, S. L., Almaghamsi, A., Al Saikhan, F., Al-Dhibi, H., Birch, D., Chung, C., Colak, D., LaVail, M. M., Vollrath, D., Erger, K., Wang, W., … Alkuraya, F. S. (2016). Treatment of retinitis pigmentosa due to MERTK mutations by ocular subretinal injection of adeno-associated virus gene vector: results of a phase I trial. *Human Genetics*, *135*(3), 327–343. https://doi.org/10.1007/s00439-016-1637-y

Gonin, J. (1901). Le scotome annulaire dans la degenerescence pigmentaire de la retine. *Ocul*, *125*, 101–130.

Gouras, P., & Carr, R. E. (1964). Electrophysiological studies in early retinitis pigmentosa. *Archives of Ophthalmology*, *72*(1), 104–110. https://doi.org/10.1001/archopht.1964.00970020106022

Green, E. S., Menz, M. D., LaVail, M. M., & Flannery, J. G. (2000). Characterization of rhodopsin mis-sorting and constitutive activation in a transgenic rat model of retinitis pigmentosa. *Investigative Ophthalmology & Visual Science*, *41*(6), 1546–1553. https://www.ncbi.nlm.nih.gov/pubmed/10798675

Grøndahl, J. (2008). Estimation of prognosis and prevalence of retinitis pigmentosa and Usher syndrome in Norway. *Clinical Genetics*, *31*(4), 255–264. https://doi.org/10.1111/j.1399-0004.1987.tb02804.x

Grover, S., Fishman, G. A., Anderson, R. J., Alexander, K. R., & Derlacki, D. J. (1997). Rate of visual field loss in retinitis pigmentosa. *Ophthalmology*, *104*(3), 460–465. https://doi.org/10.1016/s0161-6420(97)30291-7

Grover, S., Fishman, G. A., & Brown, J., Jr. (1998). Patterns of visual field progression in patients with retinitis pigmentosa. *Ophthalmology*, *105*(6), 1069–1075. https://doi.org/10.1016/S0161-6420(98)96009-2

Grover, Sandeep, Fishman, G. A., Birch, D. G., Locke, K. G., & Rosner, B. (2003). Variability of full-field electroretinogram responses in subjects without diffuse photoreceptor cell disease. *Ophthalmology*, *110*(6), 1159–1163. https://doi.org/10.1016/S0161-6420(03)00253-7

Grunwald, J. E., Maguire, A. M., & Dupont, J. (1996). Retinal hemodynamics in retinitis pigmentosa. *American Journal of Ophthalmology*, *122*(4), 502–508. https://doi.org/10.1016/s0002-9394(14)72109-9

Hafezi, F., Steinbach, J. P., Marti, A., Munz, K., Wang, Z. Q., Wagner, E. F., Aguzzi, A., & Remé, C. E. (1997). The absence of c-fos prevents light-induced apoptotic cell death of photoreceptors in retinal degeneration in vivo. *Nature Medicine*, *3*(3), 346–349. https://doi.org/10.1038/nm0397-346

Hafler, B. P., Comander, J., Weigel DiFranco, C., Place, E. M., & Pierce, E. A. (2016). Course of ocular function in PRPF31 retinitis pigmentosa. *Seminars in Ophthalmology*, *31*(1–2), 49–52. https://doi.org/10.3109/08820538.2015.1114856

Hagiwara, A., Yamamoto, S., Ogata, K., Sugawara, T., Hiramatsu, A., Shibata, M., & Mitamura, Y. (2011). Macular abnormalities in patients with retinitis pigmentosa: prevalence on OCT examination and outcomes of vitreoretinal surgery. *Acta Ophthalmologica*, *89*(2), e122-5. https://doi.org/10.1111/j.1755-3768.2010.01866.x

Hamel, C. (2006). Retinitis pigmentosa. *Orphanet Journal of Rare Diseases*, *1*(1), 40. https://doi.org/10.1186/1750-1172-1-40

Hariri, A. H., Zhang, H. Y., Ho, A., Francis, P., Weleber, R. G., Birch, D. G., Ferris, F. L., III, Sadda, S. R., & for the Trial of Oral Valproic Acid for Retinitis Pigmentosa Group. (2016). Quantification of ellipsoid zone changes in retinitis pigmentosa using en face spectral domain–optical coherence tomography. *JAMA Ophthalmology*, *134*(6), 628. https://doi.org/10.1001/jamaophthalmol.2016.0502

He, Y., Zhang, Y., Liu, X., Ghazaryan, E., Li, Y., Xie, J., & Su, G. (2014). Recent advances of stem cell therapy for retinitis pigmentosa. *International Journal of Molecular Sciences*, *15*(8), 14456–14474. https://doi.org/10.3390/ijms150814456

Heier, J. S., Brown, D. M., Chong, V., Korobelnik, J. F., Kaiser, P. K., & Nguyen, Q. D. (2012). VIEW 1 and VIEW 2 Study Groups Intravitreal aflibercept (VEGF trap-eye) in wet age-related macular degeneration. *Ophthalmology*, *12*, 2537–2548.

Hirakawa, H., Iijima, H., Gohdo, T., Imai, M., & Tsukahara, S. (1999). Progression of defects in the central 10-degree visual field of patients with retinitis pigmentosa and choroideremia. *American Journal of Ophthalmology*, *127*(4), 436–442. https://doi.org/10.1016/s0002-9394(98)00408-5

Holopigian, K., Greenstein, V., Seiple, W., & Carr, R. E. (1996). Rates of change differ among measures of visual function in patients with retinitis pigmentosa. *Ophthalmology*, *103*(3), 398–405. https://doi.org/10.1016/s0161-6420(96)30679-9

Hood, D. C., Holopigian, K., Greenstein, V., Seiple, W., Li, J., Sutter, E. E., & Carr, R. E. (1998). Assessment of local retinal function in patients with retinitis pigmentosa using the multi-focal ERG technique. *Vision Research*, *38*(1), 163–179. https://doi.org/10.1016/s0042-6989(97)00143-0

Hood, Donald C., Lin, C. E., Lazow, M. A., Locke, K. G., Zhang, X., & Birch, D. G. (2009). Thickness of receptor and post-receptor retinal layers in patients with retinitis pigmentosa measured with frequency-domain optical coherence tomography. *Investigative Ophthalmology & Visual Science*, *50*(5), 2328–2336. https://doi.org/10.1167/iovs.08-2936

Hood, Donald C., Ramachandran, R., Holopigian, K., Lazow, M., Birch, D. G., & Greenstein, V. C. (2011). Method for deriving visual field boundaries from OCT scans of patients with retinitis pigmentosa. *Biomedical Optics Express*, *2*(5), 1106–1114. https://doi.org/10.1364/BOE.2.001106

Huang, D., Swanson, E. A., Lin, C. P., Schuman, J. S., Stinson, W. G., Chang, W., Hee, M. R., Flotte, T., Gregory, K., Puliafito, C. A., & Fujimoto, J. G. (1991). Optical coherence tomography. *Science (New York, N.Y.)*, *254*(5035), 1178–1181. https://doi.org/10.1126/science.1957169

Huang, H., Chen, Y., Chen, H., Ma, Y., Chiang, P.-W., Zhong, J., Liu, X., Asan, Wu, J., Su, Y., Li, X., Deng, J., Huang, Y., Zhang, X., Li, Y., Fan, N., Wang, Y., Tang, L., Shen, J., … Yi, X. (2018). Systematic evaluation of a targeted gene capture sequencing panel for molecular diagnosis of retinitis pigmentosa. *PloS One*, *13*(4), e0185237. https://doi.org/10.1371/journal.pone.0185237

Huang, Y., Park, Y. C., Rich, R. L., Segal, D., Myszka, D. G., & Wu, H. (2001). Structural basis of caspase inhibition by XIAP: differential roles of the linker versus the BIR domain. *Cell*, *104*(5), 781–790. https://doi.org/10.1016/s0092-8674(02)02075-5

Humayun, M. S., Dorn, J. D., da Cruz, L., Dagnelie, G., Sahel, J.-A., Stanga, P. E., Cideciyan, A. V., Duncan, J. L., Eliott, D., Filley, E., Ho, A. C., Santos, A., Safran, A. B., Arditi, A., Del Priore, L. V., Greenberg, R. J., & Argus II Study Group. (2012). Interim results from the international trial of Second Sight's visual prosthesis. *Ophthalmology*, *119*(4), 779–788. https://doi.org/10.1016/j.ophtha.2011.09.028

Iannaccone, A. (2004). Kinetics of visual field loss in Usher syndrome Type II. *Invest Ophthalmol Vis Sci*, *45*, 784–792.

Iannaccone, Alessandro, Kritchevsky, S. B., Ciccarelli, M. L., Tedesco, S. A., Macaluso, C., Kimberling, W. J., & Somes, G. W. (2004). Kinetics of visual field loss in Usher syndrome Type II. *Investigative Ophthalmology & Visual Science*, *45*(3), 784–792. https://doi.org/10.1167/iovs.03-0906

Iijima, H. (2012). Correlation between visual sensitivity loss and years affected for eyes with retinitis pigmentosa. *Japanese Journal of Ophthalmology*, *56*(3), 224–229. https://doi.org/10.1007/s10384-012-0135-6

Ilhan, C., & Citirik, M. (2019). Glial proliferation and atrophy: Two poles of optic disc in patients with retinitis pigmentosa. *Journal of Current Ophthalmology*, *31*(4), 416–421. https://doi.org/10.1016/j.joco.2019.08.002

Illing, M. E., Rajan, R. S., Bence, N. F., & Kopito, R. R. (2002). A rhodopsin mutant linked to autosomal dominant retinitis pigmentosa is prone to aggregate and

interacts with the ubiquitin proteasome system. *The Journal of Biological Chemistry*, *277*(37), 34150–34160. https://doi.org/10.1074/jbc.M204955200

Imre, G., Larisch, S., & Rajalingam, K. (2011). Ripoptosome: a novel IAP-regulated cell death-signalling platform. *Journal of Molecular Cell Biology*, *3*(6), 324–326. https://doi.org/10.1093/jmcb/mjr034

Ito, N., Miura, G., Shiko, Y., Kawasaki, Y., Baba, T., & Yamamoto, S. (2022). Progression rate of visual function and affecting factors at different stages of retinitis pigmentosa. *BioMed Research International*, *2022*, 1–8. https://doi.org/10.1155/2022/7204954

Ivandic, B. T., & Ivandic, T. (2014). Low-level laser therapy improves vision in a patient with retinitis pigmentosa. *Photomedicine and Laser Surgery*, *32*(3), 181–184. https://doi.org/10.1089/pho.2013.3535

Jacobson, S. G., Sumaroka, A., Luo, X., & Cideciyan, A. V. (2013). Retinal optogenetic therapies: clinical criteria for candidacy. *Clinical Genetics*, *84*(2), 175–182. https://doi.org/10.1111/cge.12165

Jacobson, Samuel G., Cideciyan, A. V., Ho, A. C., Peshenko, I. V., Garafalo, A. V., Roman, A. J., Sumaroka, A., Wu, V., Krishnan, A. K., Sheplock, R., Boye, S. L., Dizhoor, A. M., & Boye, S. E. (2021). Safety and improved efficacy signals following gene therapy in childhood blindness caused by GUCY2D mutations. *IScience*, *24*(5), 102409. https://doi.org/10.1016/j.isci.2021.102409

Jaffal, L., Mrad, Z., Ibrahim, M., Salami, A., Audo, I., Zeitz, C., & El Shamieh, S. (2022). The research output of rod-cone dystrophy genetics. *Orphanet Journal of Rare Diseases*, *17*(1), 175. https://doi.org/10.1186/s13023-022-02318-5

Janáky, M., Goupland, S. G., & Benedek, G. (1996). Human oscillatory potentials: components of rod origin. *Ophthalmologica. Journal International d'ophtalmologie. International Journal of Ophthalmology. Zeitschrift Für Augenheilkunde*, *210*(6), 315–318. https://doi.org/10.1159/000310731

Jimenez-Davila, H. J., Klufas, M. A., & Yonekawa, Y. (2022, February 10). *A Review of Retinitis Pigmentosa*. https://www.reviewofophthalmology.com/article/a-review-of-retinitis-pigmentosa

Johnson, C. A., Wall, M., & Thompson, H. S. (2011). A history of perimetry and visual field testing. *Optometry and Vision Science: Official Publication of the American Academy of Optometry*, *88*(1), E8-15. https://doi.org/10.1097/OPX.0b013e3182004c3b

Khoury, J. M., Donahue, S. P., Lavin, P. J., & Tsai, J. C. (1999). Comparison of 24-2 and 30-2 perimetry in glaucomatous and nonglaucomatous optic neuropathies. *Journal of Neuro-Ophthalmology: The Official Journal of the North American Neuro-Ophthalmology Society*, *19*(2), 100–108. https://doi.org/10.1097/00041327-199906000-00004

Kim, Y. J., Joe, S. G., Lee, D.-H., Lee, J. Y., Kim, J.-G., & Yoon, Y. H. (2013). Correlations between spectral-domain OCT measurements and visual acuity in cystoid macular edema associated with retinitis pigmentosa. *Investigative Ophthalmology & Visual Science*, *54*(2), 1303–1309. https://doi.org/10.1167/iovs.12-10149

Kiser, A. K., Mladenovich, D., Eshraghi, F., Bourdeau, D., & Dagnelie, G. (2005). Reliability and consistency of visual acuity and contrast sensitivity measures in advanced eye disease. *Optometry and Vision Science: Official Publication of the American Academy of Optometry*, *82*(11), 946–954. https://doi.org/10.1097/01.opx.0000187863.12609.7b

Kitiratschky, V., Stingl, K., & Wilhelm, B. (2014). Safety evaluation of "retina implant alpha IMS"-a prospective clinical trial. *Graefes Arch Clin Exp Ophthalmol*, *253*(3), 381–387.

Kiuchi, K., Yoshizawa, K., Shikata, N., Matsumura, M., & Tsubura, A. (2002). Nicotinamide prevents N-methyl-N-nitrosourea-induced photoreceptor cell apoptosis in Sprague-Dawley rats and C57BL mice. *Experimental Eye Research*, *74*(3), 383–392. https://doi.org/10.1006/exer.2001.1127

Koenekoop, R. K., Sui, R., Sallum, J., van den Born, L. I., Ajlan, R., Khan, A., den Hollander, A. I., Cremers, F. P. M., Mendola, J. D., Bittner, A. K., Dagnelie, G., Schuchard, R. A., & Saperstein, D. A. (2014). Oral 9-cis retinoid for childhood blindness due to Leber congenital amaurosis caused by RPE65 or LRAT mutations: an open-label phase 1b trial. *Lancet*, *384*(9953), 1513–1520. https://doi.org/10.1016/S0140-6736(14)60153-7

Kolb, H., Nelson, R. F., Ahnelt, P. K., Ortuño-Lizarán, I., & Cuenca, N. (2020). *The architecture of the human fovea*. University of Utah Health Sciences Center. https://www.ncbi.nlm.nih.gov/books/NBK554706/

Konieczka, K., Bojinova, R. I., Valmaggia, C., Schorderet, D. F., Todorova, M. G., & Medscape. (2016). Preserved functional and structural integrity of the papillomacular area correlates with better visual acuity in retinitis pigmentosa. *Eye*, *30*(10), 1310–1323. https://doi.org/10.1038/eye.2016.136

Lam, B. L. (2005). *Electrophysiology of vision* (B. L. Lam, Ed.). CRC Press.

Leonard, K. C., Petrin, D., Coupland, S. G., Baker, A. N., Leonard, B. C., LaCasse, E. C., Hauswirth, W. W., Korneluk, R. G., & Tsilfidis, C. (2007). XIAP protection of photoreceptors in animal models of retinitis pigmentosa. *PloS One*, *2*(3), e314. https://doi.org/10.1371/journal.pone.0000314

Lesmes, L. A., Jackson, M. L., & Bex, P. (2013). Visual function endpoints to enable dry AMD clinical trials. *Drug Discovery Today. Therapeutic Strategies*, *10*(1), e43–e50. https://doi.org/10.1016/j.ddstr.2012.11.002

Léveillard, T., Fridlich, R., & Clérin, E. (2014). Therapeutic strategy for handling inherited retinal degenerations in a gene-independent manner using rod- derived cone viability factors. *C R Biol*, *337*(3), 207–213.

Léveillard, T., Mohand-Saïd, S., & Lorentz, O. (2004). Identification and characterization of rod-derived cone viability factor. *Nat Genet*, *36*, 755–759.

Li, T., Sandberg, M. A., Pawlyk, B. S., Rosner, B., Hayes, K. C., Dryja, T. P., & Berson, E. L. (1998). Effect of vitamin A supplementation on rhodopsin mutants threonine-17 --> methionine and proline-347 --> serine in transgenic mice and in cell cultures. *Proceedings of the National Academy of Sciences of the United States of America*, *95*(20), 11933–11938. https://doi.org/10.1073/pnas.95.20.11933

Li, X.-X., & Yuan, N. (1990). Measurement of the oscillatory potentials of the electroretinogram in the domains of frequency and time. *Documenta Ophthalmologica. Advances in Ophthalmology*, *76*(1), 65–71. https://doi.org/10.1007/bf00140499

Liebmann, K., De Moraes, C. G., & Liebmann, J. M. (2017). Measuring rates of visual field progression in linear versus nonlinear scales: Implications for understanding the relationship between baseline damage and target rates of glaucoma progression. *Journal of Glaucoma*, *26*(8), 721–725. https://doi.org/10.1097/ijg.0000000000000710

Lima, L. H., Burke, T., Greenstein, V. C., Chou, C. L., Cella, W., Yannuzzi, L. A., & Tsang, S. H. (2012). Progressive constriction of the hyperautofluorescent ring in

retinitis pigmentosa. *American Journal of Ophthalmology*, *153*(4), 718–727, 727.e1-2. https://doi.org/10.1016/j.ajo.2011.08.043

Lujan, B. J., Roorda, A., Knighton, R. W., & Carroll, J. (2011). Revealing Henle's fiber layer using spectral domain optical coherence tomography. *Investigative Ophthalmology & Visual Science*, *52*(3), 1486–1492. https://doi.org/10.1167/iovs.10-5946

Luthert, P. J., & Chong, N. H. (1998). Photoreceptor rescue. *Eye*, *12 (Pt 3b)*(3), 591–596. https://doi.org/10.1038/eye.1998.149

Ma, J., Fan, N., & Wang, N. (2019). Normal Visual Field. In *Advances in Visual Science and Eye Diseases* (pp. 43–48). Springer Singapore. https://doi.org/10.1007/978-981-13-2502-1_9

Mahroo, O. A. (2023). Visual electrophysiology and "the potential of the potentials." *Eye*, *37*(12), 2399–2408. https://doi.org/10.1038/s41433-023-02491-2

Maiti, A., Uparkar, M., Natarajan, S., Borse, N., & Walinjkar, J. (2011). Principal components′ analysis of multifocal electroretinogram in retinitis pigmentosa. *Indian Journal of Ophthalmology*, *59*(5), 353. https://doi.org/10.4103/0301-4738.83610

Marmor, M. F. (1999). Zrenner E (for the International Society for 604. Clinical Electrophysiology of Vision): Standard for Clinical Electroretinography (1999 Update). *Doc Ophthalmol*, *97*, 143–156.

Marmor, M. F., & Zrenner, E. (1998). Standard for clinical electroretinography (1999 update). International Society for Clinical Electrophysiology of Vision. *Documenta Ophthalmologica. Advances in Ophthalmology*, *97*(2), 143–156. https://www.ncbi.nlm.nih.gov/pubmed/10765968

Marmor, Michael F. (2002). Do you, doctor, take the mfERG.for better or for worse? [Review of *Do you, doctor, take the mfERG.for better or for worse?*]. *Graefe s Archive for Clinical and Experimental Ophthalmology*, *240*(4), 241–243. Springer Science and Business Media LLC. https://doi.org/10.1007/s00417-002-0438-2

Marmor, Michael F., Hood, D. C., Keating, D., Kondo, M., Seeliger, M. W., Miyake, Y., & International Society for Clinical Electrophysiology of Vision. (2003). Guidelines for basic multifocal electroretinography (mfERG). *Documenta Ophthalmologica. Advances in Ophthalmology*, *106*(2), 105–115. https://doi.org/10.1023/a:1022591317907

Marsiglia, M., Duncker, T., Peiretti, E., Brodie, S. E., & Tsang, S. H. (2012). Unilateral retinitis pigmentosa: a proposal of genetic pathogenic mechanisms. *European Journal of Ophthalmology*, *22*(4), 654–660. https://doi.org/10.5301/ejo.5000086

Massof, R. W., Dagnelie, G., & Benzschawel, T. (1990). First order dynamics of visual field loss in retinitis pigmentosa. *Clin Vision Sci*, *5*, 1–26.

Massof, R. W., Finkelstein, D., Starr, S. J., Kenyon, K. R., Fleischman, J. A., & Maumenee, I. H. (1979). Bilateral symmetry of vision disorders in typical retinitis pigmentosa. *The British Journal of Ophthalmology*, *63*(2), 90–96. https://doi.org/10.1136/bjo.63.2.90

Mcanany et el. (2023, April 12). *Electroretinogram*. AAO EyeWiki. https://eyewiki.aao.org/Electroretinogram

McCulloch, D. L., Marmor, M. F., Brigell, M. G., Hamilton, R., Holder, G. E., Tzekov, R., & Bach, M. (2015). ISCEV Standard for full-field clinical electroretinography (2015 update). *Documenta Ophthalmologica. Advances in Ophthalmology*, *130*(1), 1–12. https://doi.org/10.1007/s10633-014-9473-7

Meinert, C. L. (1986). *Clinical Trials, Design, Conduct, and Analysis*. Oxford University Press.

Menghini, M., Cehajic-Kapetanovic, J., & MacLaren, R. E. (2020). Monitoring progression of retinitis pigmentosa: current recommendations and recent advances. *Expert Opinion on Orphan Drugs*, *8*(2–3), 67–78. https://doi.org/10.1080/21678707.2020.1735352

Michels, R. G., Wilkinson, C. P., Rice, T. A., & Weinberg, A. B. (1991). Retinal detachment. *Retina (Philadelphia, Pa.)*, *11*(4), 450. https://doi.org/10.1097/00006982-199110000-00031

Milam, A. H., Li, Z. Y., & Fariss, R. N. (1998). Histopathology of the human retina in retinitis pigmentosa. *Progress in Retinal and Eye Research*, *17*(2), 175–205. https://doi.org/10.1016/s1350-9462(97)00012-8

Murakami, Y., Ikeda, Y., Nakatake, S., Fujiwara, K., Tachibana, T., Yoshida, N., Notomi, S., Hisatomi, T., Yoshida, S., Ishibashi, T., & Sonoda, K.-H. (2018). C-Reactive protein and progression of vision loss in retinitis pigmentosa. *Acta Ophthalmologica*, *96*(2), e174–e179. https://doi.org/10.1111/aos.13502

Murakami, Y., Yoshida, N., Ikeda, Y., Nakatake, S., Fujiwara, K., Notomi, S., Nabeshima, T., Nakao, S., Hisatomi, T., Enaida, H., & Ishibashi, T. (2015). Relationship between aqueous flare and visual function in retinitis pigmentosa. *American Journal of Ophthalmology*, *159*(5), 958-63.e1. https://doi.org/10.1016/j.ajo.2015.02.001

Nagasaka, Y., Ito, Y., Ueno, S., & Terasaki, H. (2016). Increased aqueous flare is associated with thickening of inner retinal layers in eyes with retinitis pigmentosa. *Scientific Reports*, *6*(1), 33921. https://doi.org/10.1038/srep33921

Nagy, D., Schoönfisch, B., Zrenner, E., & Jägle, H. (2008). Long-term follow-up of retinitis pigmentosa patients with multifocal electroretinography. *Invest Ophthalmol Vis Sci*, *49*, 4664–4671.

Nagy, Ditta, Schönfisch, B., Zrenner, E., & Jägle, H. (2008). Long-term follow-up of retinitis pigmentosa patients with multifocal electroretinography. *Investigative Ophthalmology & Visual Science*, *49*(10), 4664–4671. https://doi.org/10.1167/iovs.07-1360

Nakazawa, M., Ohguro, H., Takeuchi, K., Miyagawa, Y., Ito, T., & Metoki, T. (2011). Effect of nilvadipine on central visual field in retinitis pigmentosa: a 30-month clinical trial. *Ophthalmologica. Journal International d'ophtalmologie. International Journal of Ophthalmology. Zeitschrift Für Augenheilkunde*, *225*(2), 120–126. https://doi.org/10.1159/000320500

Nguyen, X.-T.-A., Moekotte, L., Plomp, A. S., Bergen, A. A., van Genderen, M. M., & Boon, C. J. F. (2023). Retinitis pigmentosa: Current clinical management and emerging therapies. *International Journal of Molecular Sciences*, *24*(8), 7481. https://doi.org/10.3390/ijms24087481

Nickells, R. W., & Zack, D. J. (1996). Apoptosis in ocular disease: a molecular overview. *Ophthalmic Genetics*, *17*(4), 145–165. https://doi.org/10.3109/13816819609057889

Niederhauser, S., & Mojon, D. S. (2002). Normal isopter position in the peripheral visual field in goldmann kinetic perimetry. *Ophthalmologica. Journal International d'ophtalmologie. International Journal of Ophthalmology. Zeitschrift Für Augenheilkunde*, *216*(6), 406–408. https://doi.org/10.1159/000067554

Nowomiejska, K., Brzozowska, A., Koss, M. J., Weleber, R. G., Schiefer, U., Rejdak, K., Juenemann, A. G., Maciejewski, R., & Rejdak, R. (2016). Quantification of the visual field loss in retinitis pigmentosa using semi-automated kinetic perimetry. *Current Eye Research*, *41*(7), 993–998. https://doi.org/10.3109/02713683.2015.1079328

Olman. (2022). Eccentricity. In *Introduction to Sensation and Perception*. University of Minnesota Libraries Publishing. https://pressbooks.umn.edu/sensationandperception/chapter/eccentricity-draft/

O'Neal, T. B., & Luther, E. E. (2023). *Retinitis Pigmentosa*. StatPearls Publishing. https://www.ncbi.nlm.nih.gov/books/NBK519518/

Ontario, H. C. C. (2022, August 6). *Champlain*. Home and Community Care Support Services. https://healthcareathome.ca/region/champlain/

Organisciak, D. T., & Bicknell, I. R. (1992). Darrow The effects of L-and D-ascorbic acid administration on retinal tissue levels and light damage in rats Curr. *Curr Eye Res*, *11*.

Orna, M. V. (1985). Light and color in nature and art, by Samuel J. williamson and Herman Z. cummins, John Wiley and sons, New York, 1983, 488 pp. Price: $30.95. *Color Research and Application*, *10*(2), 123–124. https://doi.org/10.1002/col.5080100214

Osterberg, G. A. (1935). Topography of the layer of the rods and cones in the human retima. *Acta Ophthalmol*, *13*, 1–102.

Oyster, C. W., & Haver, N. (1999). *The human eye: structure and function* (Vol. 1). Sinauer Associates Sunderland.

Pagon, R. A. (1988). Retinitis pigmentosa. *Survey of Ophthalmology*, *33*(3), 137–177. https://doi.org/10.1016/0039-6257(88)90085-9

Park, S. S., Bauer, G., Abedi, M., Pontow, S., Panorgias, A., Jonnal, R., Zawadzki, R. J., Werner, J. S., & Nolta, J. (2014). Intravitreal autologous bone marrow CD34+ cell therapy for ischemic and degenerative retinal disorders: preliminary phase 1 clinical trial findings. *Investigative Ophthalmology & Visual Science*, *56*(1), 81–89. https://doi.org/10.1167/iovs.14-15415

Parmeggiani, F., Sato, G., De Nadai, K., Romano, M. R., Binotto, A., & Costagliola, C. (2011). Clinical and rehabilitative management of retinitis pigmentosa: Up-to-date. *Current Genomics*, *12*(4), 250–259. https://doi.org/10.2174/138920211795860125

Pasantes-Morales, H., Quiroz, H., & Quesada, O. (2002). Treatment with taurine, diltiazem, and vitamin E retards the progressive visual field reduction in retinitis pigmentosa: a 3-year follow-up study. *Metabolic Brain Disease*, *17*(3), 183–197. https://doi.org/10.1023/a:1019926122125

Pawlyk, B. S., Li, T., & Scimeca, M. S. (2002). Absence of photoreceptor rescue with D-cis-diltiazem in the rd mouse Invest Ophthalmol Vis Sci. *Invest Ophthalmol Vis Sci*, *43*, 1912–1915.

Pearlman, J. T. (1979). Mathematical models of retinitis pigmentosa: a study of the rate of progress in the different genetic forms. *Transactions of the American Ophthalmological Society*, *77*, 643–656. https://www.ncbi.nlm.nih.gov/pubmed/317544

Perea-Romero, I., Gordo, G., Iancu, I. F., Del Pozo-Valero, M., Almoguera, B., Blanco-Kelly, F., Carreño, E., Jimenez-Rolando, B., Lopez-Rodriguez, R., Lorda-Sanchez, I., Martin-Merida, I., Pérez de Ayala, L., Riveiro-Alvarez, R., Rodriguez-Pinilla, E., Tahsin-Swafiri, S., Trujillo-Tiebas, M. J., ESRETNET Study Group, ERDC Study Group, Associated Clinical Study Group, … Ayuso, C. (2021). Genetic landscape of 6089 inherited retinal dystrophies affected cases in Spain and their therapeutic and extended epidemiological implications. *Scientific Reports*, *11*(1), 1526. https://doi.org/10.1038/s41598-021-81093-y

Petrin, D., Baker, A., Brousseau, J., Coupland, S., Liston, P., Hauswirth, W. W., Komeluk, R. G., & Tsilfidis, C. (2003). XIAP protects photoreceptors from n-

methyl-n-nitrosourea-induced retinal degeneration. *Advances in Experimental Medicine and Biology*, *533*, 385–393. https://doi.org/10.1007/978-1-4615-0067-4_49

Planul, A., & Dalkara, D. (2017). Vectors and gene delivery to the retina. *Annual Review of Vision Science*, *3*, 121–140. https://doi.org/10.1146/annurev-vision-102016-061413

Portera-Cailliau, C., Sung, C. H., Nathans, J., & Adler, R. (1994). Apoptotic photoreceptor cell death in mouse models of retinitis pigmentosa. *Proceedings of the National Academy of Sciences of the United States of America*, *91*(3), 974–978. https://doi.org/10.1073/pnas.91.3.974

Prado, D. A., Acosta-Acero, M., & Maldonado, R. S. (2020). Gene therapy beyond luxturna: a new horizon of the treatment for inherited retinal disease. *Current Opinion in Ophthalmology*, *31*(3), 147–154. https://doi.org/10.1097/ICU.0000000000000660

Ptito, M., Bleau, M., & Bouskila, J. (2021). The retina: A window into the brain. *Cells (Basel, Switzerland)*, *10*(12), 3269. https://doi.org/10.3390/cells10123269

Punzo, C., Kornacker, K., & Cepko, C. L. (2009). Stimulation of the insulin/mTOR pathway delays cone death in a mouse model of retinitis pigmentosa. *Nature Neuroscience*, *12*(1), 44–52. https://doi.org/10.1038/nn.2234

Racette et. al. (2019). *Visual Field Digest 8th ed.: A guide to perimetry and the Octopus perimeter*. Haag-Streit AG.

Ramachandran, R., Zhou, L., Locke, K. G., Birch, D. G., & Hood, D. C. (2013). *A Comparison of Methods for Tracking Progression in X-Linked Retinitis Pigmentosa Using Frequency Domain OCT. Transl Vis Sci Technol*. *2*.

Ramachandran, Rithambara, Zhou, L., Locke, K. G., Birch, D. G., & Hood, D. C. (2013). A comparison of methods for tracking progression in X-linked retinitis pigmentosa using frequency domain OCT. *Translational Vision Science & Technology*, *2*(7), 5. https://doi.org/10.1167/tvst.2.7.5

Rangaswamy, N. V., Patel, H. M., Locke, K. G., Hood, D. C., & Birch, D. G. (2010). A comparison of visual field sensitivity to photoreceptor thickness in retinitis pigmentosa. *Investigative Ophthalmology & Visual Science*, *51*(8), 4213–4219. https://doi.org/10.1167/iovs.09-4945

Remé, C. E., Grimm, C., Hafezi, F., Marti, A., & Wenzel, A. (1998). Apoptotic cell death in retinal degenerations. *Progress in Retinal and Eye Research*, *17*(4), 443–464. https://doi.org/10.1016/s1350-9462(98)00009-3

Renwick, J., Narang, M. A., Coupland, S. G., Xuan, J. Y., Baker, A. N., Brousseau, J., Petrin, D., Munger, R., Leonard, B. C., Hauswirth, W. W., Korneluk, R. G., & Tsilfidis, C. (2006). XIAP-mediated neuroprotection in retinal ischemia. *Gene Therapy*, *13*(4), 339–347. https://doi.org/10.1038/sj.gt.3302683

Riedl, S. J., Renatus, M., Schwarzenbacher, R., Zhou, Q., Sun, C., Fesik, S. W., Liddington, R. C., & Salvesen, G. S. (2001). Structural basis for the inhibition of caspase-3 by XIAP. *Cell*, *104*(5), 791–800. https://doi.org/10.1016/s0092-8674(01)00274-4

Robson, A. G., Michaelides, M., Saihan, Z., Bird, A. C., Webster, A. R., Moore, A. T., Fitzke, F. W., & Holder, G. E. (2008). Functional characteristics of patients with retinal dystrophy that manifest abnormal parafoveal annuli of high density fundus autofluorescence; a review and update. *Documenta Ophthalmologica. Advances in Ophthalmology*, *116*(2), 79–89. https://doi.org/10.1007/s10633-007-9087-4

Robson, A. G., Nilsson, J., Li, S., Jalali, S., Fulton, A. B., Tormene, A. P., Holder, G. E., & Brodie, S. E. (2018). ISCEV guide to visual electrodiagnostic procedures.

Documenta Ophthalmologica. Advances in Ophthalmology, *136*(1), 1–26. https://doi.org/10.1007/s10633-017-9621-y

Roman, A. J., Cideciyan, A. V., Aleman, T. S., & Jacobson, S. G. (2007). Full-field stimulus testing (FST) to quantify visual perception in severely blind candidates for treatment trials. *Physiological Measurement*, *28*(8), N51-6. https://doi.org/10.1088/0967-3334/28/8/N02

Rosenfeld, P. J., Brown, D. M., Heier, J. S., Boyer, D. S., Kaiser, P. K., & Chung, C. Y. (2006). MARINA Study Group Ranibizumab for neovascular age-related macular degeneration. *N Engl J Med*, *355*(14), 1419–1431.

Ross, D. F., Fishman, G. A., Gilbert, L. D., & Anderson, R. J. (1984). Variability of visual field measurements in normal subjects and patients with retinitis pigmentosa. *Archives of Ophthalmology*, *102*(7), 1004–1010. https://doi.org/10.1001/archopht.1984.01040030806021

Rotenstreich, Y., Belkin, M., Sadetzki, S., Chetrit, A., Ferman-Attar, G., Harari, S. I., Shaish, A., & Harats, A. (2013). Treatment with 9-cis beta-carotene-rich powder in patients with retinitis pigmentosa: a randomized crossover trial. *JAMA Ophthalmol*, *131*, 985–992.

Rousseau, S., & Lachapelle, P. (1999). The electroretinogram recorded at the onset of dark-adaptation: understanding the origin of the scotopic oscillatory potentials. *Documenta Ophthalmologica. Advances in Ophthalmology*, *99*(2), 135–150. https://www.ncbi.nlm.nih.gov/pubmed/11097118

Ruia, S., & Tripathy, K. (2023). *Humphrey Visual Field*. StatPearls Publishing. https://www.ncbi.nlm.nih.gov/books/NBK585112/

Sadeghi, A. M., Eriksson, K., Kimberling, W. J., Sjöström, A., & Möller, C. (2006). Longterm visual prognosis in Usher syndrome types 1 and 2. *Acta Ophthalmologica Scandinavica*, *84*(4), 537–544. https://doi.org/10.1111/j.1600-0420.2006.00675.x

Sahel, J.-A., Boulanger-Scemama, E., Pagot, C., Arleo, A., Galluppi, F., Martel, J. N., Esposti, S. D., Delaux, A., de Saint Aubert, J.-B., de Montleau, C., Gutman, E., Audo, I., Duebel, J., Picaud, S., Dalkara, D., Blouin, L., Taiel, M., & Roska, B. (2021). Partial recovery of visual function in a blind patient after optogenetic therapy. *Nature Medicine*, *27*(7), 1223–1229. https://doi.org/10.1038/s41591-021-01351-4

Sandberg, M. A., Weigel-DiFranco, C., Rosner, B., & Berson, E. L. (1996). The relationship between visual field size and electroretinogram amplitude in retinitis pigmentosa. *Investigative Ophthalmology & Visual Science*, *37*(8), 1693–1698. https://www.ncbi.nlm.nih.gov/pubmed/8675413

Sandberg, Michael A., Brockhurst, R. J., Gaudio, A. R., & Berson, E. L. (2005). The association between visual acuity and central retinal thickness in retinitis pigmentosa. *Investigative Ophthalmology & Visual Science*, *46*(9), 3349–3354. https://doi.org/10.1167/iovs.04-1383

Sandberg, Michael A., Rosner, B., Weigel-DiFranco, C., Dryja, T. P., & Berson, E. L. (2007). Disease course of patients with X-linked retinitis pigmentosa due to RPGR gene mutations. *Investigative Ophthalmology & Visual Science*, *48*(3), 1298–1304. https://doi.org/10.1167/iovs.06-0971

Sandberg, Michael A., Rosner, B., Weigel-DiFranco, C., McGee, T. L., Dryja, T. P., & Berson, E. L. (2008). Disease course in patients with autosomal recessive retinitis pigmentosa due to the USH2A gene. *Investigative Ophthalmology & Visual Science*, *49*(12), 5532–5539. https://doi.org/10.1167/iovs.08-2009

Santos, A., Humayun, M. S., de Juan, E., Jr, Greenburg, R. J., Marsh, M. J., Klock, I. B., & Milam, A. H. (1997). Preservation of the inner retina in retinitis pigmentosa. A morphometric analysis. *Archives of Ophthalmology*, *115*(4), 511–515. https://doi.org/10.1001/archopht.1997.01100150513011

Sato, K., Li, S., Gordon, W. C., He, J., Liou, G. I., Hill, J. M., Travis, G. H., Bazan, N. G., & Jin, M. (2013). Receptor interacting protein kinase-mediated necrosis contributes to cone and rod photoreceptor degeneration in the retina lacking interphotoreceptor retinoid-binding protein. *The Journal of Neuroscience: The Official Journal of the Society for Neuroscience*, *33*(44), 17458–17468. https://doi.org/10.1523/JNEUROSCI.1380-13.2013

Sayo, A., Ueno, S., Kominami, T., Nishida, K., Inooka, D., Nakanishi, A., Yasuda, S., Okado, S., Takahashi, K., Matsui, S., & Terasaki, H. (2017). Longitudinal study of visual field changes determined by Humphrey Field Analyzer 10-2 in patients with Retinitis Pigmentosa. *Scientific Reports*, *7*(1), 16383. https://doi.org/10.1038/s41598-017-16640-7

Schatz, A., Röck, T., & Naycheva, L. (2011). Transcorneal electrical stimulation for patients with retinitis Pigmentosa: a prospective, randomized, sham- controlled exploratory study. *Invest Opthalmol Vis Sci*, *52*(7).

Schatz, Andreas, Röck, T., Naycheva, L., Willmann, G., Wilhelm, B., Peters, T., Bartz-Schmidt, K. U., Zrenner, E., Messias, A., & Gekeler, F. (2011). Transcorneal electrical stimulation for patients with retinitis pigmentosa: a prospective, randomized, sham-controlled exploratory study. *Investigative Ophthalmology & Visual Science*, *52*(7), 4485–4496. https://doi.org/10.1167/iovs.10-6932

Schmitz-Valckenberg, S., Holz, F. G., Bird, A. C., & Spaide, R. F. (2008). Fundus autofluorescence imaging: review and perspectives. *Retina (Philadelphia, Pa.)*, *28*(3), 385–409. https://doi.org/10.1097/IAE.0b013e318164a907

Schroeder, M., & Kjellström, U. (2018). Full-field ERG as a predictor of the natural course of ABCA4-associated retinal degenerations. *Molecular Vision*, *24*, 1–16. https://www.ncbi.nlm.nih.gov/pubmed/29386879

Seeliger, M., Kretschmann, U., Apfelstedt-Sylla, E., Rüther, K., & Zrenner, E. (1998). Multifocal electroretinography in retinitis pigmentosa. *American Journal of Ophthalmology*, *125*(2), 214–226. https://doi.org/10.1016/s0002-9394(99)80094-4

Seiple, W., Clemens, C. J., Greenstein, V. C., Carr, R. E., & Holopigian, K. (2004). Test-retest reliability of the multifocal electroretinogram and humphrey visual fields in patients with retinitis pigmentosa. *Documenta Ophthalmologica. Advances in Ophthalmology*, *109*(3), 255–272. https://doi.org/10.1007/s10633-005-0567-0

Selmi, T., Alecci, C., dell' Aquila, M., Montorsi, L., Martello, A., Guizzetti, F., Volpi, N., Parenti, S., Ferrari, S., Salomoni, P., Grande, A., & Zanocco-Marani, T. (2015). ZFP36 stabilizes RIP1 via degradation of XIAP and cIAP2 thereby promoting ripoptosome assembly. *BMC Cancer*, *15*(1), 357. https://doi.org/10.1186/s12885-015-1388-5

Sheth, B. R., & Young, R. (2016). Two visual pathways in primates based on sampling of space: Exploitation and exploration of visual information. *Frontiers in Integrative Neuroscience*, *10*. https://doi.org/10.3389/fnint.2016.00037

Sieving, P. A., Arnold, E. B., Jamison, J., Liepa, A., & Coats, C. (1998). Submicrovolt flicker electroretinogram: cycle-by-cycle recording of multiple harmonics with statistical estimation of measurement uncertainty. *Investigative Ophthalmology & Visual Science*, *39*(8), 1462–1469. https://www.ncbi.nlm.nih.gov/pubmed/9660495

Sousa, K., Fernandes, T., Gentil, R., Mendonça, L., & Falcão, M. (2019). Outer retinal layers as predictors of visual acuity in retinitis pigmentosa: a cross-sectional study. *Graefe s Archive for Clinical and Experimental Ophthalmology*, *257*(2), 265–271. https://doi.org/10.1007/s00417-018-4185-4

Spaide, R. F., & Curcio, C. A. (2011). Anatomical correlates to the bands seen in the outer retina by optical coherence tomography: literature review and model. *Retina (Philadelphia, Pa.)*, *31*(8), 1609–1619. https://doi.org/10.1097/IAE.0b013e3182247535

Speros, P., & Price, J. (1981). Oscillatory potentials. History, techniques and potential use in the evaluation of disturbances of retinal circulation. *Survey of Ophthalmology*, *25*(4), 237–252. https://doi.org/10.1016/0039-6257(81)90093-x

Squire, L. R. (Ed.). (2011). *Encyclopedia of Neuroscience*. Elsevier Science & Technology.

Staurenghi, G., Sadda, S., Chakravarthy, U., Spaide, R. F., & International Nomenclature for Optical Coherence Tomography (IN•OCT) Panel. (2014). Proposed lexicon for anatomic landmarks in normal posterior segment spectral-domain optical coherence tomography: the IN•OCT consensus. *Ophthalmology*, *121*(8), 1572–1578. https://doi.org/10.1016/j.ophtha.2014.02.023

Strauss, R. W., Ho, A., Muñoz, B., Cideciyan, A. V., Sahel, J. A., & Sunness, J. S. (2016). Progression of Stargardt Disease Study Group The Natural History of the Progression of Atrophy Secondary to Stargardt Disease (ProgStar) Studies: Design and Baseline Characteristics. *Ophthalmology*, *1*, 817–828.

Strauss, Rupert W., Kong, X., Ho, A., Jha, A., West, S., Ip, M., Bernstein, P. S., Birch, D. G., Cideciyan, A. V., Michaelides, M., Sahel, J.-A., Sunness, J. S., Traboulsi, E. I., Zrenner, E., Pitetta, S., Jenkins, D., Hariri, A. H., Sadda, S., Scholl, H. P. N., & for the ProgStar Study Group. (2019). Progression of stargardt disease as determined by fundus autofluorescence over a 12-month period. *JAMA Ophthalmology*, *137*(10), 1134. https://doi.org/10.1001/jamaophthalmol.2019.2885

Strettoi, E., Gargini, C., Novelli, E., Sala, G., Piano, I., Gasco, P., & Ghidoni, R. (2010). Inhibition of ceramide biosynthesis preserves photoreceptor structure and function in a mouse model of retinitis pigmentosa. *Proceedings of the National Academy of Sciences of the United States of America*, *107*(43), 18706–18711. https://doi.org/10.1073/pnas.1007644107

Sugawara, T., Sato, E., Baba, T., Hagiwara, A., Tawada, A., & Yamamoto, S. (2011). Relationship between vision-related quality of life and microperimetry-determined macular sensitivity in patients with retinitis pigmentosa. *Japanese Journal of Ophthalmology*, *55*(6), 643–646. https://doi.org/10.1007/s10384-011-0080-9

Sujirakul, T., Davis, R., Erol, D., Zhang, L., Schillizzi, G., Royo-Dujardin, L., Shen, S., & Tsang, S. (2015). Bilateral concordance of the fundus hyperautofluorescent ring in typical retinitis pigmentosa patients. *Ophthalmic Genetics*, *36*(2), 113–122. https://doi.org/10.3109/13816810.2013.841962

Sujirakul, T., Lin, M. K., Duong, J., Wei, Y., Lopez-Pintado, S., & Tsang, S. H. (2015). Multimodal imaging of central retinal disease progression in a 2-year mean follow-up of retinitis pigmentosa. *American Journal of Ophthalmology*, *160*(4), 786-98.e4. https://doi.org/10.1016/j.ajo.2015.06.032

Sutter, E. E., & Tran, D. (1992). The field topography of ERG components in man--I. The photopic luminance response. *Vision Research*, *32*(3), 433–446. https://doi.org/10.1016/0042-6989(92)90235-b

Suvarna, V. (2010). Phase IV of drug development. *Perspectives in Clinical Research*, *1*(2), 57–60. https://www.ncbi.nlm.nih.gov/pubmed/21829783

Swaroop, A., & Zack, D. J. (2002). Transcriptome analysis of the retina. *Genome Biology*, *3*(8), REVIEWS1022. https://doi.org/10.1186/gb-2002-3-8-reviews1022

Szlyk, J. P., Seiple, W., Fishman, G. A., Alexander, K. R., Grover, S., & Mahler, C. L. (2001). Perceived and actual performance of daily tasks: relationship to visual function tests in individuals with retinitis pigmentosa. *Ophthalmology*, *108*(1), 65–75. https://doi.org/10.1016/s0161-6420(00)00413-9

Tabuchi, K., Pak, K., Chavez, E., & Ryan, A. F. (2007). Role of inhibitor of apoptosis protein in gentamicin-induced cochlear hair cell damage. *Neuroscience*, *149*(1), 213–222. https://doi.org/10.1016/j.neuroscience.2007.06.061

Takahashi, R., Deveraux, Q., Tamm, I., Welsh, K., Assa-Munt, N., Salvesen, G. S., & Reed, J. C. (1998). A single BIR domain of XIAP sufficient for inhibiting caspases. *The Journal of Biological Chemistry*, *273*(14), 7787–7790. https://doi.org/10.1074/jbc.273.14.7787

Takahashi, V. K. L., Takiuti, J. T., Carvalho-Jr, J. R. L., Xu, C. L., Duong, J. K., Mahajan, V. B., & Tsang, S. H. (2019). Fundus autofluorescence and ellipsoid zone (EZ) line width can be an outcome measurement in RHO-associated autosomal dominant retinitis pigmentosa. *Graefe s Archive for Clinical and Experimental Ophthalmology*, *257*(4), 725–731. https://doi.org/10.1007/s00417-018-04234-6

Takahashi, V. K. L., Takiuti, J. T., Jauregui, R., Lima, L. H., & Tsang, S. H. (2018). Structural disease progression in PDE6-associated autosomal recessive retinitis pigmentosa. *Ophthalmic Genetics*, *39*(5), 610–614. https://doi.org/10.1080/13816810.2018.1509354

Takahashi, V. K. L., Xu, C. L., Takiuti, J. T., Apatoff, M. B. L., Duong, J. K., Mahajan, V. B., & Tsang, S. H. (2019). Comparison of structural progression between ciliopathy and non-ciliopathy associated with autosomal recessive retinitis pigmentosa. *Orphanet Journal of Rare Diseases*, *14*(1), 187. https://doi.org/10.1186/s13023-019-1163-9

Talib, M., Dagnelie, G., & Boon, C. J. F. (2018). Recording and analysis of Goldmann kinetic visual fields. *Methods in Molecular Biology (Clifton, N.J.)*, *1715*, 327–338. https://doi.org/10.1007/978-1-4939-7522-8_24

Talib, M., van Schooneveld, M. J., van Genderen, M. M., Wijnholds, J., Florijn, R. J., Ten Brink, J. B., Schalij-Delfos, N. E., Dagnelie, G., Cremers, F. P. M., Wolterbeek, R., Fiocco, M., Thiadens, A. A., Hoyng, C. B., Klaver, C. C., Bergen, A. A., & Boon, C. J. F. (2017). Genotypic and phenotypic characteristics of CRB1-associated retinal dystrophies: A long-term follow-up study. *Ophthalmology*, *124*(6), 884–895. https://doi.org/10.1016/j.ophtha.2017.01.047

Tanna, P., Strauss, R. W., Fujinami, K., & Michaelides, M. (2017). Stargardt disease: clinical features, molecular genetics, animal models and therapeutic options. *The British Journal of Ophthalmology*, *101*(1), 25–30. https://doi.org/10.1136/bjophthalmol-2016-308823

Tenev, T., Bianchi, K., Darding, M., Broemer, M., Langlais, C., Wallberg, F., Zachariou, A., Lopez, J., MacFarlane, M., Cain, K., & Meier, P. (2011). The Ripoptosome, a signaling platform that assembles in response to genotoxic stress and loss of IAPs. *Molecular Cell*, *43*(3), 432–448. https://doi.org/10.1016/j.molcel.2011.06.006

Terman, A., & Brunk, U. T. (2006). Oxidative stress, accumulation of biological "garbage", and aging. *Antioxidants & Redox Signaling*, *8*(1–2), 197–204. https://doi.org/10.1089/ars.2006.8.197

Testa, F., Maguire, A. M., Rossi, S., Pierce, E. A., Melillo, P., Marshall, K., Banfi, S., Surace, E. M., Sun, J., Acerra, C., Wright, J. F., Wellman, J., High, K. A., Auricchio, A., Bennett, J., & Simonelli, F. (2013). Three-year follow-up after unilateral subretinal delivery of adeno-associated virus in patients with Leber congenital Amaurosis type 2. *Ophthalmology*, *120*(6), 1283–1291. https://doi.org/10.1016/j.ophtha.2012.11.048

Theelen, T., & Teussink, M. M. (2018). Inspection of the human retina by optical coherence tomography. *Methods in Molecular Biology (Clifton, N.J.)*, *1715*, 351–358. https://doi.org/10.1007/978-1-4939-7522-8_26

Travis, G. H. (1998). Mechanisms of cell death in the inherited retinal degenerations. *The American Journal of Human Genetics*, *62*(3), 503–508. https://doi.org/10.1086/301772

Tsujikawa, M., Wada, Y., Sukegawa, M., Sawa, M., Gomi, F., Nishida, K., & Tano, Y. (2008). Age at onset curves of retinitis pigmentosa. *Archives of Ophthalmology*, *126*(3), 337–340. https://doi.org/10.1001/archopht.126.3.337

Tzekov, R., Birch, D., & Seed, P. (1998). Intervisit variability of ERG amplitudes. *Invest Op*, *39*(S2769).

Ulrich, S. (2003). Visual field defects: essentials for neurolo- gists. *J Neurol*, *250*(4), 407–411.

Uy, H. S., Chan, P. S., & Cruz, F. M. (2013). Stem cell therapy: a novel approach for vision restoration in retinitis pigmentosa. *Medical Hypothesis, Discovery and Innovation in Ophthalmology*, *2*(2), 52–55. https://www.ncbi.nlm.nih.gov/pubmed/24600643

Vámos, R., Tátrai, E., Németh, J., Holder, G. E., DeBuc, D. C., & Somfai, G. M. (2011). The structure and function of the macula in patients with advanced retinitis pigmentosa. *Investigative Ophthalmology & Visual Science*, *52*(11), 8425–8432. https://doi.org/10.1167/iovs.11-7780

Van Buren., J. M. (2005). *The retinal ganglion cell layer* (Vol. 51, pp. 399–399). Oxford University Press (OUP). https://doi.org/10.1002/bjs.1800510553

Van Trigt, A. C. (1852). *De oogspiegel. Nederlandisch Lancet, third series* (Vol. 1853, pp. 417–509).

Verbakel, S. K., van Huet, R. A. C., Boon, C. J. F., den Hollander, A. I., Collin, R. W. J., Klaver, C. C. W., Hoyng, C. B., Roepman, R., & Klevering, B. J. (2018). Non-syndromic retinitis pigmentosa. *Progress in Retinal and Eye Research*, *66*, 157–186. https://doi.org/10.1016/j.preteyeres.2018.03.005

Viringipurampeer, I. A., Shan, X., Gregory-Evans, K., Zhang, J. P., Mohammadi, Z., & Gregory-Evans, C. Y. (2014). Rip3 knockdown rescues photoreceptor cell death in blind pde6c zebrafish. *Cell Death and Differentiation*, *21*(5), 665–675. https://doi.org/10.1038/cdd.2013.191

Viringipurampeer, Ishaq A., Metcalfe, A. L., Bashar, A. E., Sivak, O., Yanai, A., Mohammadi, Z., Moritz, O. L., Gregory-Evans, C. Y., & Gregory-Evans, K. (2016). NLRP3 inflammasome activation drives bystander cone photoreceptor cell death in a P23H rhodopsin model of retinal degeneration. *Human Molecular Genetics*, *25*(8), 1501–1516. https://doi.org/10.1093/hmg/ddw029

Vislisel, J. (n.d.). *Atlas Entry - Normal fundus - adult*. Retrieved September 28, 2023, from https://webeye.ophth.uiowa.edu/eyeforum/atlas/pages/normal-fundus.htm

Visuvanathan, S., Baker, A. N., Lagali, P. S., Coupland, S. G., Miller, G., Hauswirth, W. W., & Tsilfidis, C. (2022). XIAP gene therapy effects on retinal ganglion cell structure and function in a mouse model of glaucoma. *Gene Therapy*, *29*(3–4), 147–156. https://doi.org/10.1038/s41434-021-00281-7

Wachtmeister, L. (1980). Further studies of the chemical sensitivity of the oscillatory potentials of the electroretinogram (ERG) I. GABA- and glycine antagonists. *Acta Ophthalmologica*, *58*(5), 712–725. https://doi.org/10.1111/j.1755-3768.1980.tb06684.x

Wachtmeister, L. (1981). Further studies of the chemical sensitivity of the oscillatory potentials of the electroretinogram (ERG). III. Some omega amino acids and ethanol. *Acta Ophthalmologica*, *59*(4), 609–619. https://doi.org/10.1111/j.1755-3768.1981.tb08349.x

Wachtmeister, L. (1998). Oscillatory potentials in the retina: what do they reveal. *Progress in Retinal and Eye Research*, *17*(4), 485–521. https://doi.org/10.1016/s1350-9462(98)00006-8

Wang, J., Menchenton, T., Yin, S., Yu, Z., Bance, M., Morris, D. P., Moore, C. S., Korneluk, R. G., & Robertson, G. S. (2010). Over-expression of X-linked inhibitor of apoptosis protein slows presbycusis in C57BL/6J mice. *Neurobiology of Aging*, *31*(7), 1238–1249. https://doi.org/10.1016/j.neurobiolaging.2008.07.016

Wang, N., Liu, X., & Fan, N. (Eds.). (2019). *Optic disorders and visual field* (1st ed.) [PDF]. Springer. https://doi.org/10.1007/978-981-13-2502-1

Wassmer, S. J., De Repentigny, Y., Sheppard, D., Lagali, P. S., Fang, L., Coupland, S. G., Kothary, R., Guy, J., Hauswirth, W. W., & Tsilfidis, C. (2020). XIAP protects retinal ganglion cells in the mutant ND4 mouse model of Leber hereditary optic neuropathy. *Investigative Ophthalmology & Visual Science*, *61*(8), 49. https://doi.org/10.1167/iovs.61.8.49

Wassmer, S. J., Leonard, B. C., Coupland, S. G., Baker, A. N., Hamilton, J., Hauswirth, W. W., & Tsilfidis, C. (2017). Overexpression of the X-linked inhibitor of apoptosis protects against retinal degeneration in a feline model of retinal detachment. *Human Gene Therapy*, *28*(6), 482–492. https://doi.org/10.1089/hum.2016.161

Weleber, R. G., Smith, T. B., Peters, D., Chegarnov, E. N., Gillespie, S. P., Francis, P. J., Gardiner, S. K., Paetzold, J., Dietzsch, J., Schiefer, U., & Johnson, C. A. (2015). VFMA: Topographic analysis of sensitivity data from full-field static perimetry. *Translational Vision Science & Technology*, *4*(2), 14. https://doi.org/10.1167/tvst.4.2.14

Wen, Y., Klein, M., Hood, D. C., & Birch, D. G. (2012). Relationships among multifocal electroretinogram amplitude, visual field sensitivity, and SD-OCT receptor layer thicknesses in patients with retinitis pigmentosa. *Investigative Ophthalmology & Visual Science*, *53*(2), 833–840. https://doi.org/10.1167/iovs.11-8410

Witkin, A. J., Ko, T. H., Fujimoto, J. G., Chan, A., Drexler, W., Schuman, J. S., Reichel, E., & Duker, J. S. (2006). Ultra-high resolution optical coherence tomography assessment of photoreceptors in retinitis pigmentosa and related diseases. *American Journal of Ophthalmology*, *142*(6), 945–952. https://doi.org/10.1016/j.ajo.2006.07.024

Wong, A., & Sharpe, J. A. (2000). A comparison of tangent screen, Goldmann, and Humphrey perimetry in the detection and localization of occipital lesions. *Ophthalmology*, *107*, 527–544.

Wong, S. H., & Plant, G. T. (2015). How to interpret visual fields. *Pract Neurol*, *15*, 374–381.

Wouters, O. J., McKee, M., & Luyten, J. (2020). Estimated research and development investment needed to bring a new medicine to market, 2009-2018. *JAMA: The Journal of the American Medical Association*, *323*(9), 844. https://doi.org/10.1001/jama.2020.1166

Wright, A. F. (2015). Long-term effects of retinal gene therapy in childhood blindness [Review of *Long-term effects of retinal gene therapy in childhood blindness*]. *The New England Journal of Medicine*, *372*(20), 1954–1955. https://doi.org/10.1056/NEJMe1503419

Wright, M. E., Han, D. K., & Hockenbery, D. M. (2000). Caspase-3 and inhibitor of apoptosis protein(s) interactions in Saccharomyces cerevisiae and mammalian cells. *FEBS Letters*, *481*(1), 13–18. https://doi.org/10.1016/s0014-5793(00)01962-1

Xiaoming C, Y. Y. (2000). *Modern clinical visual field test*. People's Medical Publishing House.

Xu, D., Bureau, Y., McIntyre, D. C., Nicholson, D. W., Liston, P., Zhu, Y., Fong, W. G., Crocker, S. J., Korneluk, R. G., & Robertson, G. S. (1999). Attenuation of ischemia-induced cellular and behavioral deficits by X chromosome-linked inhibitor of apoptosis protein overexpression in the rat hippocampus. *The Journal of Neuroscience: The Official Journal of the Society for Neuroscience*, *19*(12), 5026–5033. https://doi.org/10.1523/jneurosci.19-12-05026.1999

Xu, M., Zhai, Y., & MacDonald, I. M. (2020). Visual field progression in retinitis pigmentosa. *Investigative Ophthalmology & Visual Science*, *61*(6), 56. https://doi.org/10.1167/iovs.61.6.56

Yabal, M., & Jost, P. J. (2015). XIAP as a regulator of inflammatory cell death: the TNF and RIP3 angle. *Molecular & Cellular Oncology*, *2*(1), e964622. https://doi.org/10.4161/23723548.2014.964622

Yabal, M., Müller, N., Adler, H., Knies, N., Groß, C. J., Damgaard, R. B., Kanegane, H., Ringelhan, M., Kaufmann, T., Heikenwälder, M., Strasser, A., Groß, O., Ruland, J., Peschel, C., Gyrd-Hansen, M., & Jost, P. J. (2014). XIAP restricts TNF- and RIP3-dependent cell death and inflammasome activation. *Cell Reports*, *7*(6), 1796–1808. https://doi.org/10.1016/j.celrep.2014.05.008

Yao, J., Feathers, K. L., Khanna, H., Thompson, D., Tsilfidis, C., Hauswirth, W. W., Heckenlively, J. R., Swaroop, A., & Zacks, D. N. (2011). XIAP therapy increases survival of transplanted rod precursors in a degenerating host retina. *Investigative Ophthalmology & Visual Science*, *52*(3), 1567–1572. https://doi.org/10.1167/iovs.10-5998

Yao, J., Jia, L., Khan, N., Zheng, Q.-D., Moncrief, A., Hauswirth, W. W., Thompson, D. A., & Zacks, D. N. (2012). Caspase inhibition with XIAP as an adjunct to AAV vector gene-replacement therapy: improving efficacy and prolonging the treatment window. *PloS One*, *7*(5), e37197. https://doi.org/10.1371/journal.pone.0037197

Yi, T., Shihui, W., & Siwei, Y. (2010). *Basis and clinical progress of visual pathway diseases. Beijing: People's Medical Publishing House*.

Yokochi, M., Li, D., Horiguchi, M., & Kishi, S. (2012). Inverse pattern of photoreceptor abnormalities in retinitis pigmentosa and cone-rod dystrophy. *Documenta Ophthalmologica. Advances in Ophthalmology*, *125*(3), 211–218. https://doi.org/10.1007/s10633-012-9348-8

Yu, D.-Y., & Cringle, S. J. (2005). Retinal degeneration and local oxygen metabolism. *Experimental Eye Research*, *80*(6), 745–751. https://doi.org/10.1016/j.exer.2005.01.018

Yuansheng Y, H. Z. (2015). *Modern clinical visual field test*. People's Medical Publishing House.

Yuansheng, Y., Jia, M., & Hui, Z. (2005). *Principle for humphrey visual field test and analysis. Beijing: People's Medical Publishing House*.

Yung, M., Klufas, M. A., & Sarraf, D. (2016). Clinical applications of fundus autofluorescence in retinal disease. *International Journal of Retina and Vitreous*, *2*(1), 12. https://doi.org/10.1186/s40942-016-0035-x

Zadro-Lamoureux, L. A., Zacks, D. N., Baker, A. N., Zheng, Q.-D., Hauswirth, W. W., & Tsilfidis, C. (2009). XIAP effects on retinal detachment-induced photoreceptor apoptosis [corrected]. *Investigative Ophthalmology & Visual Science*, *50*(3), 1448–1453. https://doi.org/10.1167/iovs.08-2855

Zahid, S., Peeler, C., Khan, N., Davis, J., Mahmood, M., Heckenlively, J. R., & Jayasundera, T. (2014). Digital quantification of Goldmann visual fields (GVFs) as a means for genotype-phenotype comparisons and detection of progression in retinal degenerations. *Advances in Experimental Medicine and Biology*, *801*, 131–137. https://doi.org/10.1007/978-1-4614-3209-8_17

Zhao, Y., Feng, K., Liu, R., Pan, J., Zhang, L., & Lu, X. (2019). Vitamins and mineral supplements for retinitis pigmentosa. *Journal of Ophthalmology*, *2019*, 8524607. https://doi.org/10.1155/2019/8524607

Zrenner, E., Bartz-Schmidt, K. U., Benav, H., Besch, D., Bruckmann, A., Gabel, V.-P., Gekeler, F., Greppmaier, U., Harscher, A., Kibbel, S., Koch, J., Kusnyerik, A., Peters, T., Stingl, K., Sachs, H., Stett, A., Szurman, P., Wilhelm, B., & Wilke, R. (2011). Subretinal electronic chips allow blind patients to read letters and combine them to words. *Proceedings. Biological Sciences*, *278*(1711), 1489–1497. https://doi.org/10.1098/rspb.2010.1747

Appendix

A. ImageJ protocol for manual measurement of ellipsoid zone on OCT

To measure the ellipsoid zone from an OCT image using ImageJ:

1. Launch ImageJ → File → Open → import OCT.png
2. From toolbar select the straight-line tool
3. Use + key to zoom on scale at the bottom left of the OCT raster (not the fundus image)
4. Click and hold on the outer edge of the white line (not grey border)
5. Move cursor to draw horizontal line to opposite outer edge of the white line
6. Release to create line
7. Adjust nodes as needed to straighten
8. Analyse → Set scale
   Known distance: 200
   Unit of Length: µm
9. Use – key to zoom out
10. From toolbar click and hold on straight-line tool to change to segmented line
11. Click to trace the ellipsoid zone (2nd hyperreflective line from the RPE)
12. Double-click or right-click on the last node to complete the line
13. Adjust nodes as needed to best fit
14. Analyse → Measure
15. Record length

B. Normative data for multi-focal ERG

LCD 61 Hex		N1 (ms)		P1 (ms)		P1 (nv/d2)	
Age	**Ring**	**Mean**	**2 SD**	**Mean**	**2 SD**	**Mean**	**2 SD**
0-40	**1**	14.60	5.80	29.00	3.00	36.35	14.95
	2	14.20	3.90	29.00	3.00	18.80	6.00
	3	14.35	2.85	28.80	3.40	10.40	3.40
	4	14.70	2.30	29.40	2.70	7.15	2.45
	5	14.55	2.45	29.55	3.15	6.40	2.20
40-60	**1**	16.70	3.80	30.95	3.75	37.35	14.75
	2	14.85	2.75	30.20	2.30	17.05	6.55
	3	14.45	2.55	30.00	2.30	10.60	4.00
	4	15.45	2.55	30.75	2.45	7.80	3.10
	5	15.75	2.25	31.05	2.55	6.60	2.80
60-100	**1**	16.80	5.10	31.50	7.90	34.95	17.75
	2	15.15	3.45	30.35	6.95	15.60	6.80
	3	14.90	3.10	30.25	6.75	10.15	4.35
	4	15.65	3.05	30.85	7.05	7.75	3.45
	5	16.20	3.40	31.15	7.15	6.45	2.95

C. Normative data for full-field ERG

2019.1 Norms

S1 Photopic - Light-adapted 3.0 Flash ERG -- single flash

		A time	A time range	A Amp	A Amp Range	B time	B time range	B Amp	B Amp Range
1	0-10	13.84	2.89	-52.72	26.77	27.80	2.05	190.14	92.38
2	10-20	13.61	2.78	-40.64	34.43	29.24	3.65	153.82	90.22
3	20-30	13.87	3.16	-36.56	26.48	29.24	4.19	130.62	66.32
4	30-40	13.34	2.72	-32.29	21.38	28.91	3.20	128.83	56.46
5	40-50	13.43	2.80	-33.04	16.27	30.41	3.65	120.50	46.59
6	50-60	14.16	2.49	-34.36	19.24	30.69	3.26	124.17	67.57
7	60-70	14.09	2.74	-29.44	15.72	30.48	3.66	118.30	55.90
8	70-100	13.90	2.51	-29.51	14.83	30.96	4.72	104.95	44.23

S3 Photopic -Light-adapted 3.0 Flicker ERG (30 Hz)

		Peak time	Peak time range	Peak Amp	Peak Amp Range	Trough time	Trough time range	Trough Amp	Trough Amp Range
1	0-10	24.32	2.47	135.52	65.01	9.89	3.48	0.00	0.00
2	10-20	25.53	3.30	118.30	65.00	11.04	3.30	0.00	0.00
3	20-30	25.65	4.75	117.49	59.66	11.83	3.03	0.00	0.00
4	30-40	25.65	3.91	108.89	49.73	11.64	3.09	0.00	0.00
5	40-50	26.30	4.50	101.86	49.38	12.27	3.55	0.00	0.00
6	50-60	27.04	3.25	106.17	49.02	12.42	3.12	0.00	0.00
7	60-70	26.67	4.94	103.75	47.38	12.47	2.78	0.00	0.00
8	70-100	29.83	6.29	107.65	51.89	14.59	4.79	0.00	0.00

S1 Scotopic -Dark-adapted 0.01 ERG -- single flash

		A time	A time range	A Amp	A Amp Range	B time	B time range	B Amp	B Amp Range
1	0-10	36.91	12.34	-43.80	51.84	85.90	14.31	343.56	169.14
2	10-20	36.91	12.34	-43.80	51.84	90.99	20.71	243.78	127.57
3	20-30	37.72	6.82	-36.39	41.98	94.19	18.77	233.88	188.35
4	30-40	38.86	3.31	-34.76	42.95	91.62	20.85	218.78	168.49
5	40-50	38.86	12.02	-33.12	43.92	95.28	18.54	207.01	161.85
6	50-60	38.27	8.73	-32.31	33.32	96.16	12.43	212.32	142.28
7	60-70	39.14	8.33	-31.50	33.94	97.72	19.48	208.93	139.28
8	70-100	39.14	8.33	-31.50	33.94	103.75	22.14	194.54	141.99

S3 Scotopic -Dark-adapted 3.0 ERG -- single flash

		A time	A time range	A Amp	A Amp Range	B time	B time range	B Amp	B Amp Range
1	0-10	14.06	8.17	-246.00	292.39	48.31	9.40	494.31	261.25
2	10-20	14.76	2.39	-212.80	125.96	46.99	8.71	360.60	181.23
3	20-30	14.19	3.97	-195.40	93.22	45.92	10.67	334.20	147.55
4	30-40	15.03	3.85	-200.90	118.91	46.88	9.79	323.59	177.17
5	40-50	15.60	3.99	-172.20	75.15	47.75	10.64	283.79	95.83
6	50-60	16.14	4.21	-181.10	87.32	46.99	9.81	287.10	113.19
7	60-70	15.85	4.36	-178.65	80.66	49.20	7.97	290.40	131.21
8	70-100	17.38	7.67	-176.20	87.65	50.12	5.32	316.23	149.22

S5 Scotopic -Dark-adapted 10.0 ERG -- Single flash

		A time	A time range	A Amp	A Amp Range	B time	B time range	B Amp	B Amp Range
1	0-10	11.80	1.53	-306.20	98.94	39.63	15.52	502.34	172.08
2	10-20	12.16	1.97	-221.30	112.37	43.15	11.05	340.41	157.09
3	20-30	12.02	1.39	-210.90	111.44	43.55	9.90	341.19	142.09
4	30-40	11.70	1.35	-201.40	106.56	43.85	10.20	325.47	153.76
5	40-50	12.68	1.35	-191.90	73.24	44.11	10.60	309.74	136.16
6	50-60	13.00	2.35	-196.20	83.24	44.36	8.30	318.54	118.55
7	60-70	12.53	2.56	-200.50	90.52	47.21	8.10	297.30	105.77
8	70-100	13.22	1.97	-184.50	48.99	44.42	8.72	276.06	167.84

D. Supplemental results

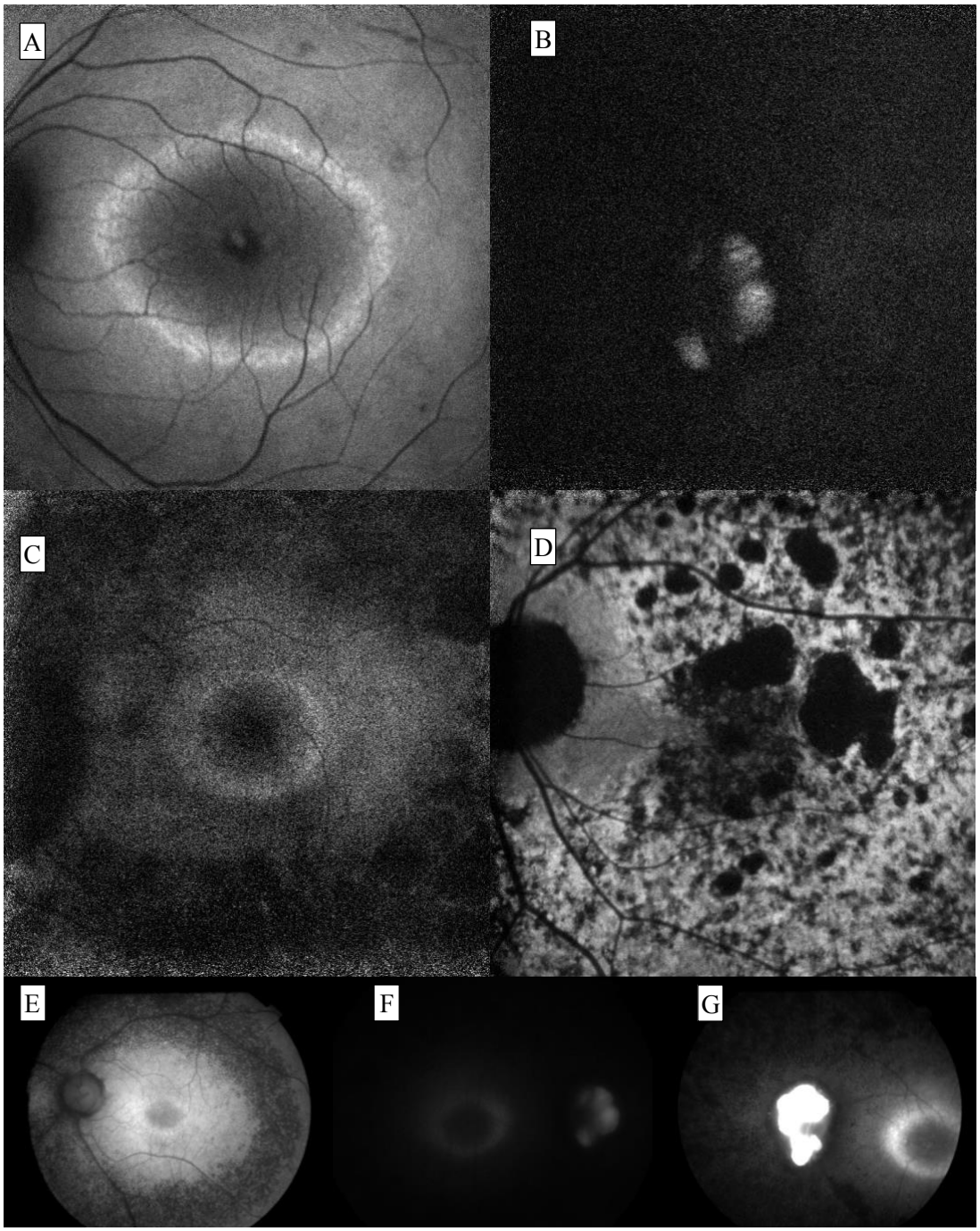

Supplemental Figure I. Various FAF presentations within study cohort. Images a-d display OCT FAFs whereas images e-f display fundus camera FAFs. (A) OCT FAF of acceptable quality, which clearly captures the borders of the hyperautofluorescent ring (HAR). (B) OCT FAF of low exposure with lack of visible retinal landmarks. (C) OCT FAF of poor quality. Although the HAR is visible, high grain and noise make it difficult to pinpoint the exact limits. (D) OCT FAF of a patient with severe retinal dystrophy and geographic atrophy. The macula and HAR are not visible or measurable. (E) Fundus FAF of acceptable quality, which provides a wider view of the retina but still faintly delineates the borders of the hyperautofluorescent ring. (F) Fundus FAF of low exposure and poor visibility. (g) Fundus FAF with central exposure artefact. Scale is not available on any FAF images.

Supplemental Table I. Correlation of ellipsoid zone length and mfERG amplitude and latencies.

Ring	Response	Correlation	p-value
1	N1 latency	-0.24	0.067
	P1 latency	-0.22	0.100
	P1 amplitude	0.53	<0.001
2	N1 latency	-0.37	0.005
	P1 latency	-0.19	0.163
	P1 amplitude	0.83	<0.001
3	N1 latency	-0.49	<0.001
	P1 latency	-0.08	0.056
	P1 amplitude	0.72	<0.001
4	N1 latency	-0.18	0.171
	P1 latency	-0.17	0.200
	P1 amplitude	0.65	<0.001
5	N1 latency	0.08	0.563
	P1 latency	0.15	0.263
	P1 amplitude	0.57	<0.001

Supplemental Table II. Correlation of ellipsoid zone length and ffERG amplitudes and latencies.

Condition	Strength	Response	Correlation	p-value
Photopic		a-wave amplitude	-0.41	<0.001
		a-wave latency	-0.02	0.885
		b-wave amplitude	0.64	<0.001
		b-wave latency	-0.22	0.052
30Hz Flicker		peak amplitude	0.57	<0.001
		peak latency	-0.17	0.146
		trough latency	-0.44	<0.001
Scotopic	0.01	a-wave amplitude	-0.19	0.103
		a-wave latency	-0.28	0.015
		b-wave amplitude	0.62	<0.001
		b-wave latency	-0.24	0.038
	3.0	a-wave amplitude	-0.62	<0.001
		a-wave latency	-0.46	<0.001
		b-wave amplitude	0.65	<0.001
		b-wave latency	0.23	0.045
	10.0	a-wave amplitude	-0.61	<0.001
		a-wave latency	-0.32	0.005
		b-wave amplitude	0.63	<0.001
		b-wave latency	-0.42	<0.001

Supplemental Table III. Correlation of HVF mean deviation and mfERG amplitudes and latencies.

Protocol	Ring	Response	Correlation	p-value
30-2	1	N1 latency	0.34	0.411
		P1 latency	0.45	0.260
		P1 amplitude	-0.44	0.276
	2	N1 latency	0.07	0.875
		P1 latency	0.36	0.382
		P1 amplitude	0.35	0.397
	3	N1 latency	-0.86	0.006
		P1 latency	-0.35	0.397
		P1 amplitude	0.74	0.038
	4	N1 latency	-0.19	0.648
		P1 latency	0.28	0.509
		P1 amplitude	0.44	0.272
	5	N1 latency	0.25	0.550
		P1 latency	0.40	0.326
		P1 amplitude	0.54	0.170

24-2	1	N1 latency	-0.11	0.725
		P1 latency	0.32	0.315
		P1 amplitude	0.27	0.392
	2	N1 latency	-0.89	<0.001
		P1 latency	0.09	0.791
		P1 amplitude	0.61	0.034
	3	N1 latency	-0.73	0.006
		P1 latency	-0.87	<0.001
		P1 amplitude	0.74	0.006
	4	N1 latency	-0.71	0.010
		P1 latency	-0.78	0.003
		P1 amplitude	0.72	0.008
	5	N1 latency	-0.77	0.003
		P1 latency	-0.50	0.100
		P1 amplitude	0.61	0.036

Supplemental Table IV. Correlation of GVF isopter length and mfERG amplitudes and latencies.

Protocol	Ring	Response	Correlation	p-value
V4e	1	N1 latency	-0.72	0.018
		P1 latency	-0.66	0.036
		P1 amplitude	-0.17	0.631
	2	N1 latency	0.10	0.779
		P1 latency	-0.38	0.280
		P1 amplitude	-0.09	0.804
	3	N1 latency	-0.25	0.487
		P1 latency	0.23	0.525
		P1 amplitude	-0.42	0.229
	4	N1 latency	0.67	0.035
		P1 latency	-0.35	0.318
		P1 amplitude	-0.56	0.089
	5	N1 latency	0.41	0.242
		P1 latency	0.22	0.538
		P1 amplitude	-0.45	0.194
III4e	1	N1 latency	-0.35	0.323
		P1 latency	-0.87	<0.001
		P1 amplitude	0.54	0.107
	2	N1 latency	0.25	0.487
		P1 latency	-0.80	0.005
		P1 amplitude	-0.34	0.331
	3	N1 latency	0.36	0.301
		P1 latency	-0.19	0.591
		P1 amplitude	-0.61	0.062
	4	N1 latency	0.21	0.554
		P1 latency	0.03	0.930
		P1 amplitude	-0.31	0.382
	5	N1 latency	0.68	0.029
		P1 latency	0.29	0.410
		P1 amplitude	-0.02	0.947
I4e	1	N1 latency	-0.16	0.448
		P1 latency	-0.16	0.464
		P1 amplitude	0.36	0.081
	2	N1 latency	0.26	0.217
		P1 latency	0.05	0.821
		P1 amplitude	0.11	0.620
	3	N1 latency	0.36	0.087
		P1 latency	0.40	0.052
		P1 amplitude	-0.30	0.157
	4	N1 latency	0.05	0.827
		P1 latency	-0.06	0.791

		P1 amplitude	-0.10	0.642
	5	N1 latency	0.40	0.054
		P1 latency	0.24	0.264
		P1 amplitude	0.33	0.111
13e	1	N1 latency	-0.33	0.073
		P1 latency	0.002	0.993
		P1 amplitude	0.43	0.018
	2	N1 latency	-0.09	0.634
		P1 latency	-0.14	0.455
		P1 amplitude	0.47	0.009
	3	N1 latency	-0.07	0.725
		P1 latency	-0.08	0.657
		P1 amplitude	0.48	0.007
	4	N1 latency	-0.21	0.256
		P1 latency	-0.36	0.050
		P1 amplitude	0.52	0.006
	5	N1 latency	0.01	0.967
		P1 latency	-0.19	0.327
		P1 amplitude	0.65	<0.001
12e	1	N1 latency	-0.40143436	0.023
		P1 latency	-0.08997378	0.624
		P1 amplitude	0.41339740	0.019
	2	N1 latency	-0.08461186	0.645
		P1 latency	-0.13821595	0.451
		P1 amplitude	0.55977321	<0.001
	3	N1 latency	-0.16996208	0.352
		P1 latency	-0.12260898	0.504
		P1 amplitude	0.63124261	<0.001
	4	N1 latency	-0.09357547	0.610
		P1 latency	-0.34714148	0.052
		P1 amplitude	0.48422022	0.005
	5	N1 latency	0.09506458	0.605
		P1 latency	-0.17025266	0.352
		P1 amplitude	0.74238097	<0.001

Supplemental Table V. Correlation of GVF isopter length and ffERG amplitudes and latencies.

Isopter	Condition	Strength	Response	Correlation	p-value
V4e	Photopic		a-wave amplitude	-0.23	0.152
			a-wave latency	0.26	0.093
			b-wave amplitude	0.06	0.721
			b-wave latency	-0.10	0.546
	30Hz Flicker		peak amplitude	0.08	0.603
			peak latency	0.04	0.779
			trough latency	-0.09	0.587
	Scotopic	0.01	a-wave amplitude	0.10	0.527
			a-wave latency	-0.25	0.117
			b-wave amplitude	-0.11	0.505
			b-wave latency	-0.25	0.107
		3.0	a-wave amplitude	-0.12	0.454
			a-wave latency	0.008	0.960
			b-wave amplitude	-0.06	0.708
			b-wave latency	-0.16	0.299
		10.0	a-wave amplitude	-0.06	0.708
			a-wave latency	-0.24	0.127
			b-wave amplitude	-0.08	0.600
			b-wave latency	-0.12	0.455
III4e	Photopic		a-wave amplitude	-0.50	0.005
			a-wave latency	0.12	0.531

			b-wave amplitude	0.26	0.168
			b-wave latency	-0.19	0.308
	30Hz Flicker		peak amplitude	0.33	0.076
			peak latency	0.05	0.796
			trough latency	-0.45	0.014
	Scotopic	0.01	a-wave amplitude	-0.01	0.941
			a-wave latency	-0.35	0.057
			b-wave amplitude	-0.11	0.579
			b-wave latency	-0.26	0.160
		3.0	a-wave amplitude	-0.31	0.091
			a-wave latency	0.008	0.967
			b-wave amplitude	-0.08	0.687
			b-wave latency	0.08	0.678
		10.0	a-wave amplitude	-0.14	0.459
			a-wave latency	0.02	0.912
			b-wave amplitude	-0.16	0.412
			b-wave latency	-0.07	0.706
I4e	Photopic		a-wave amplitude	-0.51	<0.001
			a-wave latency	0.008	0.958
			b-wave amplitude	0.65	<0.001
			b-wave latency	-0.37	0.016
	30Hz Flicker		peak amplitude	0.53	<0.001
			peak latency	-0.34	0.030
			trough latency	-0.56	<0.001
	Scotopic	0.01	a-wave amplitude	0.006	0.970
			a-wave latency	-0.20	0.193
			b-wave amplitude	0.36	0.020
			b-wave latency	-0.41	0.008
		3.0	a-wave amplitude	-0.72	<0.001
			a-wave latency	-0.26	0.097
			b-wave amplitude	0.49	0.001
			b-wave latency	0.16	0.327
		10.0	a-wave amplitude	-0.59	<0.001
			a-wave latency	-0.46	0.002
			b-wave amplitude	0.44	0.003
			b-wave latency	-0.26	0.100
I3e	Photopic		a-wave amplitude	-0.39	0.010
			a-wave latency	-0.04	0.780
			b-wave amplitude	0.60	<0.001
			b-wave latency	-0.30	0.054
	30Hz Flicker		peak amplitude	0.45	0.003
			peak latency	-0.33	0.031
			trough latency	-0.50	<0.001
	Scotopic	0.01	a-wave amplitude	-0.08	0.600
			a-wave latency	-0.11	0.486
			b-wave amplitude	0.40	0.008
			b-wave latency	-0.24	0.126
		3.0	a-wave amplitude	-0.63	<0.001
			a-wave latency	-0.36	0.019
			b-wave amplitude	0.51	<0.001
			b-wave latency	0.23	0.149
		10.0	a-wave amplitude	-0.54	<0.001
			a-wave latency	-0.61	<0.001
			b-wave amplitude	0.48	<0.001
			b-wave latency	-0.27	0.090
I2e	Photopic		a-wave amplitude	-0.43	0.004
			a-wave latency	0.008	0.959
			b-wave amplitude	0.59	<0.001
			b-wave latency	-0.28	0.072

	30Hz Flicker		peak amplitude	0.41	0.006
			peak latency	-0.36	0.018
			trough latency	-0.38	0.014
	Scotopic	0.01	a-wave amplitude	-0.14	0.387
			a-wave latency	-0.03	0.865
			b-wave amplitude	0.43	0.005
			b-wave latency	-0.16	0.032
		3.0	a-wave amplitude	-0.61	<0.001
			a-wave latency	-0.17	0.283
			b-wave amplitude	0.53	<0.001
			b-wave latency	0.36	0.019
		10.0	a-wave amplitude	-0.53	<0.001
			a-wave latency	-0.50	<0.001
			b-wave amplitude	0.49	<0.001
			b-wave latency	-0.05	0.741